# Design of Inflatable Solar Concentrator

by

Omar Carrasquillo

B.S. Mechanical Engineering
Massachusetts Institute of Technology, 2011

SUBMITTED TO THE DEPARTMENT OF MECHANICAL ENGINEERING IN PARTIAL FULFILLMENT OF THE REQUIREMENTS FOR THE DEGREE OF

MASTER OF SCIENCE IN MECHANICAL ENGINEERING

AT THE

MASSACHUSETTS INSTITUTE OF TECHNOLOGY

June 2013





Signature of Author: _____
Department of Mechanical Engineering
May 20, 2013

Certified by: _____
Alexander H. Slocum
Pappalardo Professor of Mechanical Engineering
Thesis Supervisor

Accepted by: _____
David E. Hardt
Ralph E. and Eloise F. Cross Professor of Mechanical Engineering
Chairman, Department Committee on Graduate Students

# Design of Inflatable Solar Concentrator

by

Omar Carrasquillo

Submitted to the Department of Mechanical Engineering
on May 20, 2013 in Partial Fulfillment of the
Requirements for the Degree of Master of Science in
Mechanical Engineering

ABSTRACT

Solar concentrators improve the performance of solar collection systems by increasing the amount of usable energy available for a given collector size. Unfortunately, they are not known for their light weight and portability, which is ideal for basic applications like solar cooking. The goal of the project was to a design a light-weight and portable solar concentrator with minimal tracking requirements. The concept of an inflatable compound parabolic concentrator was developed, which required modifying the theoretical profile geometry. An analytical model was created to predict the efficiency of the system for different design parameter configurations. The model was used to develop a design and manufacturing process which was used to design and manufacture small-scale and full-scale prototypes. Experiments were designed to test the performance of the concentrators and the test results were used to determine a model accuracy of 11.4±1.3 % and 1.9±1.6% using the small-scale prototype and full-scale prototype, respectively.

Thesis Supervisor: Alexander H. Slocum
Title: Pappalardo Professor of Mechanical Engineering

# ACKNOWLEDGEMENTS

This thesis would not have been possible without the tremendous support, help and contributions from colleagues, friends, and family. In particular, I would like to extend special thanks to:

Professor Alex Slocum: for the constant encouragement and believing in me, for teaching me how to enjoy what we do, and for guiding me as I start to discover my passion. I'll forever be thankful the opportunity to join his lab, which allowed me to learn so much from him and grow both personal and professionally.

Precision Engineering Research Group (PERG): for always being so supportive and willing to help out.

Grossman Group and Alison Greenlee: for the collaboration in the solar cooker that served as motivation for this project.

Marc Belanger and Ken Stone: for constant support in the Edgerton Student Machine Shop and the MIT Hobby Shop to allow me to build so many crucial components for my research.

Otherlab: in particular to Kevin Simon, for taking on the project of aiding me in the design of the prototype and fabricating it.

Big Blue Saw: for the manufacturing of full-scale sheet metal parts for the reflective panels of the concentrator.

Dr. Barbara Hughey: for providing me with the light sensor that allowed me to conduct the experiments.

Sean Patrick Robinson (MIT Physics Junior Lab): for lending me the neutral density filter that proved to be so crucial in the testing procedures.

Deborah Alibrandi: for making sure I was able to get everything I needed for the research.

Most importantly, my family and friends: for having been present constantly, encouraging me to push through the tough times and succeed.

# TABLE OF CONTENTS

# LIST OF FIGURES

# LIST OF TABLES

# Chapter 1: Introduction

## 1.1 Motivation

The Grossman Group in the Department of Materials Science & Engineering at the Massachusetts Institute of Technology is doing research on a thermal fuel capable of storing solar energy and releasing it on demand. When exposed to sunlight, this fuel undergoes a series of chemical reactions allowing it to store solar energy in its chemical bonds. Then with the use of catalyst, the stored energy can be released in the form of heat as the chemical reactions are reversed and the fuel returns to its original state. Thus, this solar thermal fuel (STF) acts as a source of renewable energy that can be used in a variety of applications. In particular, the possibility using the STF to power a solar cooker was explored.

People in developing countries face many challenges in trying to provide food for their families; often, this has to do with the lack of resources and economic sources of energy. A solar cooker that runs on STF is an ideal product for developing countries because it utilizes a renewable source of energy for an everyday chore such as cooking, as well as a means to cook when the sun isn't available. To maximize the performance of the system, it's important to allow the STF to absorb the necessary solar as quickly as possible. By using a solar concentrator, one is able to focus the amount of solar energy through an aperture into a smaller exit, thus magnifying the solar energy in that area. Currently there are many well-known manufacturing processes for common solar concentrators, but few are known for its light weight and portability.

In the solar cooker industry, minimizing manufacturing costs make the products available to a larger number of people. A way to minimize costs is to reduce the tracking requirements of the solar concentrator, eliminating the need for expensive tracking mechanisms. In addition,

portability is highly desired, as it makes the solar cooker easier to handle and position. Unfortunately, few solar cookers fail to meet these needs because they often require a bulky cumbersome solar concentrator to maximize its performance.

## 1.2 Problem Statement

The goal of this work was to design a light-weight and portable solar concentrator with minimal tracking requirements. To accomplish this, the following tasks were necessary:

1. Study the science governing the design and performance of different types of solar concentrators and compare the advantages and disadvantages between them.
2. Select a solar concentrator for the solar cooker design. An ideal concentrator requires minimal solar tracking without excessively sacrificing concentration.
3. Develop a design concept for a light weight and portable solar concentrator.
4. Create an analytical model to understand the effect of different design parameters on the overall efficiency of the system.
5. Use the analytical model to design the components for a prototype and then develop a robust manufacturing process. Two prototypes were built, one small-scale and another full-scale.
6. Test the prototypes to validate the accuracy of the analytical model.

# Chapter 2: Background

## 2.1 Solar Energy

The sun is a source of renewable energy that emits electromagnetic radiation at a relatively constant rate throughout the year. As described in Chapter 2 of [1], the sun emits energy at a rate equivalent to the energy coming from a furnace at a temperature of about 6,000 K. The total energy emitted by the sun can't be harvested from Earth for several important reasons: 1) the sun's energy dissipates throughout the solar system so only a small fraction of the aforementioned energy reaches the earth, 2) due to the earth's orbit and rotation, the sun's energy only reaches a region on the surface of the earth for a portion of the day (which varies during the year), and 3) the atmosphere reflects 30% of the solar energy that reaches the earth. With all those factors taken into account, the amount of solar energy available at the earth's surface is optimally 1 $kW/m^2$ on a good clear day, near the equator.

For solar applications, the amount of solar energy available depends on the angle of incidence, which is the measure of the angle between the perpendicular line of a surface (normal) and a solar ray incident on the surface [2], as shown in Figure 2-1.

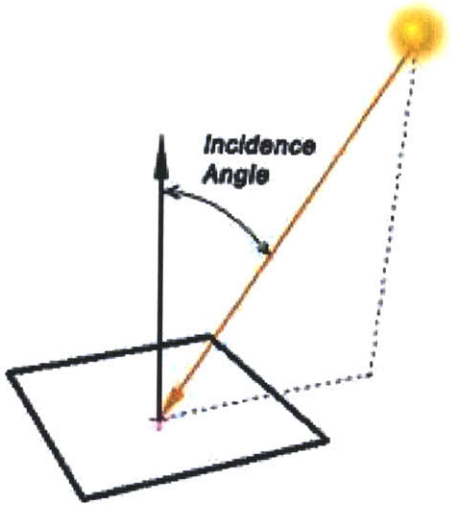


**Figure 2-1: Incidence angle of the sun [2].**

The following equation describes the relationship between the incidence angle, $\theta_i$, and the solar intensity available at a surface, $I$:

$$I = I_0 \cos \theta_i. \qquad \textbf{Equation 2-1}$$

In Equation 2-1, $I_0$ is the solar intensity at Earth, considered to be the optimal value of 1 kW/m$^2$. It can be seen that solar intensity is maximized at an incidence angle of zero degrees, corresponding to the solar rays coming in aligned with the surface's normal. Furthermore, as solar rays diverge from the perpendicular, its intensity decreases.

Given this behavior, the path of the sun becomes a pivotal factor in the design of solar energy systems. Due to the daily rotation of the earth about its tilted axis and its annual orbit around the sun, a solar device would require a two-axis tracking system in order to collect the maximum amount of solar energy available over the course of the year. However, the closer the position of the sun is followed, the higher the costs and system complexity will be. Thus, a reasonable balance between system complexity and maximum collectable energy must be determined.

## 2.2 Concentrated Solar Power

As detailed in Chapter 8 of [1], in solar energy applications, one must minimize heat losses in the collector in order to maximize the amount of useful heat captured from the absorbed solar energy. Because heat loss is directly proportional to surface area, a common way of improving the performance of solar collectors is to make them smaller. To avoid losing collection ability due to the decrease in size, solar concentrators are used to redirect light incident on a large area onto a smaller area by using mirrors (reflection) or lenses (refraction).

## 2.3 Optics

As explained in [3], the basic tool used in designing solar concentrators is geometrical optics, as it's essentially an optical system. The most important part of geometrical optics used in the design of solar concentrators is the theory of how light rays react when they make contact with a surface and are either reflected or transmitted. The fundamentals that describe the two possible scenarios are the Law of Reflection and the Law of Refraction (also known as Snell's Law).

Figure 2-2 is a representation of the Law of Reflection. The image shows a ray of light coming in at an incidence angle, $\theta_i$, with respect to the surface normal (dotted line) and going away from the surface at an angle of reflection, $\theta_r$, with respect to the normal. The Law of Reflection states that when light is reflected from a smooth surface, the angle of reflection is equal to the angle of incidence ($\theta_r = \theta_i$). Furthermore, both rays and the plane normal lie on a single plane.

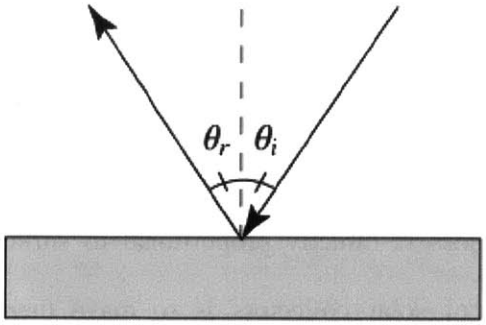


**Figure 2-2: Law of Reflection [4].**

Defining the vectors describing the incident ray, reflected ray and the normal (pointing away from the surface), as $\vec{r}$, $\vec{r}'$, and $\hat{n}$, respectively, the Law of Reflection may be expressed in vector form:

$$\vec{r}' = \vec{r} - 2(\hat{n} \cdot \vec{r})\hat{n}. \qquad \textbf{Equation 2-2}$$

Multiple solar concentrators use reflective surfaces to direct sunlight entering the aperture into the desired solar collector. Depending on the particular solar concentrator design, the type of receiver, and incident angle of the sun, the path the sun rays will take to reach the collector and the number reflections off the mirrors will vary. All reflective materials have a reflectivity factor, $\rho$, which describes what fraction of the energy an incident ray of light will be reflected; the remaining energy is absorbed in the mirror. Hence, for solar energy applications, the greater the numbers of reflections that a solar ray undergoes to reach the collector, the bigger the losses will be. The absorption losses in a reflective solar concentrator, $L_a$, are described by the following equation:

$$L_a = (1 - \rho^{<n>}), \qquad \textbf{Equation 2-3}$$

where $<n>$ are the average number of reflections.

Figure 2-3 depicts the Law of Refraction. In this situation, the ray of light with an angle of incidence, $\theta_1$, with respect to the surface normal is transmitted through a material at an angle

of refraction, $\theta_2$, with respect to the normal. The image also depicts the refractive indices of the media on either side of the refracting boundary, $n_1$ and $n_2$.

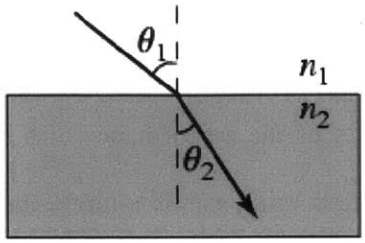


**Figure 2-3: Law of Refraction [5].**

Snell's Law states that the sine of the angle of incidence bears a constant ratio to the angle of refraction:

$$n_1 \sin\theta_1 = n_2 \sin\theta_2. \qquad \textbf{Equation 2-4}$$

Similarly to the Law of Reflection, it may be expressed in vector form:

$$n_2\vec{r}' = n_1\vec{r} + (n_2\vec{r}' \cdot n_1 - n_1\vec{r} \cdot n_1)n_1. \qquad \textbf{Equation 2-5}$$

As was the case with reflective solar concentrators, refractive lenses that are used to concentrate solar power also have losses to consider. When a ray of light is refracted by a lens, a fraction of its energy is reflected away at the refraction boundary. The reflective losses, $L_r$, of lenses depend entirely on the refractive index of the medium in which the ray of light is originally traveling in, $n_1$, and on the refractive index of lens material, $n_2$. This relationship is expresses as such:

$$L_r = \left(\frac{n_1 - n_2}{n_1 + n_2}\right)^2. \qquad \textbf{Equation 2-6}$$

## 2.4 Solar Concentrators

Some important metrics used to describe and compare solar concentrators are: concentration ratio, acceptance angle sensitivity to mirror and alignment errors, size of the reflector area, and the average number of reflections [6]. There are two types of concentration ratio that describe different aspects of the performance of a solar concentrator: geometric and optical. The geometric concentration ratio, $CR$ is entirely determined by the geometry of the concentrator and is defined as

$$CR = \frac{A_a}{A_r}, \qquad \textbf{Equation 2-7}$$

where $A_a$ is the area of the concentrator's aperture and $A_r$ is the area of the receiver. The optical concentration ratio takes into account the optical efficiency which is a metric that takes into account how much of the incident energy is lost due to the optical properties of the concentrator. For instance, for a reflective concentrator, the optical efficiency, $\eta_{opt}$, is defined as

$$\eta_{opt} = \sum_{i=1}^{i=R} \frac{\rho^{n_r}}{R}, \qquad \textbf{Equation 2-8}$$

where $R$ is the total number of rays and $n_r$ is the number of reflections of a ray in a concentrator before reaching the receiver. The optical concentration ration is metric that captures the ability of a solar concentrator to increase the amount of light energy available at the receiver based on its geometry and optical properties, as defined in Chapter 8 of [1]. This metric is usually referred to as the effective concentration ratio, $CR_{eff}$, and is described as

$$CR_{eff} = CR\ x\ \eta_{opt}. \qquad \textbf{Equation 2-9}$$

There are different types of solar concentrators typically used, reflective and refractive, and they have different performance metrics. With the collaboration of other students in the MIT Precision Engineering Research Group (PERG), four main concentrator designs were analyzed.

### 2.4.1 Fresnel Lens

Most of the research done regarding the Fresnel lens was done by Soraya Terrab, a student that visited MIT during the summer of 2012 as part of the MIT Summer Research Program. She worked on a solar cooker thermal storage unit which used a Fresnel lens as part of the design.

A Fresnel lens is a refractive solar concentrator that focuses the light incident on its aperture onto a distinct point or a line. Although the lenses usually have high concentration ratios, they also have high tracking requirements. This means that it has the ability to collect large amounts of energy as long as it closely tracks the position of the sun. Terrab made a model that examined the total energy that could be collected by a Fresnel lens as a function of both its lens aperture area and number of times it has to be moved to a new position. Terrab's model assumed a Fresnel lens with acceptance half-angle of 10° and a 96% efficiency, as well as a sun that sweeps a full 180° in a 12 hour period. At this rate of solar angular displacement, the Fresnel lens would have to be repositioned every 80 minutes to ensure sunlight is always within its acceptance angle, which would be an inconvenience for the user. Below are the results from her model:

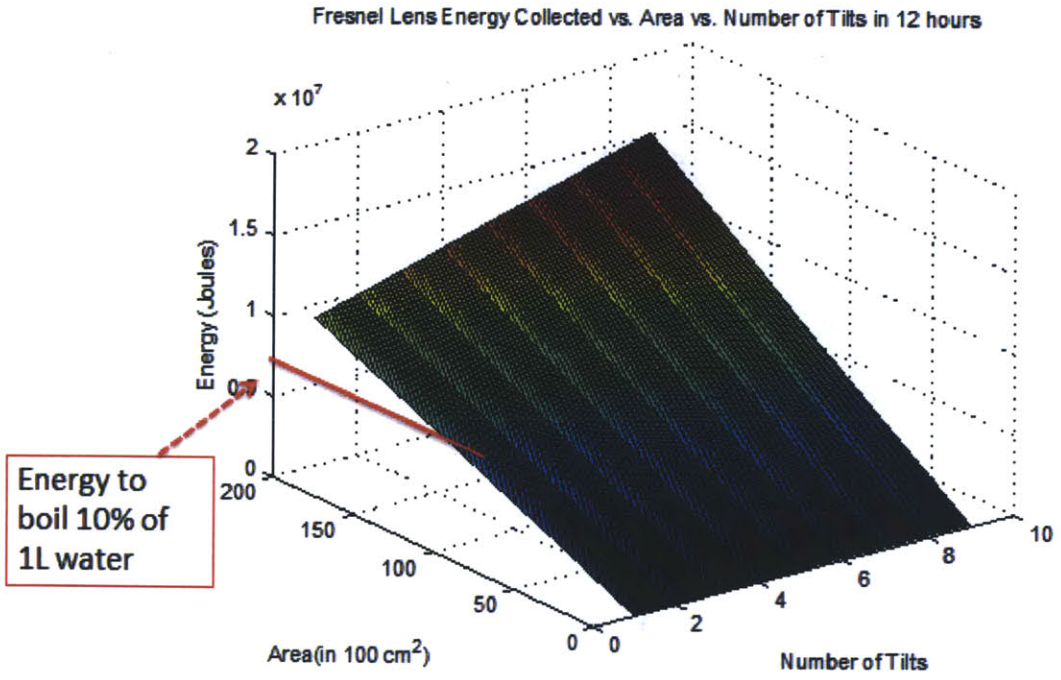


**Figure 2-4: Energy collection capabilities of a Fresnel lens with acceptance half-angle of 10° as a function of lens area and the number of position adjustments required to maximize energy collection in a 12 hour period.**

### 2.4.2 Flat Panels

Analysis of a flat panel concentrator was led by Daniel Bridgers, a graduate student in PERG. Bridgers built a Matlab model to characterize a two-dimensional flat panel reflector trough. Figure 2-5 shows the concentration ratio of a flat panel trough for different acceptance angles. In addition, Bridgers did studies that predict the efficiency of the system based on number of position adjustments and different aspect ratios (Figure 2-6). In summary, flat panel concentrators have low tracking requirements but can only achieve low concentration ratios.

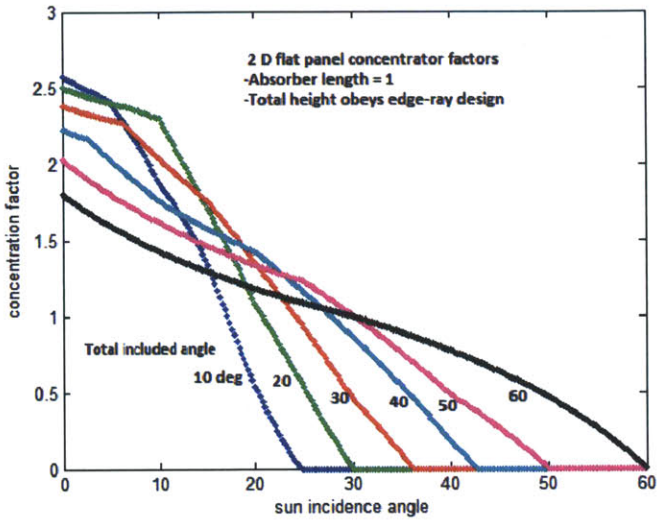


**Figure 2-5: Concentration ratio of 2D flat panel trough for different acceptance angles.**

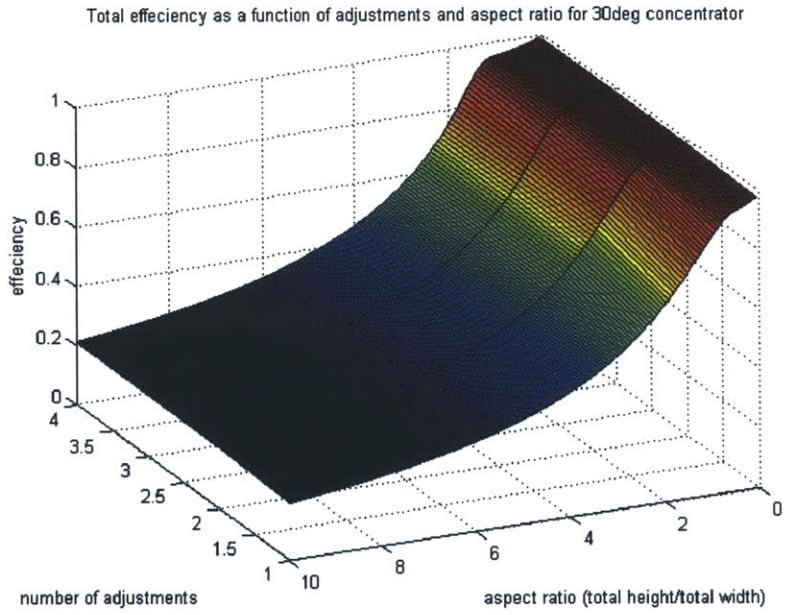


**Figure 2-6: Efficiency of 2D flat panel trough, with 30° acceptance angle, as function of trough aspect ratio and the number of adjustments required to maximize energy collection during a day.**

### 2.4.3 Parabolic Trough

Bridgers also took the lead in the analysis of a parabolic concentrator. Logically, the profile of a parabolic concentrator is a parabola, meaning that all incident rays of light parallel to the parabola's axis will be reflected towards the focus. Because of this, parabolic concentrators are usually used in trough designs where a cylindrical collector placed concentrically to the two-dimensional parabola's focus. This characteristic means that high concentration ratios may be obtained with this design as long as the axis of the parabola is aligned with the sun (see Figure 2-7). However, any small deviation in incidence angle causes the reflected rays to miss the focal point, which requires the parabolic concentrator track the sun's position closely. Additionally, Bridgers made a model to analyze the behavior of the parabolic trough's efficiency for different incidence angles of the sunlight and trough aspect ratios (see Figure 2-8).

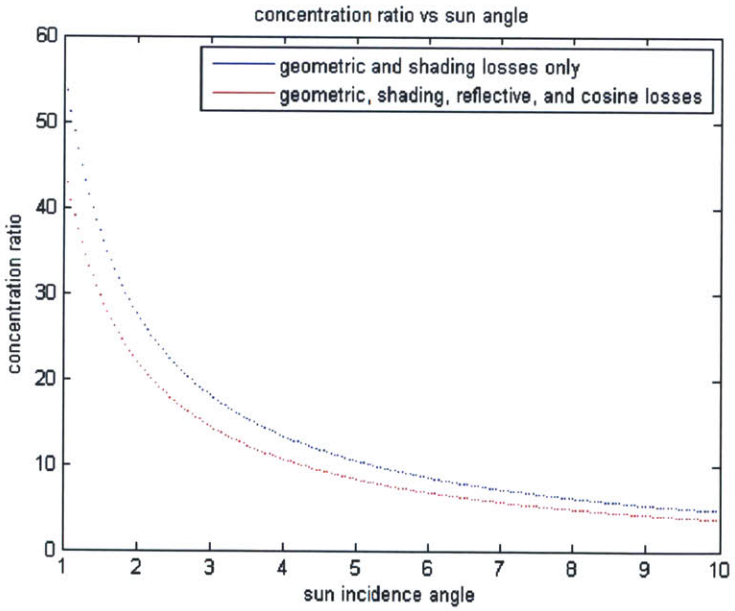


**Figure 2-7: Concentration ratio as a function of incidence angle for parabolic trough with tube collector along focus.**

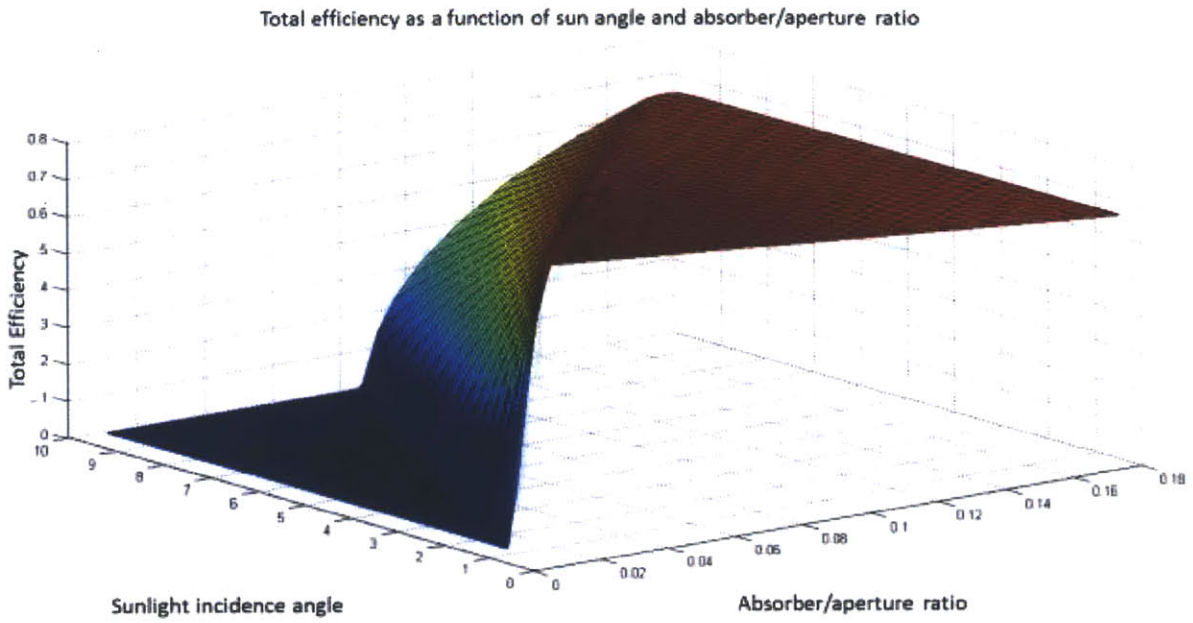


**Figure 2-8: Efficiency of parabolic trough as a function of solar incidence angle and absorber/aperture aspect ratio.**

### 2.4.4 Compound Parabolic Concentrator

The compound parabolic concentrator (CPC) is an example of a non-imaging concentrator, meaning that all the light rays captured are reflected onto a region rather than focused on a point. Figure 2-9 shows the two-dimensional theoretical shape of the CPC:

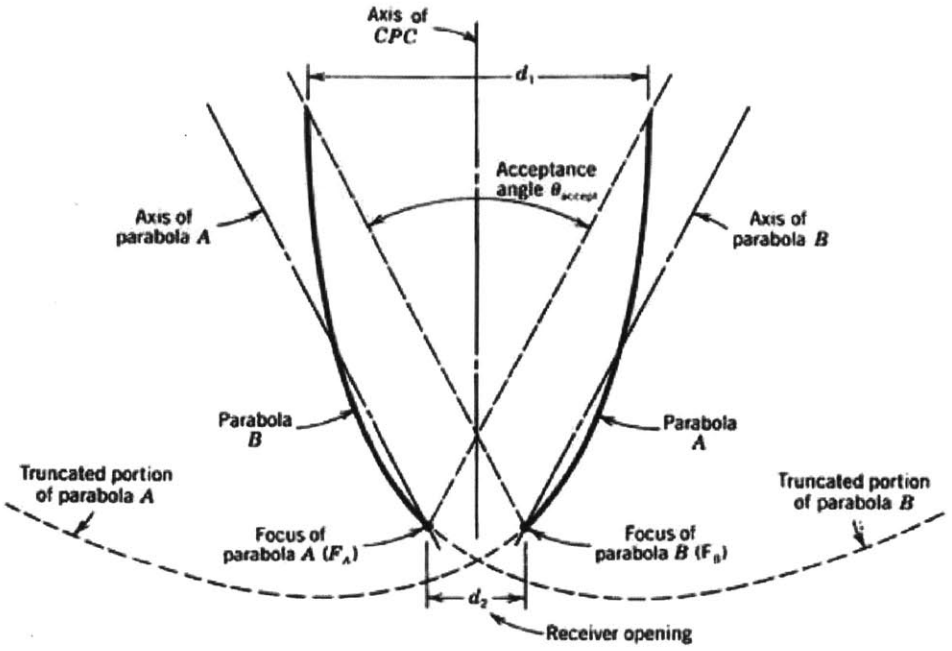


**Figure 2-9: Two-dimensional profile of a compound parabolic concentrator (CPC) [1].**

As shown, the profile of the CPC consists of mirror segments of two parabolas, *Parabola A* on the right and *Parabola B* on the left, with different focal points, $F_A$ and $F_B$, respectively; the focus of each branch is at the point where the opposite branch meets the receiver, labeled *Receiver opening* in the figure. The height of the theoretical CPC is also defined; the branch of each parabola extends between the *Receiver opening* and the point at which the slope of the curve is parallel to *Axis of CPC*.

By definition, the axis of each parabola passes through its focal point. The angle the axes of the parabolas make with the axis of the CPC, labeled *Axis of CPC*, defines the acceptance angle, $\theta_{accept}$, of the concentrator. The acceptance angle defines the maximum incidence angle at which light entering the aperture will reach the receiver. If the incidence angle of the light is smaller than half the acceptance angle, light will be reflected through the receiver (see Figure

2-10a). Otherwise, the ray of light will reflect its way out through the aperture of the concentrator (see Figure 2-10b).

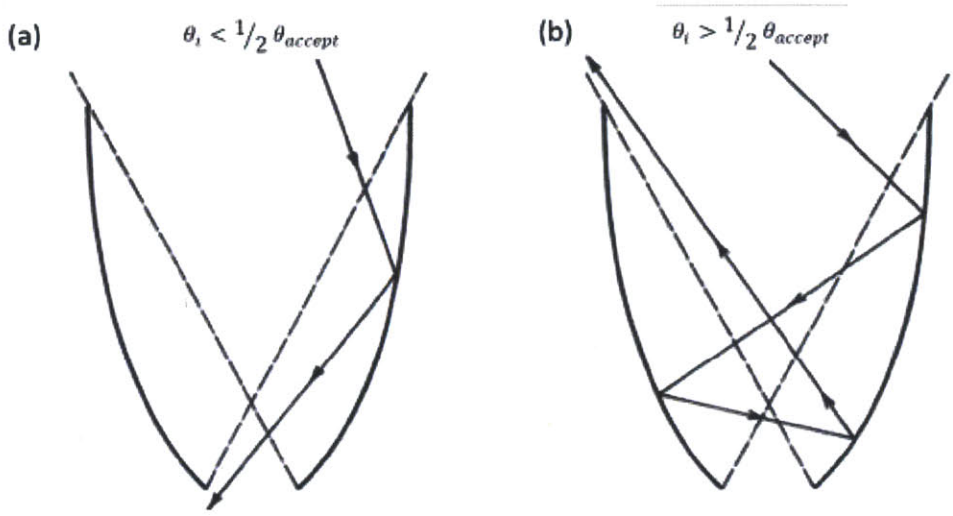


**Figure 2-10: Reflection of light within a CPC - (a) incidence angle less than half-acceptance angle; (b) incidence angle greater than half-acceptance angle (from Chapter 9 of [1]).**

Due to the reflective symmetry about the axis of the CPC, a different convention was used from this point forward in order to define the CPC parameters using half of the profile; Table 1 summarizes the relationship between the two naming conventions.

**Table 1: Thesis notation of CPC design parameters as compared to [1].**

| | Figure 2-9 | Thesis |
|---|---|---|
| Aperture | $\frac{d_1}{2}$ | $a$ |
| Exit/Receiver | $\frac{d_2}{2}$ | $b$ |
| Acceptance angle | $\frac{\theta_{accept}}{2}$ | $\theta_a$ |

To fully constrain the design of a CPC, only two of the three dimensions from Table 1 have to be defined because they are related by

$$a = \frac{b}{\sin\theta_a}. \qquad \textbf{Equation 2-10}$$

Also, these parameters define the concentrator's height, $H$, as

$$H = (a + b)\cot\theta_a. \qquad \textbf{Equation 2-11}$$

Once fully defined, the profile shown in Figure 2-9 may be used to design a two-dimensional or three-dimensional CPC; the 2D CPC is obtained by extruding the profile along the length of a trough, while the 3D CPC is obtained by revolving the profile around the concentrator's axis. The concentration ratios are described by

$$CR_{2D} = \frac{1}{\sin\theta_a}, \qquad \textbf{Equation 2-12}$$

and

$$CR_{3D} = \frac{1}{(\sin\theta_a)^2}, \qquad \textbf{Equation 2-13}$$

for the 2D and 3D configurations, respectively.

Figure 2-11 shows a plot of the concentration ratio that can be obtained by the 2D CPC depending on the chosen acceptance half-angle. As seen, moderate concentration ratios may be obtained with a CPC design, higher than flat panel reflectors but lower than a parabolic trough or Fresnel lens. As a general principle: the smaller the acceptance angle, the more closely the sun must be tracked. Compared to the other concentrators, the CPC provides a compromise between low tracking requirements and moderate concentration ratio. A drawback of the CPC design is its high aspect ratio (height:aperture) required to follow the theoretical geometry. However, it has been determined that some portion of the CPC may be truncated without much loss in

performance [6]; thus, the height of the concentrator can be reduced without dramatic decreases in the concentration ratio.

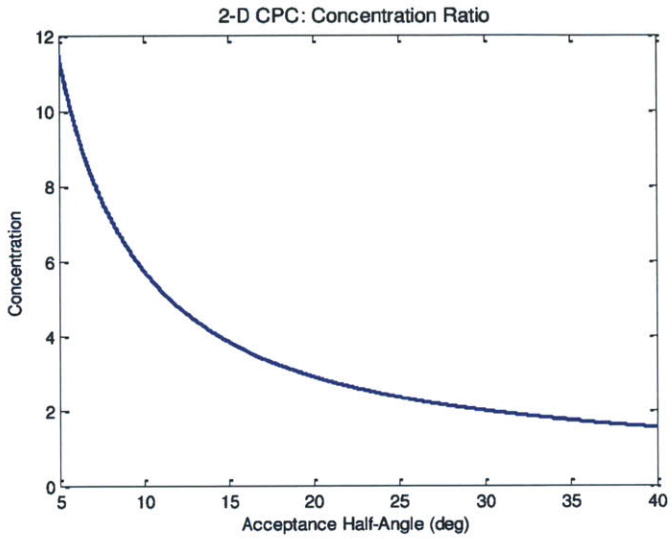


**Figure 2-11: Theoretical concentration ratio of the 2D CPC.**

## 2.5 Prior Art

As Chapter 3 will outline, the proposed solution to the problem statement was an inflatable 3D compound parabolic concentrator. In order to maximize efficacy of the design process, different existing technologies related to the concept of interest were researched. One such device was an inflatable solar collection balloon, patented by the company Cool Earth Solar, which is currently being developed as a solar energy collection device (see Figure 2-12). The balloon is made of a clear top film and a reflective bottom film; both assume the shape of a spherical dish when the structure is inflated. Sunlight enters the balloon through the top film and is reflected off of the bottom film into its focal point where a photovoltaic receiver is located for collection of the reflected light.

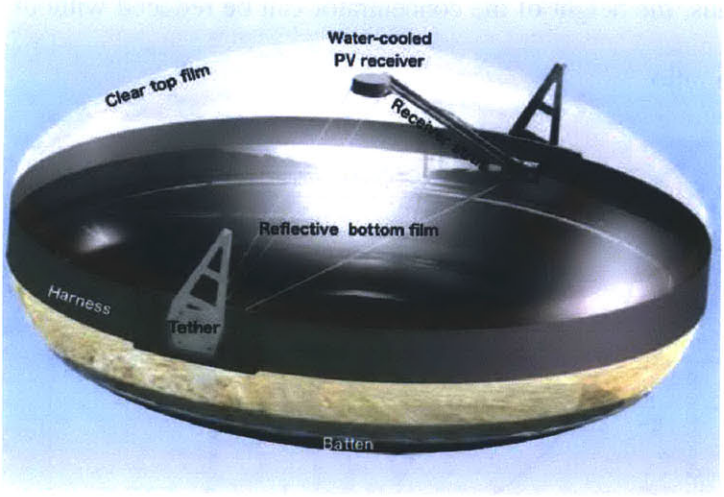


**Figure 2-12: Cool Earth Solar's inflatable solar balloon concept [7].**

The patent for inflatable solar balloon [8] was used to learn about the details regarding the fabrication and operation of the proposed device. The device was designed such the films could be bonded into a flat stack assembly. In addition, it allows for the addition of features and materials to help reinforce the structure: external circumferential harness, film attachments to reduce stress concentrations and modify inflated shape, and a support from a truss-like structure.

The citations made by this patent, as well as the most recent inventions that have reference the inflatable solar balloon, were used as baseline to conduct an extensive search that captured the development of portable and inflatable radiation reflection systems over time. The patents studied were grouped into two basic categories: inflatable reflectors and solar energy collection systems. Most of the patents, regardless of the intended application, describe a similar concept that uses two flexible membranes, one transparent and another reflective, bound around their edges to create a space that is pressurized to give shape to the structure. The following

sections will highlight some of the patents that are representative of the most common design and manufacturing processes for inflatable, solar collection devices.

### 2.4.1 Inflatable Reflectors

[9] describes a process using pressurized fluid to shape a reflective surface, something that has been replicated by multiple inventors. Two circular sheets of a pliant resilient plastic, one transparent and another coated with a reflecting metal, are attached around their circumference. The empty space between the sheets is filled with pressurized air, which imparts a curvature on the sheets. Figure 2-13 shows two images extracted from [9].

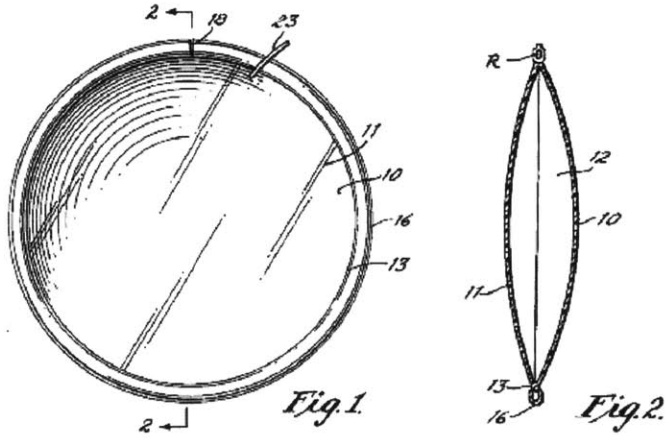


**Figure 2-13: Images of a patent for an inflatable curved mirror [9].**

In [10], an inflatable mirror that may be formed into a permanently rigid structure is described. This invention was designed for outer space; a mirror structure capable of being assembled in space and used to concentrate solar energy to several collectors. Similar to the previous patent, a mirror lens is attached to an outer ring and upon inflation it assumes a parabolic shape (see Figure 2-14a). The differences are: (1) the outer ring is also an inflatable and may be filled with a liquid material that solidifies to give rigidity, and (2) the inflation

chamber is provided by a construction element that is removed after the mirror has been shaped (see Figure 2-14b). This is possible because the mirror lens is formed by a double wall membrane that is filled with the same solidifying liquid material used in the outer ring, which fixes the mirror into a parabolic shape after inflation. Unlike the previous patent, sun radiation enters directly to the reflector instead of going through an inflation chamber.

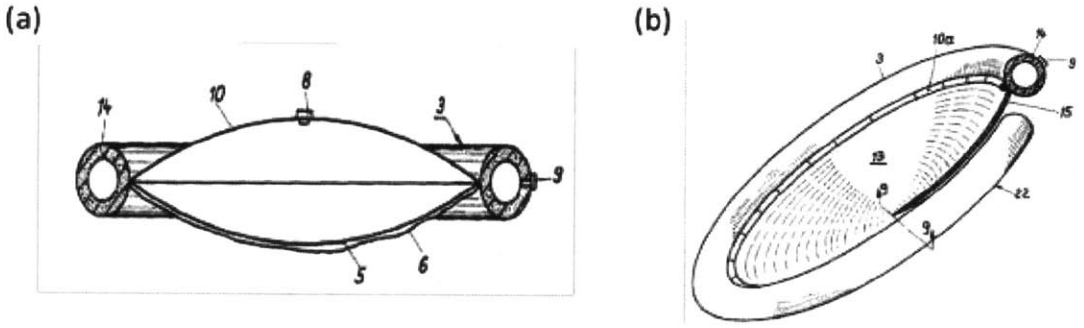


**Figure 2-14: Images of patent describing inflatable mirror structure capable of being permanently formed into a rigid structure [10].**

### 2.4.2 Collection of Solar Energy

[11] discusses an inflatable solar collector that also uses the concept of an upper transparent flexible film and a lower sheet coated with a reflective metal which form a space in between to be inflated by a pressurized fluid. Tubes carrying a working fluid are placed inside the enclosure such that the solar rays reflected by the lower sheet are concentrated on them.

# Chapter 3: Design Concept Generation

## 3.1 Strategies

In order to build a light-weight, portable compound parabolic concentrator, a wide variety of products in the market that contain these qualities were examined, some of which were inspiring during the design generation and brainstorming process. The main design strategies considered were foldable, collapsible, and inflatable structures.

The inspiration for the foldable or collapsible structure came from common kitchenware. Recently, products in this industry are being designed to save up space in the kitchen when they are not being used. Two examples of these are a foldable (Figure 3-1) and collapsible (Figure 3-2) colander.

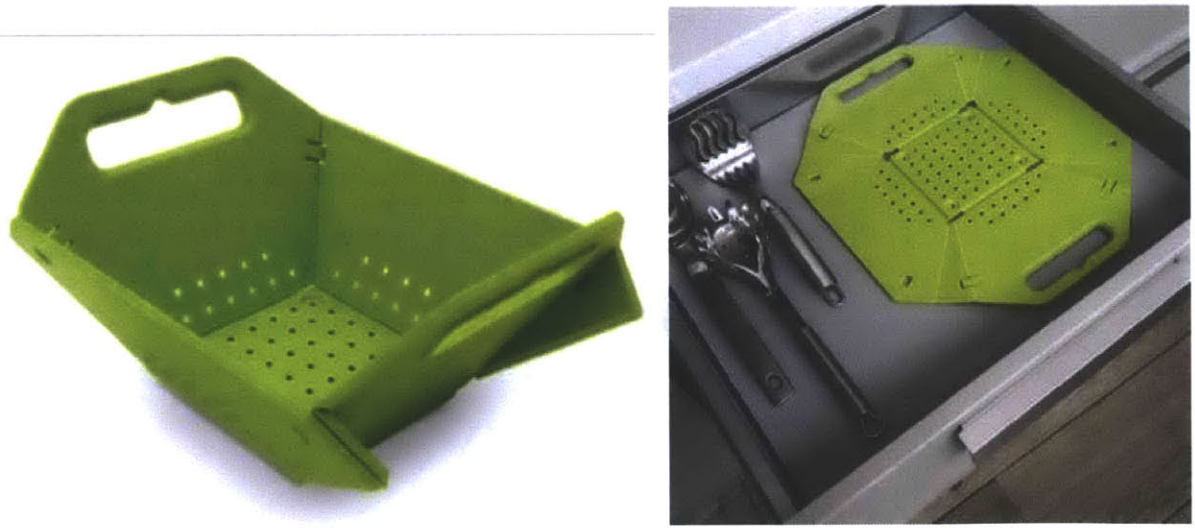

**Figure 3-1: Foldable colander in both its configurations [12].**

**Figure 3-2: Collapsible colander in both of its configurations [13].**

Both of these products are designed to minimize the amount of space needed for storage, while allowing for the same functionality as their non-foldable/non-collapsible counterparts. This feature is particularly desirable for traveling equipment; one example is a metallic collapsible cup, as shown in Figure 3-3.

**Figure 3-3: Collapsible cup [14].**

The third strategy was an inflatable structure. Inflatable structures bring to mind images of air mattresses and bouncy houses, but are actually quite versatile. In general, inflatables are

used for equipment that must be easily transported and fairly easy to assemble when it must be used.

Comparing the three strategies, they all provide a certain level of portability but vary in weight depending on the type of material. Other differences include their footprint and volume when in their stored configuration and the number of moving parts. Both colanders are manufactured in one part and the ability to fold and collapse is added in by incorporating recesses into the design. In contrast, the cup in Figure 3-3 shows a collapsible structure with multiple moving parts. Additionally, the manufacturing process for inflatables consists of connecting different fabrics in predetermined patters. Once assembled, the procedure to make and inflatable ready for use is relatively more complex than the other strategies because it will most likely require a pump to inflate in a timely manner.

Considering all strategies and their ability to meet the functional requirements, the inflatable structure was chosen. The main reason for this decision was that the footprint of the foldable and collapsible structures during their stored configuration is constrained by their ready-for-use dimensions. Inflatable structures have considerably less volume when stored than during their fully inflated states due to the lack of pressurized air, allowing the inflatable to be stored in a more compact manner. Furthermore, the idea of an inflatable solar concentrator is highly creative, innovative, and worth exploring.

## 3.2 Concept Selection

The extensive search for prior work on inflatable concentrator technology, detailed in Section 2.4, led to development of two design concepts: enclosed (Figure 3-4a) and open (Figure 3-4b).

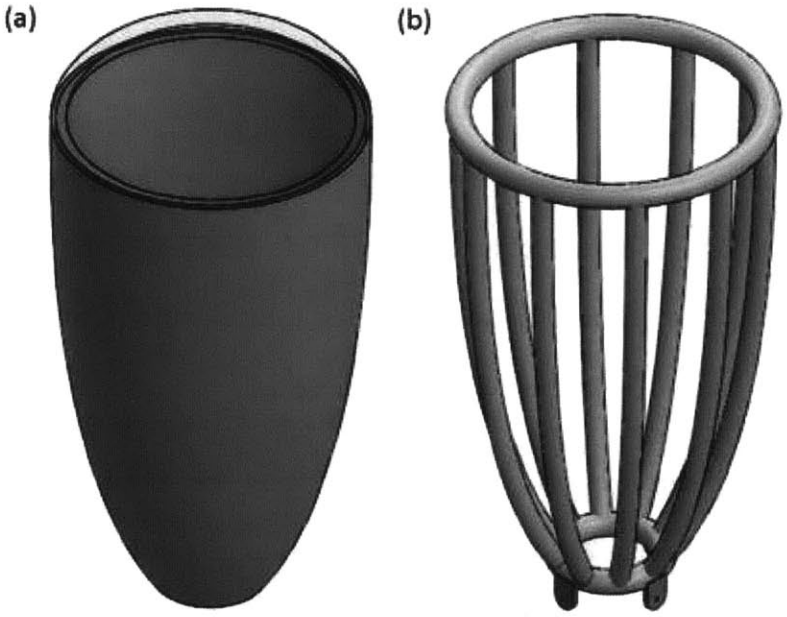


**Figure 3-4: Design concepts for inflatable solar concentrator - (a) enclosed envelope and (b) open, inflatable frame.**

The first concept consists of attaching elastic membranes along their edges to enclose an envelope that may be inflated with a pressurized fluid. Figure 3-4a is a representation of a three-dimensional CPC that could be made with the combination of two types of elastic membranes, one transparent and the other reflective, of varying thicknesses such that a desired non-spherical shape may be obtained. The top membrane would be transparent to allow the sunlight to enter the concentrator, while the bottom membrane would have to be reflective on the inside to direct entering sunlight towards the concentrator's exit. The sides of the reflector would be made of a

reflective flexible membrane or a plastic with a coat of reflective material on its inside. Additionally, the walls may be encased by an external plastic sheet to provide rigidity. Once the membranes are sealed around their edges and the gap between has been them pressurized, the concentrator would be placed on top of a collector.

The advantage of the enclosed concept is that the reflective surface is completely sealed off from the environment. Consequently, no dirt or dust can accumulate on the reflective surface which may decrease the optical efficiency of the system. Another advantage is that the manufacturing process will be fairly simple, only requiring the sheets of material to be joined together. One of the biggest drawbacks of this concept is that it requires light to be refracted through the transparent membrane in order to enter the concentrator. As detailed in Section 2.3, when rays of light are refracted, a fraction of the ray is reflected and energy is lost. In addition, having the reflective region closed off would make it difficult to access in the future for maintenance or repairs.

The idea behind the second concept is to leave the structure open to the environment and eliminate the need for sunlight to be refracted into the concentrator. As shown in Figure 3-4b, this concept consists of creating inflatable ribs and support rings to provide a rigid structure for the concentrator. By allowing light to enter the aperture directly without going through a transparent membrane, reflective losses are eliminated and a higher amount of solar energy is captured. This concept requires the manufacturing of independent reflective segments, which may be vacuum formed, to be attached to the ribs filling up the space between them. These segments may be made from a naturally reflective material or from some other material that is well-suited for the selected manufacturing process, and is later coated with a reflective film.

An advantage of the open frame concept is that it does not require the structure to be inflated exclusively with air, and as such the fluid won't be in the sunlight's path. There are existing products that provide the ability to inflate a structure with a fluid that solidifies with time (e.g., expanding foam), providing a rigid structure once inflated. This may not be ideal if the user wants to deflate the concentrator after some period of time, but it is still a possibility. Since the reflective surfaces are exposed to the environment, they are easy to access if needed for any repairs, maintenance, or modifications; but this means that it will also be exposed to dust, dirt and other particles that will deteriorate the optical efficiency of the system. From a manufacturing standpoint, building and assembling this inflatable model would be more complex given that the reflective surfaces must be made separately and incorporated into the rib structure.

During the concept evaluation process, Otherlab was contacted for consultation. Otherlab is a private research and development company based in San Francisco, CA, with experience in the design and manufacturing of inflatables consisting of complex geometries. Both concepts were run through Otherlab, and their input was taken into account given their expertise. They expressed concern regarding the closed concept because of its dependence on the ability of the transparent plastic membrane to refract light into the system. Otherlab pointed out that ultraviolet light emitted by the sun deteriorates plastics. To prevent this, it could be treated with the cost of jeopardizing its transparency, which would amplify reflective losses and eliminate the efficiency of the system. After careful consideration, it was decided to move forward with the open inflatable frame design and avoid these risks.

# Chapter 4: Analytical Model

## 4.1 Overview

Another consideration in an attempt to simplify the manufacture of the inflatable concentrator was making reflective facets out of straight sections, rather than a parabolic curved wall as suggested by the theoretical CPC design (Figure 4-1a). From a manufacturing standpoint, it is simpler and cheaper to work with flat sections than having to go through the necessary processes to form materials into a specific shape permanently. In addition, using straight sections along the height of the concentrator connected to the inflatable ribs means that the shape of the top-view cross-section will no longer be a circle, as it would be in the theoretical 3D CPC. Instead, the cross-sectional shape with be a polygon, where the number of inflatable ribs defines the number of sides in the polygon (Figure 4-1b).

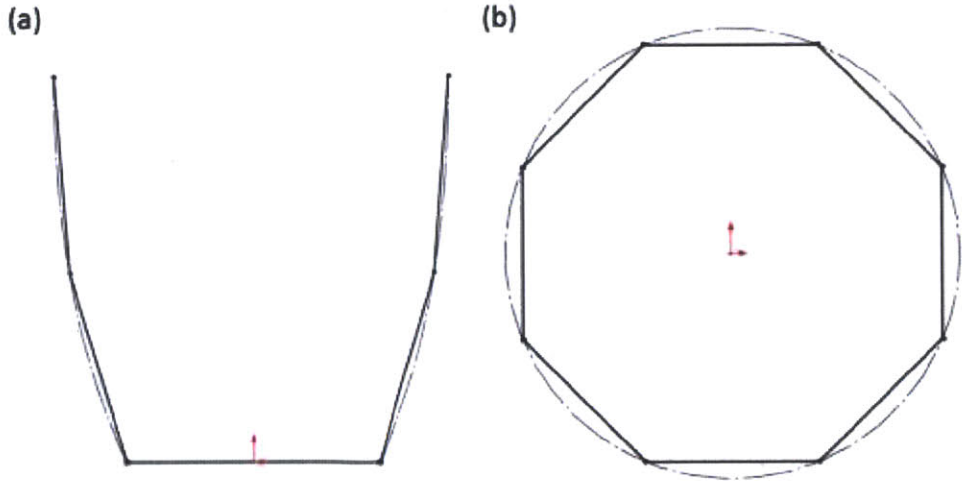


**Figure 4-1: CPC approximation using flat sections - (a) 2D profile using flat segments to approximate parabolic curve and (b) top cross-sectional view of polygon approximating circular geometry.**

As seen in Figure 4-1a, the parabolic-shaped wall of the CPC (dotted line) may be substituted by flat sections. Intuitively, as the number of flat segments increases, the wall geometry will more closely approximate the theoretical parabolic curve. Figure 4-1b depicts a top view of the concentrator's cross-section showing the theoretical circular geometry (dotted line) approximated by the polygon created by the ribs (corners of the polygon) and the reflective facets (sides of the polygon). This specific example shows the geometry for a design using eight ribs, thus the cross-sectional view of the aperture assumes an octagonal geometry. In this view, the same concept as in the side cross-sectional view applies, as the number of ribs increases, the number of sides in the polygon increases and the cross-sectional geometry more closely approximates a circle.

Besides the usual design parameters that must be selected for the design of a typical compound parabolic concentrator, the proposed design requires the selection of two others: the number of flat sections in each facet and the number of inflatable ribs. In order to make a sound engineering decision, the direct effect of each of these two factors on the optical efficiency must be determined. The approach was to build an analytical model of the concentrator that predicts the efficiency of the system as a function of different solar incidence angles, the number of panels and the number of ribs used. This model would then be tested with prototypes by comparing the experimental and theoretical results to understand the accuracy of the model. Having an accurate analytical model of the system is a powerful design tool because it provides the means to determine the key design parameters to meet any specific set of requirements for a given application.

## 4.2 Ray tracing: First-order approximation

The analytical model for this design was a ray tracing code (using Matlab) that would calculate the efficiency of the solar concentrator for different solar incidence angles as the number of flat segments and ribs were iterated. The strategy was to model a two-dimensional view of the concentrator profile and understand the behavior of an evenly distributed source of light entering the aperture. For the first-order approximation, the goal was to build a simple model that would help guide the design process. In the ray tracing program, only rays going into the collector with zero or one reflection were accounted for and only one half of the reflective profile was considered.

To describe the reflective surfaces of the concentrator, the explicit equations of the parabolic branches were derived. Since these are tilted parabolas, the equations were described based on a rotated coordinate system (U-V axes). Figure 4-2 shows a graphical representation of the CPC in the rotated coordinate system corresponding to the right branch of the CPC. However, all the known parameters are specified in a coordinate system where the vertical axis is aligned with the axis of the CPC (X-Y axes). Thus, a supplementary Matlab code was written to transfer points between coordinate systems.

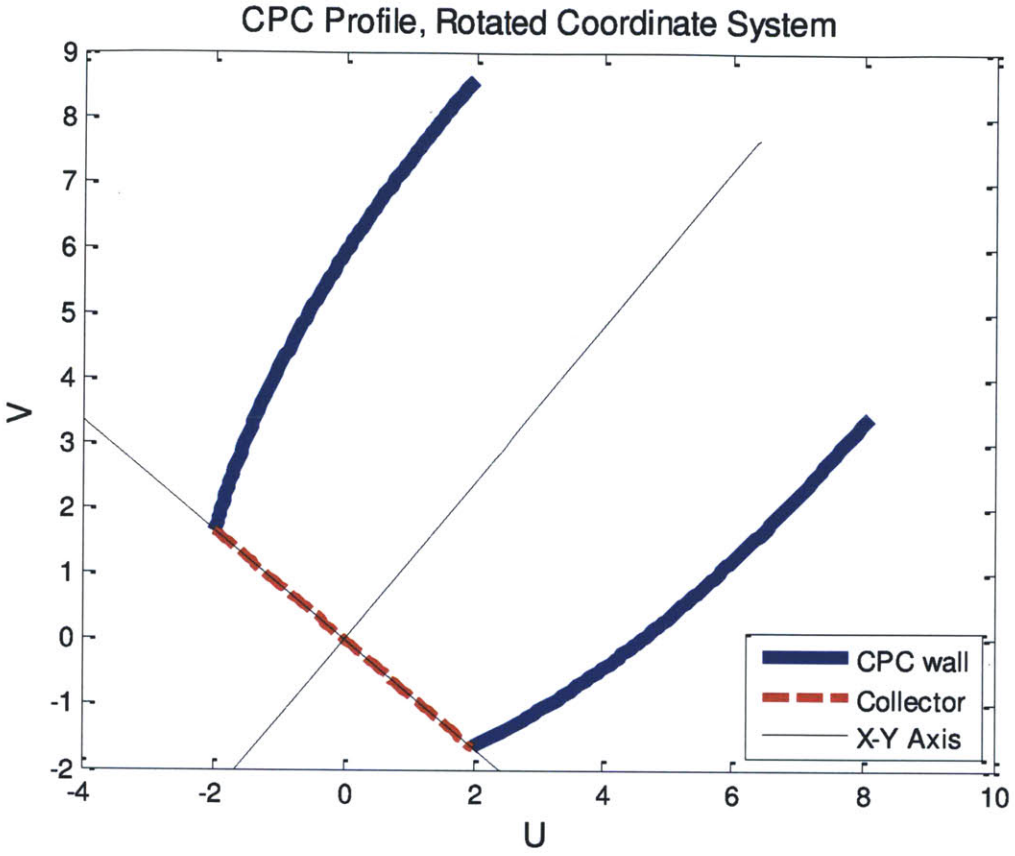


**Figure 4-2: CPC profile in a rotated coordinate system, as seen from the right branch.**

As seen in Figure 4-2, the U-V coordinate system is rotated with respect to the X-Y coordinate system about the origin by half the acceptance angle of the CPC such that the axis of the parabola is coincident with the V-axis. Given this orientation and the known dimensions of the parabola, the equation of each branch was determined.

The proposed design is based on the premise that the facets between the ribs, made of a number, $n$, of flat panels compose the reflective region in the concentrator. In a two-dimensional view of the model, the flat panels are seen as lines which approximate the parabolic branch of the ideal CPC. To derive the equations of the straight segments, the range along the U-axis between

the collector and aperture was divided into $n$ intervals; the lines connecting the endpoints between each interval represent the flat panels in the model.

The other component that had to be characterized was the incident light. The rays of light were described parametrically using the points of entry along the aperture and the angle of incidence. To ensure an even distribution of incident light, the points of entry were obtained by using the endpoints of equal intervals along the length of the aperture.

Using the equations for the light rays, reflective segments, and the collector, the intent of the Matlab code was to utilize a curve intersection script to determine where each ray of light intercepts the concentrator, whether it goes directly to the collector or undergoes a reflection. If the ray intersects one of the reflective segments, the code uses Equation 2-2 to compute the equation of the reflected ray.

### 4.2.1 Number of Reflective Panels

The first analytical model was used to understand the effect that the number of reflective panels used in each facet has on the optical efficiency of the concentrator for different angles of incidence. It is important to note that this model ignored the varying size of the collector depending on the number of inflatable ribs used; it was assumed that the size of the collector is constant and covers the entire distance across the two-dimensional side cross-sectional view. In the Matlab ray tracing code, loops were used to iterate through different angles of incidence for the rays of light and different number of reflective panels along the wall of the concentrator. Below is a plot showing how the first-order ray tracing program works:

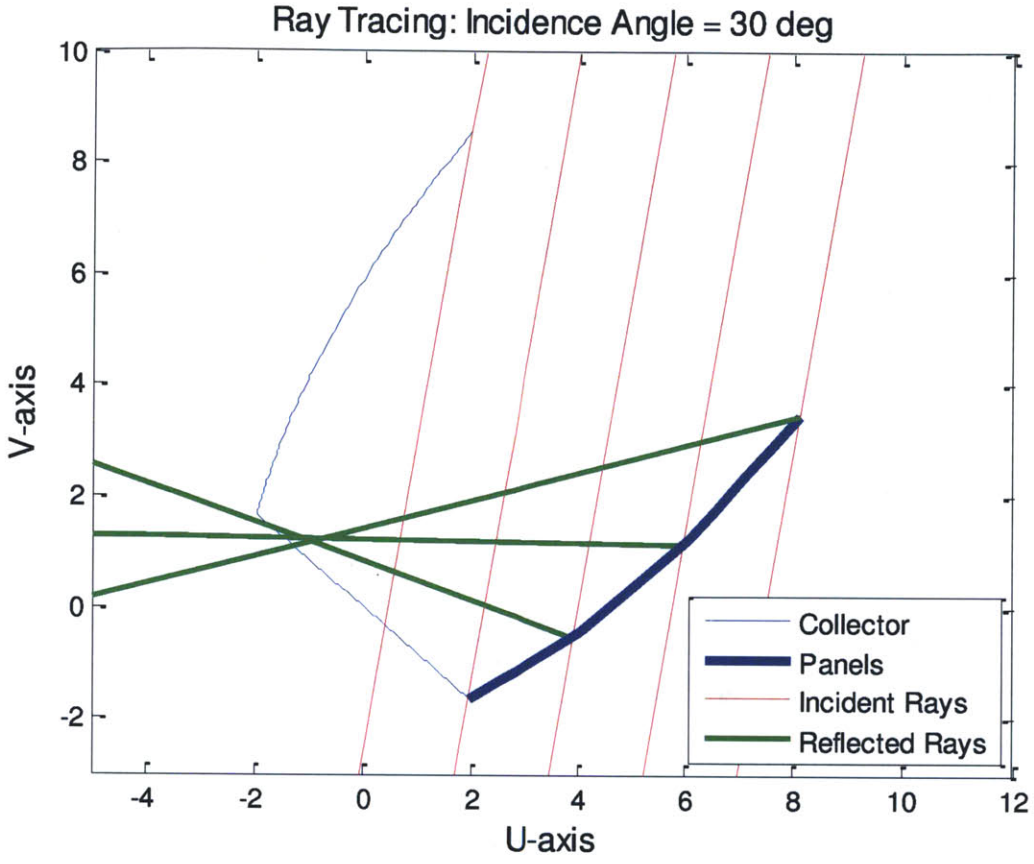


**Figure 4-3: First-order ray tracing analysis for varying number of panels; incidence angle of 30° entering concentrator profile containing three reflective panels along walls**

Figure 4-3 is a graphical representation of the first-order ray tracing model used to capture the effect of using different number of reflective panels in each facet; the other branch seen in the cross-section is only shown to provide perspective of the geometry of profile. As mentioned, the reflective panels along this other branch were ignored in this first-order model. This particular example depicts a scenario of five rays of light at an incidence angle of 30° entering the aperture of a concentrator with three panels along its reflective walls. From the five evenly distributed incident rays (red), two reach the collector (dotted blue line) directly and the other three are reflected (green) off of the panels (solid blue) at different points along the length of the concentrator. The three incident rays that are reflected reach different panels, which

explain why all three reflected rays have different orientations. In this specific scenario, all incident rays reach the collector with at most one reflection. However, two of the limitations of this first-order model are that if rays were to reach the other branch of the profile a reflection wouldn't be recorded, and if the rays were theoretically going to bounce off a second reflective panel and still reach the collector, it would be considered a loss in the efficiency calculation.

To fully capture the effects of solar incidence angle and number of reflective segments on the optical efficiency, the ray tracing code sweeps through different scenarios and calculates the optical efficiency for each one. The results were plotted in a three-dimensional surface graph:

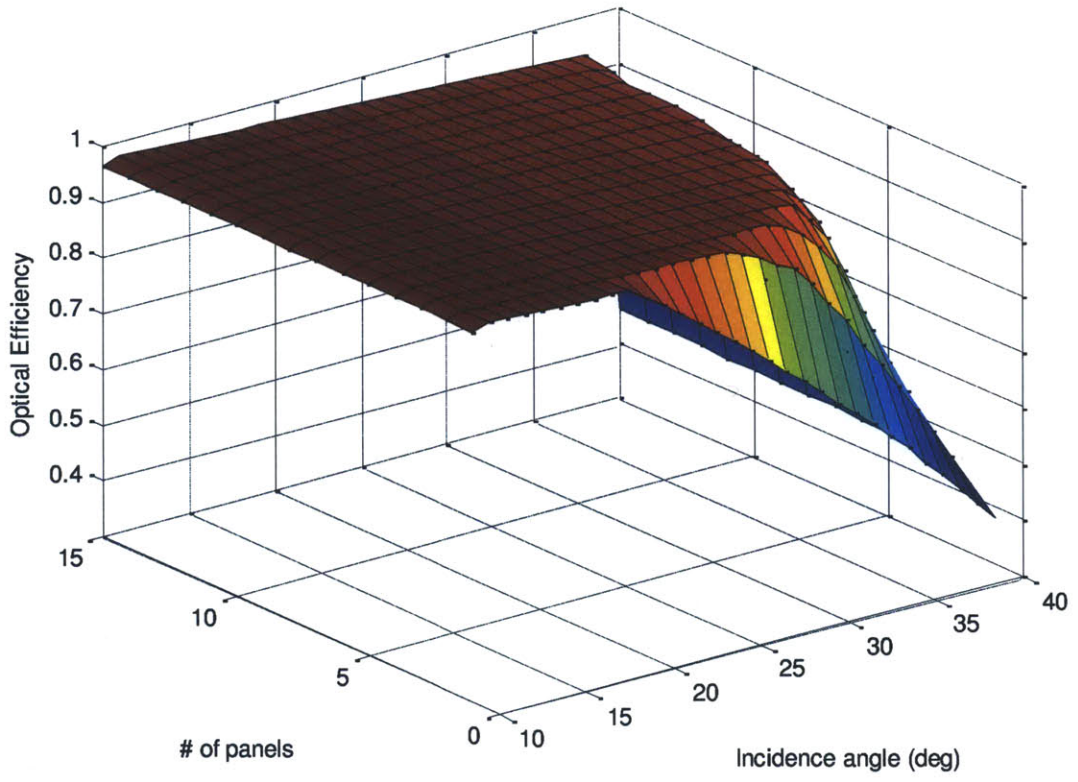


**Figure 4-4: First-order ray tracing model results - optical efficiency as a function of incidence angle and number of reflective segments. (Acceptance half-angle: 40°)**

The first observation made from Figure 4-4 was that, as expected, efficiency increases as incidence angle approaches 0° (perfectly aligned with the axis of the concentrator), and as the number of panels increases (reflective wall geometry gets closer to the theoretical parabolic shape of the CPC). However, it was observed that increasing the number of panels used to approximate the parabolic branch had diminishing returns in optical efficiency. For small incidence angles there is practically no benefit in using high number of panels, but at larger incidence angles, still within the acceptance angle of the design, there is. Figure 4-5 is an alternate view of Figure 4-4 that shows the optical efficiency dependency on the number of panels for lager angles of incidence:

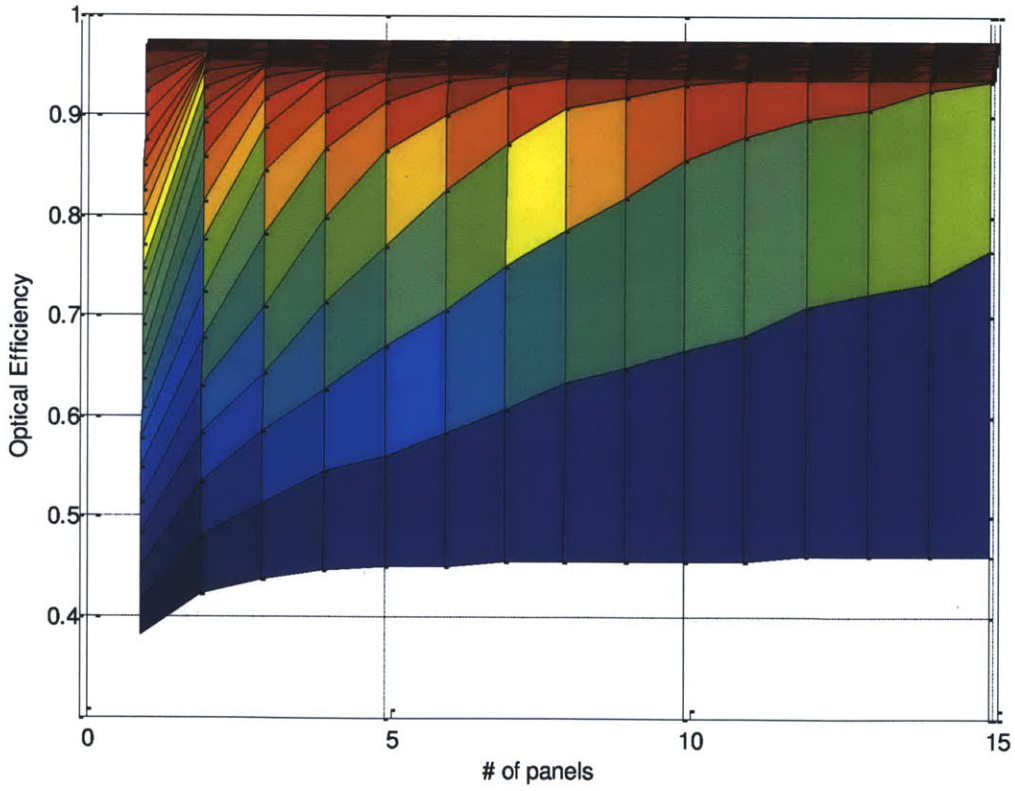


**Figure 4-5: Alternate view of first-order ray tracing model results – optical efficiency as a function of number of reflective panels; higher curves indicate smaller incidence angle.**

The view in Figure 4-5 depicts the effect of the number of panels on optical efficiency more clearly; it shows the region corresponding to larger incidence angles. As the incidence angles decrease (higher curves in the plot), overall efficiency increases and the point of marginal diminishing returns for number of panels is reached with smaller number of panels. In other words, the maximum efficiency of the system with a parabolic wall (equivalent to an infinite number of panels) can be approximated fairly closely by using a small number of panels. For example, in the model of this concentrator with an acceptance half-angle of 40°, at an incidence angle of 30°, the maximum optical efficiency with fifteen reflective panels, 94.65%, can be obtained with just four panels.

### 4.2.2 Number of ribs

Changing the number of inflatable ribs in the design effectively changes the size of the collector by changing the number of sides on the polygon-shaped cross-section as seen from a top view. As the number of ribs increases, the cross-section more closely approximates circle which is the theoretical shape of the three dimensional CPC. This relationship is graphically demonstrated in Figure 4-6:

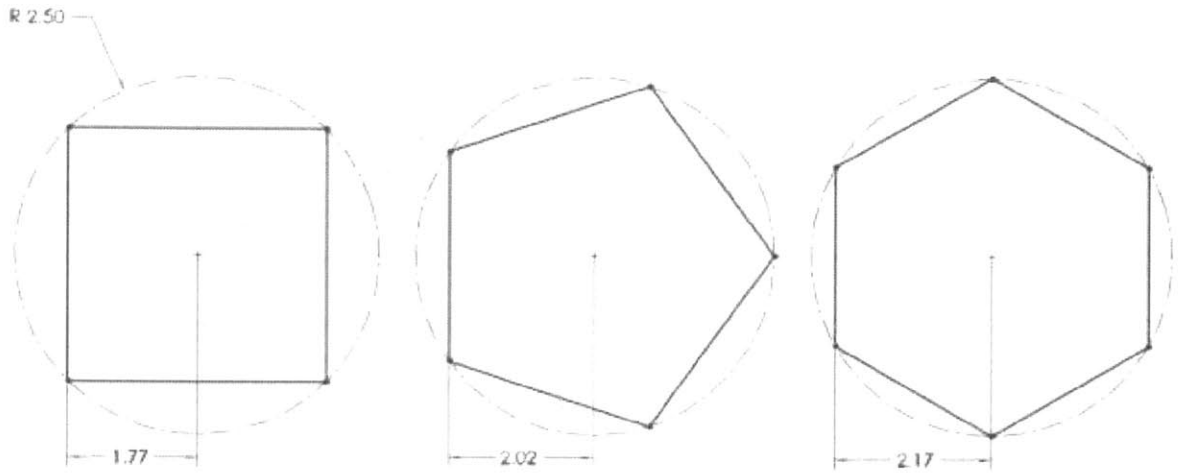


**Figure 4-6: Top view of concentrator cross-section showing relationship between larger number of polygon sides and larger apothem.**

Figure 4-6 shows polygons inscribed in circles of the same diameter with the distance of the apothem, which is the distance between the center (concentrator axis) and the side (reflective panels) of the polygon. As expected, the length of the apothem increases for polygons with a higher number of sides.

To analyze the effect of the number of ribs on the optical efficiency of the concentrator, the previous model was modified slightly to produce two new models. Firstly, a model was built where the number of panels in each facet was fixed and the optical efficiency was calculated for different incidence angles and number of ribs. Secondly, the optical efficiency dependency on the number of panels and the number of ribs was calculated for a given incidence. Below is a graphical representation of first-order ray tracing analysis done to analyze the effect of changing the number of ribs in the design:

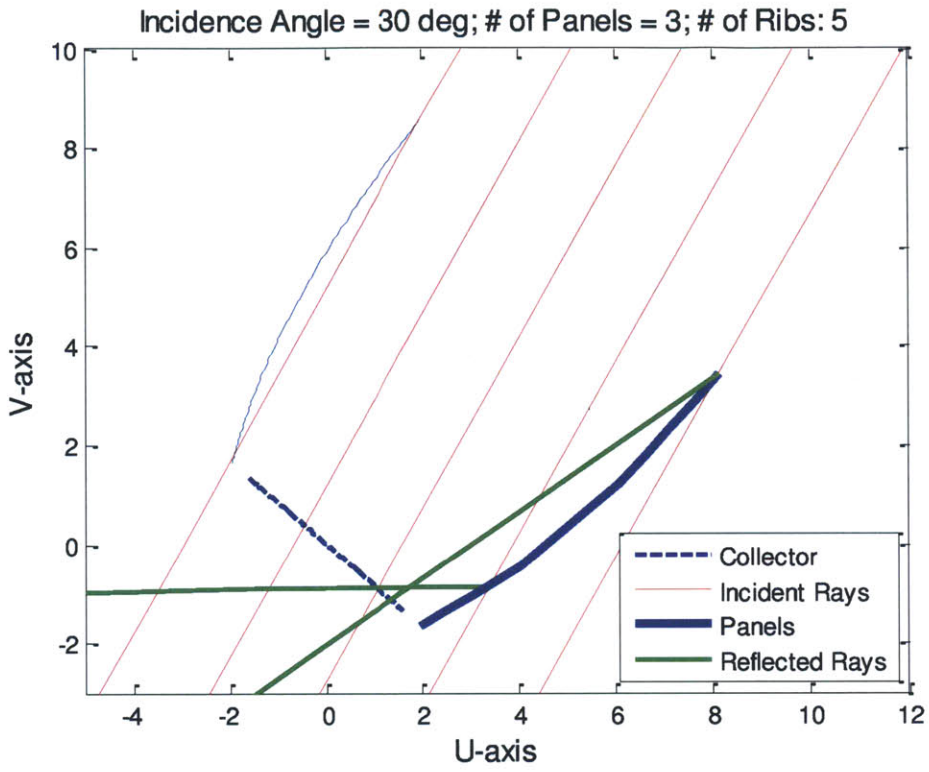


**Figure 4-7: First-order ray tracing analysis for varying number of ribs; incidence angle of 30° entering concentrator profile containing three reflective panels along walls and five ribs.**

Figure 4-7 shows the ray tracing model of five rays with incidence angle of 30° entering a concentrator with acceptance half-angle of 40° and five ribs when it has three reflective panels along its height. Again, the results were plotted in a three-dimensional surface graph for both scenarios: fixed number of panels (see Figure 4-8) and a fixed incidence angle (see Figure 4-9).

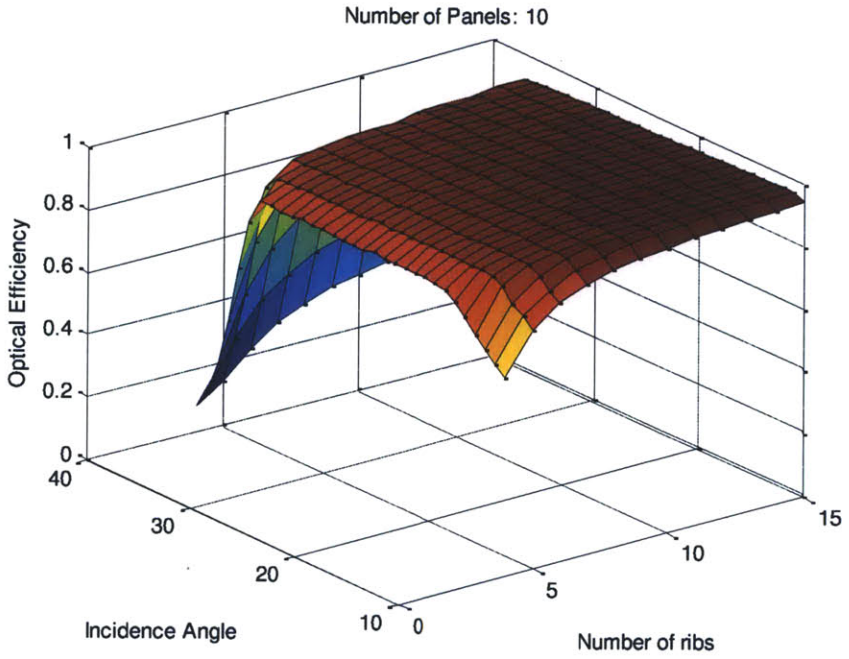


**Figure 4-8: First-order ray tracing model results – optical efficiency as a function of number incidence angle and number of ribs for a fixed number of panels. (Acceptance half-angle: 40°)**

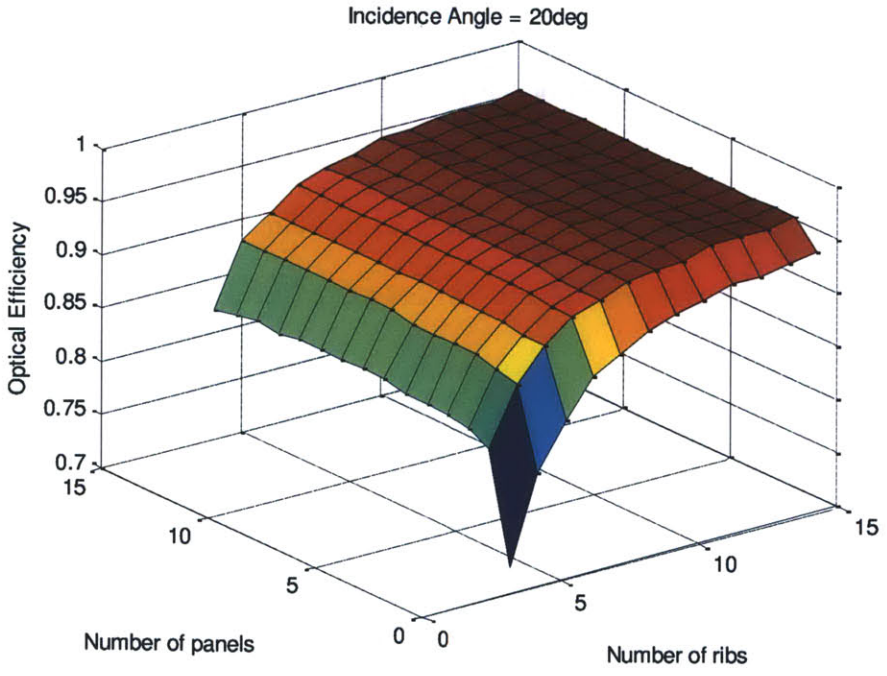


**Figure 4-9: First-order ray tracing model results – optical efficiency as a function of number of panels and number of ribs for a constant incidence angle. (Acceptance half-angle: 40 °)**

As seen in Figure 4-8, similar to what was observed in Figure 4-4, increasing the number of ribs has diminishing returns in optical efficiency for a specific range of incidence angle; the effect becomes more noticeable at the extremes, close to 0° and close to the acceptance half-angle. Figure 4-9 reveals that for a fixed incidence angle, the number of ribs is the most influential factor on the optical efficiency. It can be assumed that this relationship varies depending on the incidence angle; but given the right conditions, the design of a CPC could be simplified dramatically. In conclusion, it was also determined that the maximum efficiency of the system with the theoretical CPC geometry can be closely approximated by a small number of ribs.

## 4.3 Ray Tracing: Multiple Reflections

During the testing phase (Chapter 6), a more accurate analytical model was built, which considered multiple reflection, including the other reflective branch of the concentrator profile. The same procedure was done to determine the equations of the straight segments along the other branch. However, since the second branch is aligned on another coordinate system, all the points and equations had to be transformed to the same U-V coordinate system that was being used. In addition, an extra loop was added to the code which considered rays that required multiple reflections to reach the receiver. The new model provided more accurate values of efficiency for specific design parameters, but it the same trends were observed.

# Chapter 5: Design and Manufacturing

## 6.1 Strategy

The main objective of designing and building prototypes was to test the accuracy of the analytical model. In addition, building prototypes leads to better understanding of real performance of the system and helps improve the design for manufacturing and assembly process. While the goal was the build an inflatable solar concentrator, the approach was to use rapid-prototyping techniques to assemble a small-scale prototype while discussing the inflatable design with Otherlab.

The critical design parameters were specified and calculated in the Matlab analytical model. In the code, the user specifies the aperture length and acceptance half-angle which are used to calculate the height and exit lengths of the concentrator. For the analytical model, the code iterates through multiple number of reflective panels in each facet and different number of ribs. As the parabolic branch is divided into $n$ equal segments for calculating the equations of the linear segments, the coordinates of the interval endpoints are stored.

The prototype design was done in SolidWorks, using design tables to manage the dimensions of the part sketches from the Matlab script. The main part sketches were setup as follows:

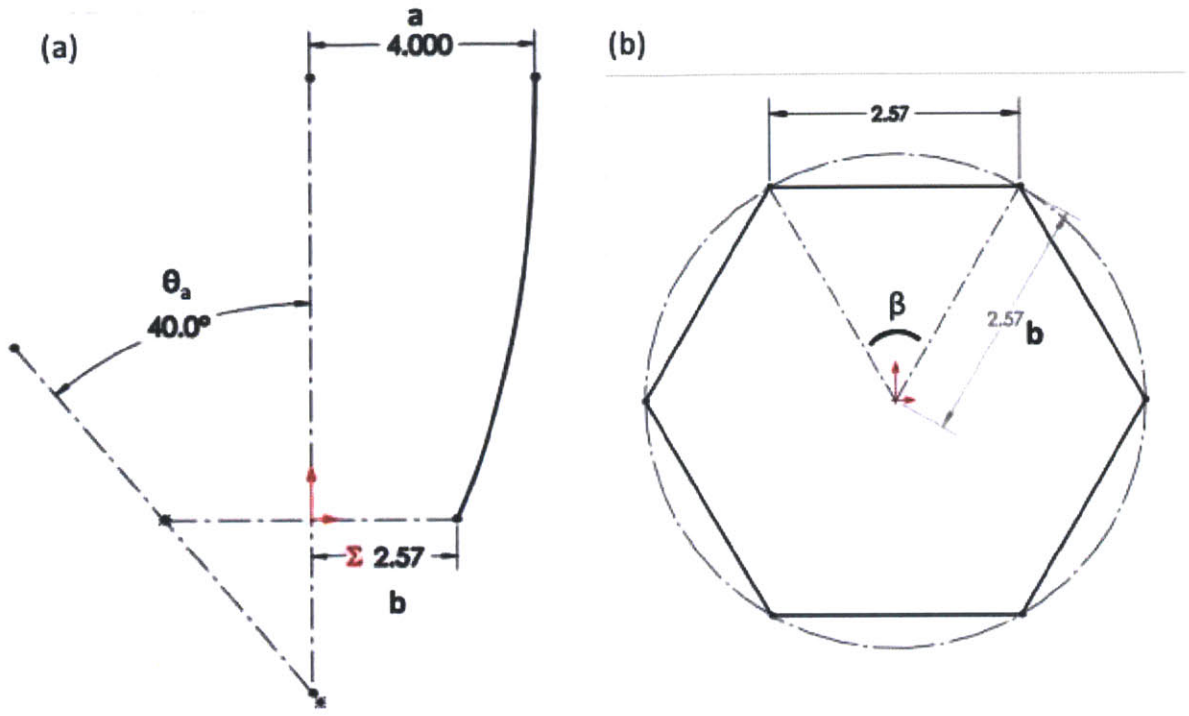


**Figure 5-1: SolidWorks sketches representing main baseline geometry for (a) inflatable ribs and (b) the concentrator's aperture and exit.**

Figure 5-1a depicts a side cross-sectional view of the CPC, where the parabolic branch is the baseline for the inflatable ribs. The image shows the main dimensions needed to fully define the sketch: the aperture radius, $a$, and the acceptance half-angle, $\theta_a$, which are related to the exit radius, $b$, via Equation 2-10 (the dimensions $a$ and $b$ are referred to as 'radius' because they correspond to the radius of the polygons at the concentrator's aperture and exit, respectively). All three dimensions are parameters in the Matlab ray tracing code; thus, when the code is run, the dimensions are automatically updated in the design table that controls the sketch. Figure 5-1b shows the top cross-sectional view of the CPC at the plane of the concentrator's exit. As noted, the radius of the polygon is the distance, $b$. The length of the polygon's sides represents the length of the reflective panels in the facet at that particular plane. In general, the dimensions of a polygon's radius and sides are related by

$$s_{polygon} = 2\, r_{polygon}\, \sin\left(\frac{\beta}{2}\right), \qquad \textbf{Equation 5-1}$$

where $s_{polygon}$ is the side of the polygon, $r_{polygon}$ is the radius of the polygon, and $\beta$ is the central angle. In this example, since the polygon is a regular hexagon, the trigonometry works out such that the dimension of each of the polygon's sides is equal to the exit radius.

As previously described, the reflective region in the concentrator was going to be built using reflective panels that meet at the ribs, forming reflective facets. The key to dimensioning these panels was in the endpoints of the intervals in the parabolic branch, which indicate where the panels meet. Since the equation of the parabolic branch was expressed in the rotated coordinate system, the coordinates of the panel endpoints were also calculated in the U-V coordinate system:

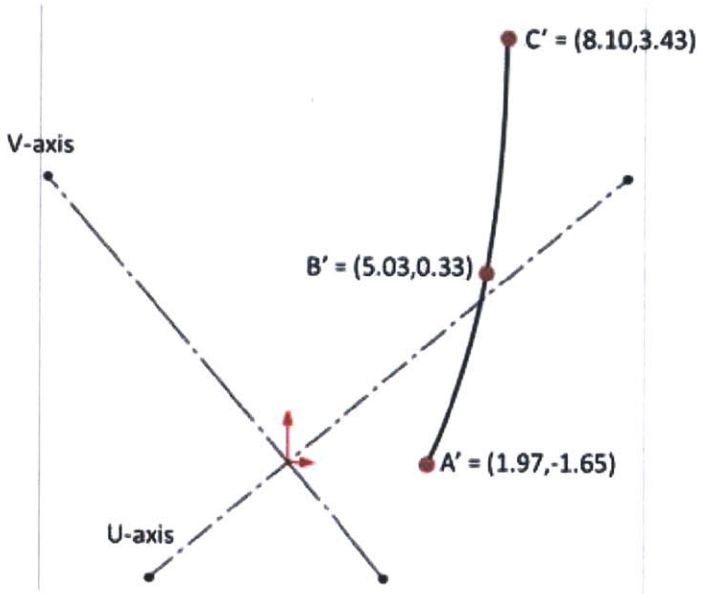


**Figure 5-2: Parabolic branch divided into two equal intervals. *A'*, *B'*, and *C'* are the endpoints of the reflective panels; their coordinates are expressed relative to the U-V coordinate system.**

Figure 5-2 shows the endpoints of two intervals in the parabolic branch expressed in the U-V rotated coordinate system. This scenario describes a facet that would use two reflective panels to approximate the theoretical parabolic branch. In order to use these coordinates to dimension the panels, they were transformed back to the X-Y coordinate system:

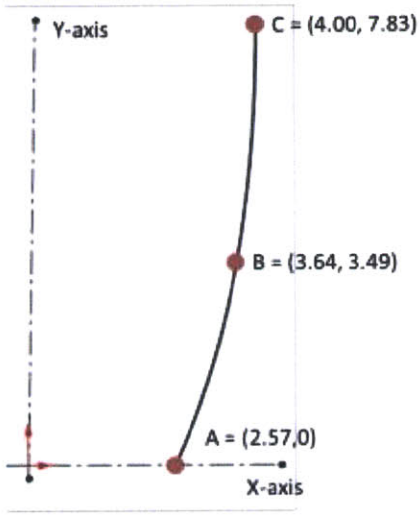


**Figure 5-3: Reflective panels' endpoints expressed in the X-Y coordinate system: *A*, *B*, and *C***

Figure 5-3 is a side view of the panels, as seen from the ribs, showing the same endpoints as in Figure 5-2, but expressed in the X-Y coordinate system. Figure 5-4 helps visualize the geometrical relationship between the x-y coordinates of the endpoints and the dimensions of the panels in each facet.

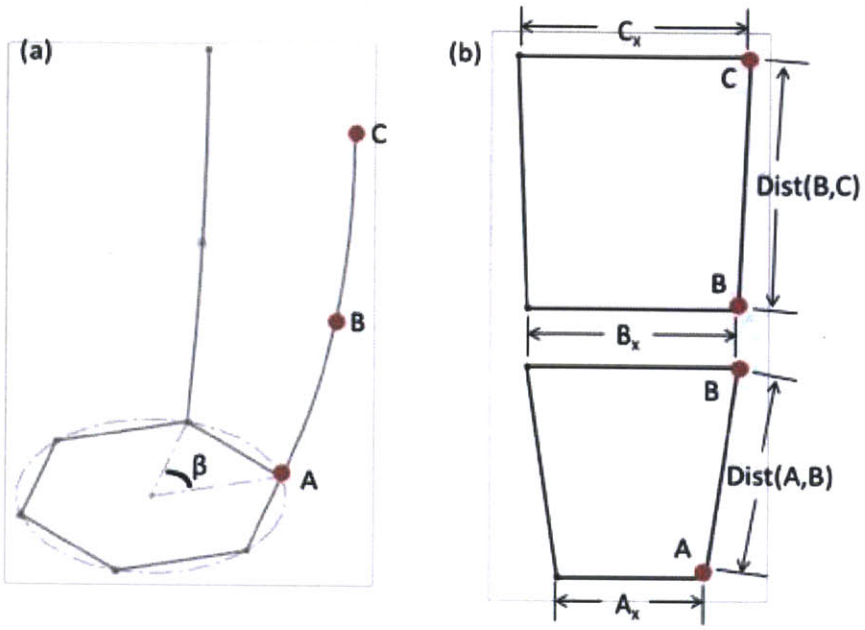


**Figure 5-4: Sketches describing the relationship between (a) the segment endpoints in the parabolic branch (ribs) and (b) the dimensions used to define the panels for the reflective facets.**

Figure 5-4a is a three-dimensional sketch showing the position of the ribs (Figure 5-3) in the overall geometry of the concentrator. This particular sketch describes a concentrator that uses two reflective panels in each facet (space between the ribs), and uses a total of six ribs, hence the hexagonal cross-sectional shape. The origin in Figure 5-3 is at the center of the hexagon in Figure 5-4a, having the Y-axis coincident with the concentrator axis and the X-axis along the dotted line that connects the center of the hexagon with point *A*. Additionally, it can be seen that each panel will assume the shape of an isosceles trapezoid. In Figure 5-4b, schematics of the two reflective panels that would be used in the proposed concentrator design are shown. In addition, it demonstrates how the coordinates of points *A*, *B* and *C* are correlated to the dimensions of the panels.

From the perspective of the concentrator's aperture, its cross-section is a regular polygon that reduces in size as it approaches the exit. At any plane along the height of the concentrator,

the length of the polygon's side, corresponding to the base of the panels at that plane, will be determined by its radius and central angle (Equation 5-1). In Figure 5-4, points *A*, *B*, and *C* are the coordinates for the corners of a polygon at different vertical distances, equal to the y-coordinate of each respective point, from the bottom of the concentrator. For each point, the x-coordinate corresponds to the radius of the polygon which can be used to determine the base length of the reflective panels at each plane. For this particular case, in which the polygon is a regular hexagon, the base length of the reflective panels at the y-coordinate of each one of the points *A*, *B* and *C*, is equal the x-coordinate $A_x$, $B_x$, and $C_x$, respectively.

To determine the third panel dimension that fully constrains the design, the same coordinates were used. From analyzing Figure 5-3 and Figure 5-4, it can be seen that the distances between points *A* and *B*, and points *B* and *C*, in the plane of the rib describe the side contours of the panels throughout the height of the concentrator. Hence, the length of the leg of a particular panel equals the distance between the coordinates corresponding to the top and bottom vertices. In this example, the leg of the bottom panel equals the distance between points *A* and *B*, while the leg of the upper panel equals the distance between points *B* and *C*.

## 5.2 Small-scale prototype

### 5.2.1 Prototype 1

After the first-order analytical model was completed, the results were used to design a sketch-model of the concentrator concept. Knowing that it is possible to obtain a reasonable optical efficiency with a low number of ribs and reflective panels in each facet, it was decided to build a prototype with six ribs and six panels. The other dimensions of the concentrator were

chosen such that the prototype would have a small, manageable size; aperture radius of 4.00 inches and 40° accepted half-angle, as depicted back in Figure 5-1. To manufacture the prototype quickly, all components were designed such that they could be made using the waterjet. The design of the ribs was done using the sketch of Figure 5-1a as a baseline and adding features to assemble it around a disc. A CAD of the rib is shown below.

**Figure 5-5: Parabolic rib for Prototype 1**

As discussed, the ribs were designed such that they would be pressure fitted into slots around the circumference of a disk, as shown in Figure 5-6. Both the ribs and the disk were made out of high-density polyethylene (HDPE), 0.25 inch thick and 0.50 inch thick, respectively.

**Figure 5-6: CAD image of Prototype 1.**

Next was the design of the reflective panels. For the purpose of testing the models, it was decided to use sheet metal in order to guarantee the panels would remain as flat as possible to better test the accuracy of the analytical model. The sketch for each panel was an isosceles trapezoid defined by the lengths of both bases and the leg. All three dimensions were controlled by a design table linked to the rib's CAD file, which was updated automatically by the Matlab

ray tracing code with the coordinates of all the interval endpoints. Once set up correctly, dimensions of all panels would be updated directly by managing the main design table in the rib CAD file. Below is a CAD assembly of all the panel components ready to be converted to an .ord file for the waterjet.

**Figure 5-7: Prototype 1 facet composed of six reflective panels**

Once all components were manufactured, they were assembled by press fitting the ribs into the slots in the disk and using double sided tape to attach the panels to the ribs (see Figure 5-8).

**Figure 5-8: Partial assembly of Prototype 1.**

Inserting the ribs in the base disk was a trivial operation. However, aligning the panels along the facet proved to be a complicated task for three main reasons: (1) the profile of the panels was constructed by drawing a line between two points in the parabolic curve, meaning that the panels only make contact with the ribs at two points, (2) there were no features included in the design which helped the alignment of the panels respect to each other along the height of the concentrator, and (3) the ribs came out to be too flexible. After assembling the first facet between two ribs, those ribs were pulled in together widening the gap in the adjacent facet regions (see Figure 5-9)

**Figure 5-9: Misalignment of reflective panels in Prototype 1.**

Figure 5-9 fully captures the problems encountered during the assembly of Prototype 1. At the bottom portion of the concentrator, the two facets seem to be interfacing smoothly. However, it is clear how this deteriorates as you go up the concentrator. It can be seen how the edges of the panels in each facet do not form a smooth contour, making it difficult to assemble adjacent facets. All these issues were taken into account and corrected for a second version of a small-scale prototype.

### 5.2.2 Prototype 2

For the second small-scale prototype, the rib was designed to facilitate the panel alignment during assembly. Two rib designs that were considered are shown below in Figure 5-10.

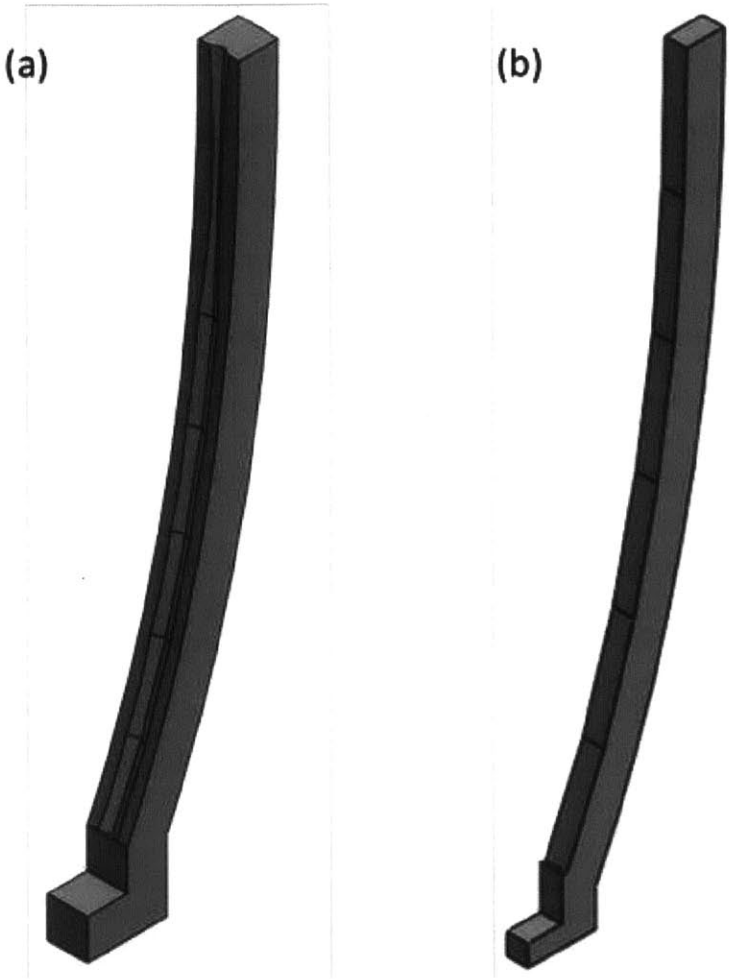


**Figure 5-10: Rib designs considered for Prototype 2 to be assembled in different locations - (a) rib for polygon corner location; (b) rib to be on polygon side directly supporting back of panels.**

Figure 5-10a shows a re-design of the rib used in Prototype 1; it's meant to be kept at corners of the polygon indicating the edges of the facets. The part was designed such that a V-groove router bit could be used to cut out a 90° section along the profile of the panels. This would provide the ribs with a feature that helps align the panels in the correct orientation at the facet interface in each corner. Figure 5-10b is based on a different approach that deviates slightly from the inflatable design concept. This approach cut out the profile of the flat panels on the side

of the ribs, to be placed directly behind the facets such that the panels would have a surface to rest on. This meant that the location of the ribs would have to change from the corners of the polygon to directly on the polygon's sides and a second rib would be used for each facet to provide better support. This location of the ribs together with the new surface profile provides a good surface to guide the placement of the panels along the ribs. The concept in Figure 5-10a provides a better alignment feature to guarantee panels are placed in the right position along the facet, however it is more complex to manufacture than the design shown in Figure 5-10b which would also be done in the waterjet. Again, driven by the need for a rapid-prototyping strategy, the latter approach was selected.

The new prototype design concept necessitated the redesign of the base of the concentrator. For Prototype 2, the base was designed such that ribs could rest directly behind the facets and the desired geometry of the concentrator exit was open to allow for testing (see Figure 5-11).

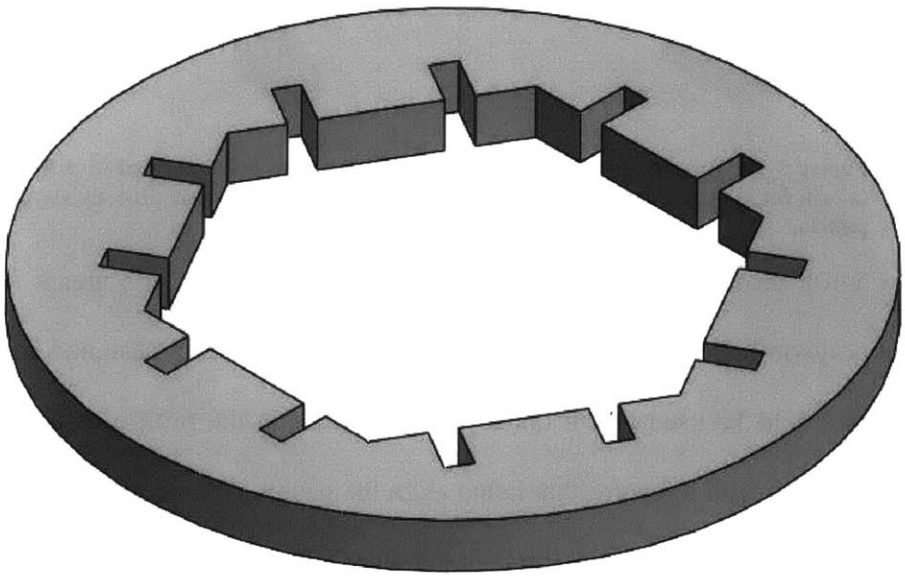

**Figure 5-11: Base of concentrator for Prototype 2.**

Furthermore, the interface in the ribs was altered such that it would mate with the collector through the side opposite to the facets, thus not interfering with the concentrator exit. Below is a full CAD of the assembly of Prototype 2:

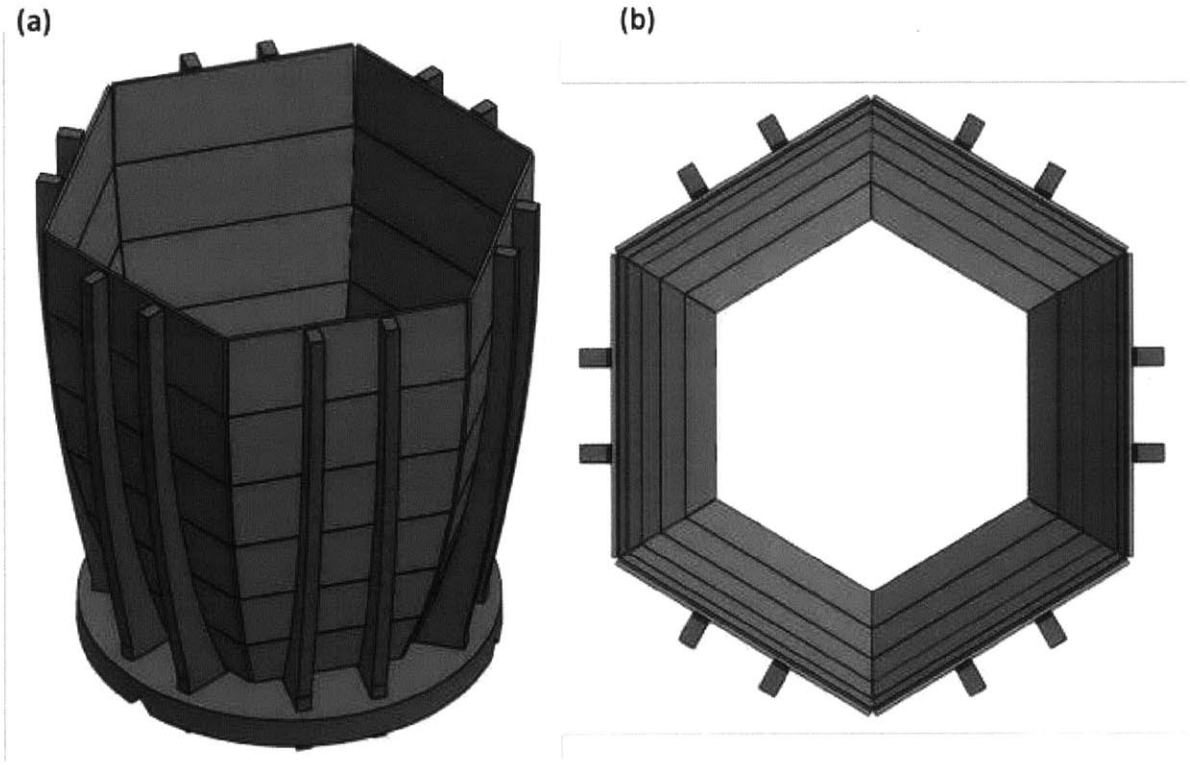


**Figure 5-12: CAD model of Prototype 2 - (a) Isometric view; (b) Top view.**

The sole necessary change related to the reflective panels was involving the assembly process. As discussed, it was a difficult task to align all the panels properly along the facets which jeopardized the adjacent facet interfaces. After a series of bench-level experiments, a solution was developed to robustly assemble the facets and mount them on the concentrator. Panels still had to be made independently because each one rests on the ribs at different angles. Thus, to manage all the panels as one piece, they were taped together. Since the facets are made of independent panels, the junction of adjacent panels creates a hinge and allows for the

assembly to be placed on the ribs properly. ReflecTech® mirror film was used to tape the panels together because it is designed to be both adhesive and reflective.

The execution of this improved assembly process consisted of a series of steps. A facet template was designed and made out of sheet metal thinner than the one used for the panels using the waterjet. After the template was fixed on a flat surface, the panel sections could be placed in the template for precise alignment (see Figure 5-13).

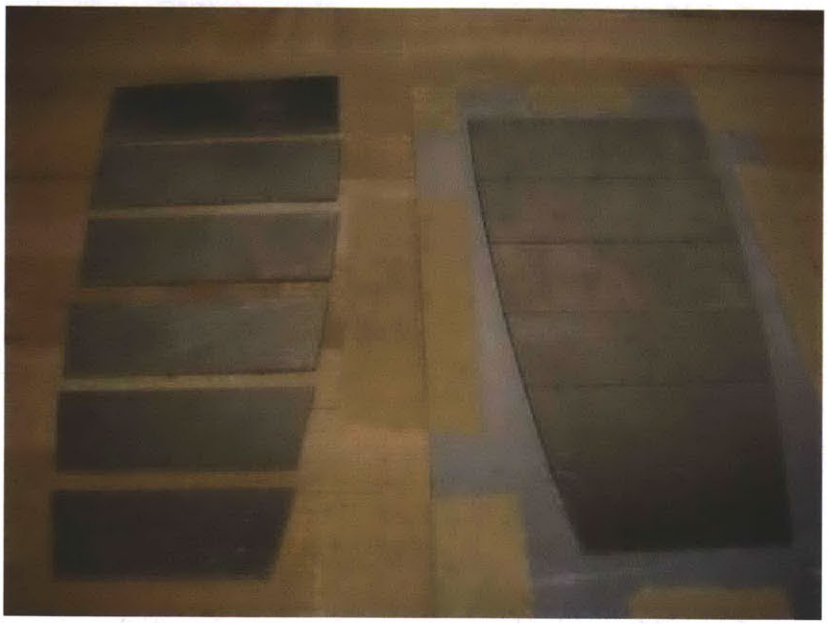

**Figure 5-13: Independent panels before and after being placed in the facet template.**

Once aligned, the ReflecTech® mirror film was carefully applied on the panels resting in the template using a roller (see Figure 5-14); the film had to be applied very carefully in order to minimize the number of bubbles on the surface since they would negatively affect the optical efficiency of the mirror. ReflecTech® has protective transparent films on both sides; one side protects the adhesive and the other the reflective surface. During this step, only the protective

film on the adhesive side was removed in order to tape it on the panels. The film on the reflective side was left on to protect it during the assembly process; it would later be removed for testing.

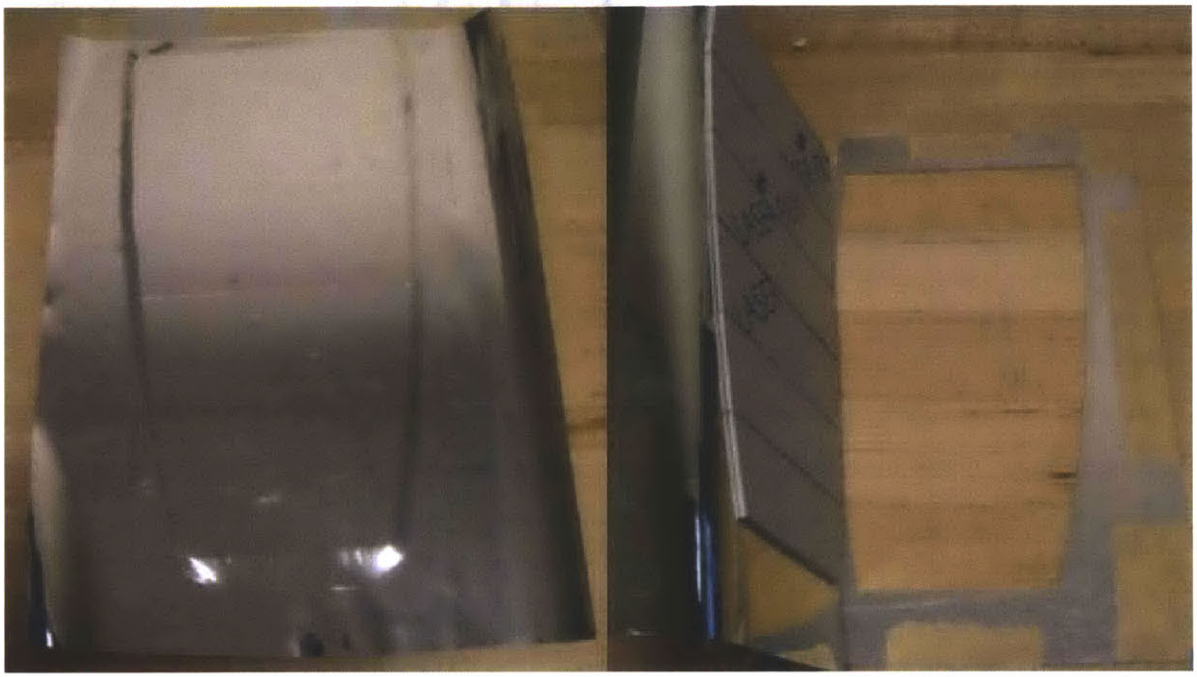

**Figure 5-14: Application of ReflecTech® mirror film on the panels to make facet assembly.**

Then, the facet assembly was removed from the template and an X-Acto knife was used to remove the excess mirror film. The full assembly process of the facet is shown in Figure 5-15.

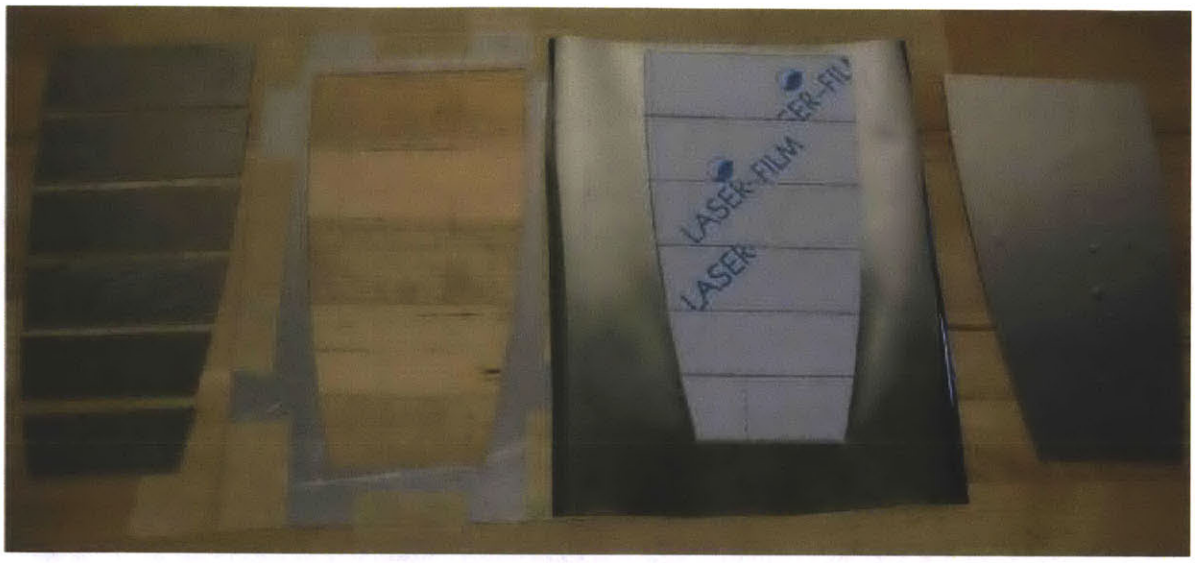


**Figure 5-15: Full assembly process of reflective facets.**

The right-most image in Figure 5-15 shows some of the bubbles that can form during the ReflecTech® application.

Similar to the first prototype, the facets of the second prototype were also attached using double-sided tape. The ribs were press-fitted into the slots in the concentrator base and strips of double-sided tape were attached to the flat sections of the rib profiles, as shown in Figure 5-16.

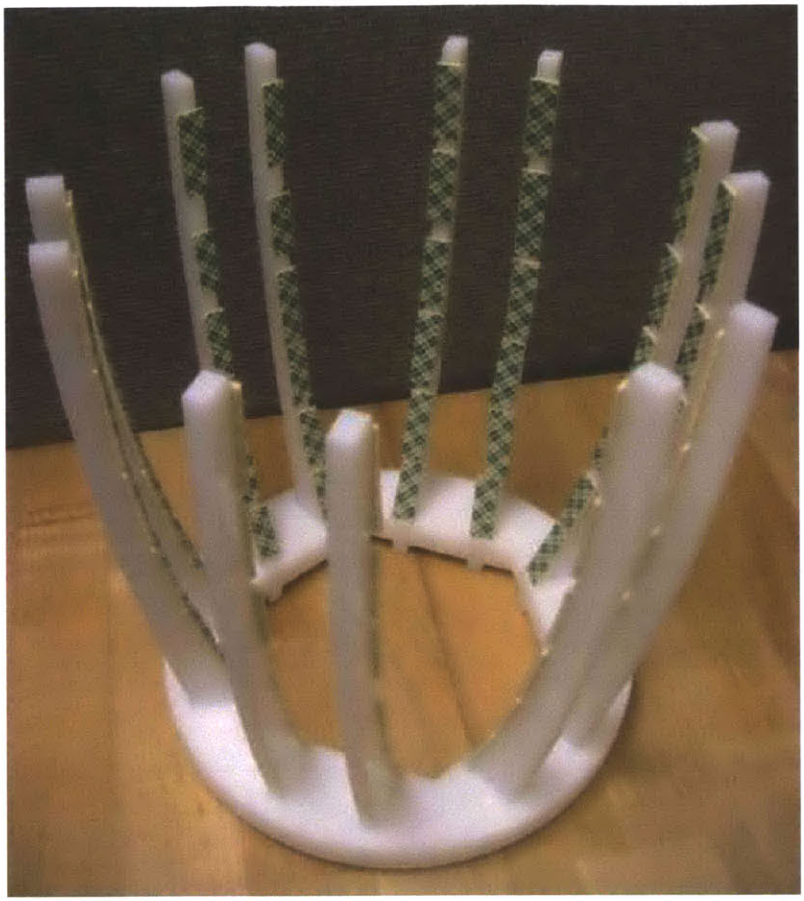

**Figure 5-16: Partial assembly of Prototype 2; double-sided tape on ribs, ready for attachment of facets.**

Once all of the facets were assembled using the method previously described, they were mounted on the ribs. For proper alignment, the bottom edge of each facet was aligned with the side of the hexagon at the base of the concentrator. After correct placement, the rest of the panels were pressed down on the tape. Below is an image of the finalized assembly.

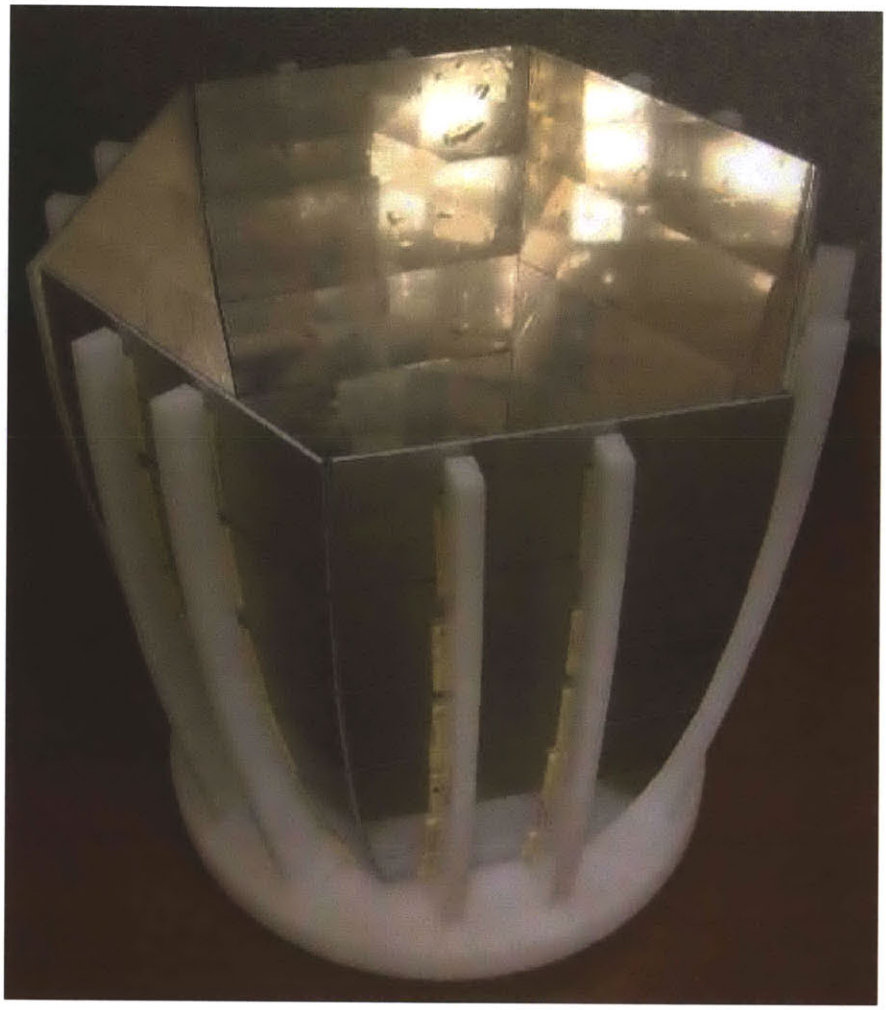

**Figure 5-17: Prototype 2 fully assembled.**

## 5.3Inflatable

### 5.3.1 Sizing

The inflatable solar concentrator was designed at full-scale. The concentrator dimensions were specified such that it could be used to cook rice, a common meal in developing countries. In order to cook rice, the concentrator must be able to direct the amount of energy required to boil water and cook 1 kg of rice, about four cups, to a receiver. According to [15], it takes approximately 800 kJ of energy to cook rice, assuming 1.5 kg of water per 1 kg of rice. To bring this 1.5 kg of water to a boil (100 °C), additional energy is required. This can be calculated by

$$E_b = m_w \, c_{p,w} \, \Delta T, \tag{8}$$

where $m_w$ is the water quantity (1.5 kg), $c_{p,w}$ is the specific heat of water (4.16 J/kg-C°), $\Delta T$ is the change in temperature (100 °C– 20 °C), and $E_b$ is the energy, in Joules. In this case, 502.3 kJ of energy are needed to bring 1.5 kg of water to a boiling in order to cook the rice. Hence, the concentrator must be able to collect 1.3 MJ of energy to cook 1 kg of rice. Furthermore, it was assumed that the user will want to cook the rice in a reasonable amount of time.

For the purpose of this calculation, a conservative estimate for the amount of time it would take to boil water and cook 1 kg of rice was one hour. Recall from Equation 2-1 that the intensity of the sun at a surface depends on the incidence angle. Thus, since the sun's position will be changing at a certain rate, the total energy collected must be integrated over the entire charging period. For the purpose of these calculations, the angular change of the sun was assumed to be

$$\frac{d\gamma}{dt} = \frac{180°}{12\,hrs} = 7.27\,x\,10^{-5}\,\frac{rad}{s}, \qquad \text{Equation 5-2}$$

where $\frac{d\gamma}{dt}$ is the angular displacement per second of the sun. Furthermore, the amount of energy entering the concentrator's aperture can be calculated by

$$E_{aperture} = \int_{t_1}^{t_2} A_{aperture}\, I_0\, \cos\gamma\, dt. \qquad \text{Equation 5-3}$$

In Equation 5-3, $E_{aperture}$ is the total energy entering the concentrator's aperture during the time period between $t_1$ and $t_2$, $A_{aperture}$ is the area of the aperture, and $\gamma$ is the sun's incidence angle at a particular step of integration. Since $\gamma$ also has a time dependency, Equation 5-2 and Equation 5-3 were combined in order to calculate the available energy with respect to the incidence angle at $t_1$ and $t_2$, as described by

$$E_{aperture} = \int_{\gamma_1}^{\gamma_2} A_{aperture}\, I_0\, \cos\gamma\, \frac{d\gamma}{7.27\,x\,10^{-5}\,\frac{rad}{s}}, \qquad \text{Equation 5-4}$$

where $\gamma_1$ and $\gamma_2$ are the initial and final positions of the sun, respectively, with respect to the aperture's normal. When determining the incidence angle of the sun at the beginning and end of the collection period, it was assumed that the concentrator will be placed in such a position that maximizes available energy; this means that at the midpoint of the considered period, the acceptance angle is 0°. For example, with the angular rate described by Equation 5-2, it was determined that the sun sweeps a total of 15° during the one hour period being considered for cooking the rice. The concentrator is assumed to be positioned such that $\gamma_1 = -7.5°$ and $\gamma_2 = +7.5°$. A script was written on Matlab to solve for the aperture area necessary to collect the requisite energy in a specific amount of time, considering the theoretical optical efficiency of the concentrator. Taking into account possible inconsistencies in the energy requirement estimates,

the required energy used was 1.5 MJ. Based on the calculations, it was determined that the radius of concentrator aperture had to be 42.06 cm, or 16.56 inches, in order to collect 1.5 MJ of energy in one hour.

The other parameter that had to be determined in order to design the inflatable solar concentrator was the acceptance half-angle. For the application previously discussed, an acceptance half-angle of 7.5° would suffice. However, if the user was interested in a longer energy collection period, there are other factors that must be considered. Recall that as the acceptance half-angle of the CPC increases, both the concentrator's height and concentration ration will decrease. Thus, there must be a compromise between the size of the concentrator and the number of tilts it requires for energy collection during a period of time. Using the same angular displacement rate of the sun from Equation 5-2, the number of times a concentrator would have to be repositioned, or tilted, in order to collect energy for a full 10 hour period in a day was analyzed. In this period, the sun would sweep an angular distance of 120°, depending on a particular acceptance half-angle (see Table 2). Based on this study, it was decided that designing a concentrator with an acceptance half-angle of 25° was an acceptable compromise between a good concentration ratio and a reasonable number of times the concentrator would have to be repositioned in a 10 hour period. Table 3 shows a summary of the design parameters describing the inflatable solar concentrator. The areas of the concentrator aperture and exit were calculated using the equation for the area of a regular hexagon, expressed in term of its radius.

**Table 2: Number of tilts required to collect all the energy available in a 10 hour period for a given concentrator acceptance half-angle.**

| $\theta_a$ [°] | $2\theta_a$ [°] | Number of Tilts |
|---|---|---|
| 7.5 | 15 | 8 |
| 10 | 20 | 6 |
| 15 | 30 | 4 |
| 20 | 40 | 3 |
| 25 | 50 | 3 |
| 30 | 60 | 2 |
| 35 | 70 | 2 |
| 40 | 80 | 2 |

**Table 3: Design parameters of the full-scale inflatable solar concentrator.**

| Aperture | | Exit | | Acceptance Half-Angle [°] | Height [in.] | Concentration Ratio |
|---|---|---|---|---|---|---|
| Radius [in.] | Area [in.] | Radius [in.] | Area [in.] | 25 | 50.52 | 5.60 |
| 16.56 | 712.48 | 7.00 | 127.31 | | | |

### 5.3.2 Full-Scale Prototype: Inflatable

The inflatable solar concentrator was envisioned as a structure consisting of inflatable ribs, forming an outer frame, with reflective facets connected to them. Designing to minimize weight and maximize portability, the solar concentrator should have a light, reflective film (e.g. Mylar) forming the facets instead of sheet metal, as was done for the small-scale prototypes. Not only would this minimize the weight of the system, but it also facilitates easy assembly, without the need of adding or removing parts (i.e. detachable reflective panels). However, for

prototyping purposes, the reflective facets were assembled using ReflecTech® covered sheet panels to ensure that the reflective surfaces were truly flat, similar to what was described in the analytical model.

The design of the inflatable part of the solar concentrator was done with direct feedback from Otherlab engineers, particularly Kevin Simon, Pete Lynn, and Tucker Gilman, given their expertise in the design and manufacturing of complex inflatable systems. The concept was to have Otherlab manufacture the inflatable ribs; the reflective panels would be made separately, using a similar approach as the one used for the small-scale prototypes. For the inflatable design, the same rib profile shown in Figure 5-1a was used, but with the dimensions listed in Table 3. To convert the CPC profile into inflatable tubes, the curve was offset by half the diameter of the inflatable tubes such that the surface for the reflective panels would remain at the intended location. Solidwork's sweep feature was used to create an inflatable rib; the feature was revolved around the concentrator axis to get the rest of the ribs. For rigidity, hexagonal inflatables were added at the aperture and exit of the concentrator. Figure 5-18 shows the CAD model of the first inflatable CPC design that was sent to Otherlab for revision.

**Figure 5-18: Inflatable CPC design, version 1.**

The most crucial feedback from Otherlab was: although the hexagons were easy to make, the long parabolic tubes could not be developed as designed. The two options were to approximate the curve with short, straight sections along the length, or to split the curve long ways along the saddle and sew length-wise. Since the parabolic branches were already being approximated by straight sections, incorporating this into the design was the obvious next step. Instead of using the theoretical parabolic branch of the CPC as the path in the sweep feature, a profile was made using line segments to connect the endpoints obtained from the Matlab code. In addition, the interface of the ribs with the lower hexagonal inflatable was modified such that the hexagon wouldn't block any portion of the specified concentrator exit. The two-dimensional

sketches of the new sweep path, as well as a close-up of the concentrator exit region, are shown in Figure 5-19.

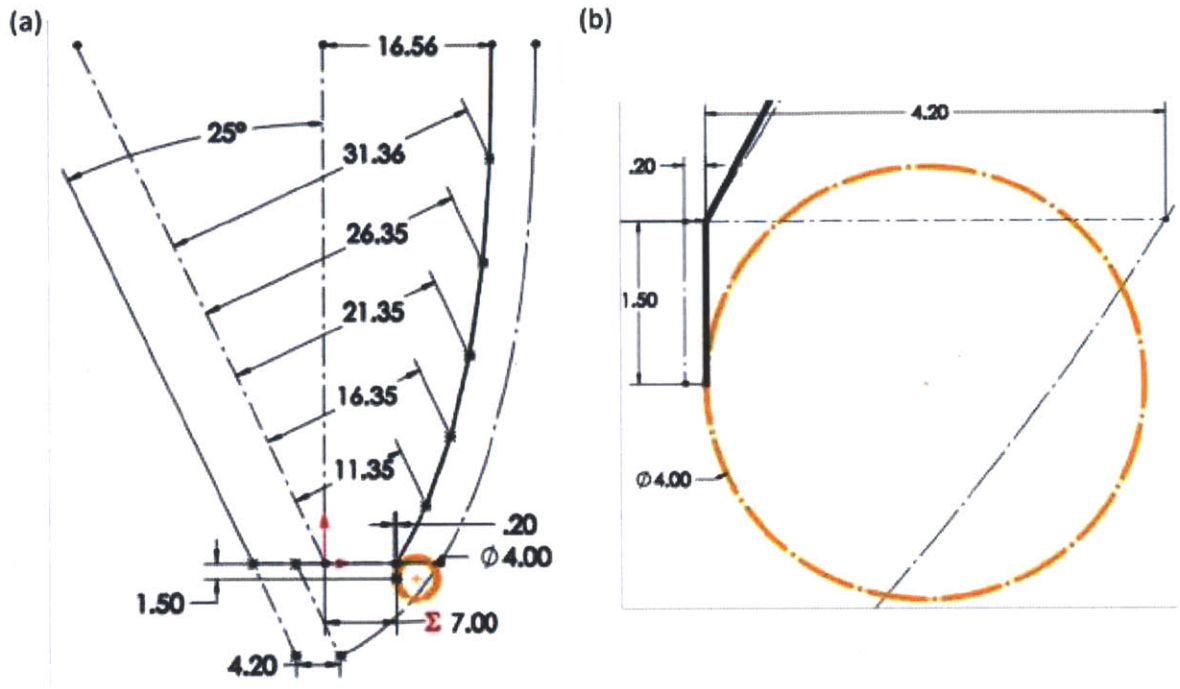


**Figure 5-19: Two-dimensional sketch of sweep path used to design inflatable ribs (Units in inches, unless otherwise specified.) – (a) fully constrained sketch showing design dimensions; (b) close up of interface between rib and lower hexagon.**

In Figure 5-19a, the main design dimensions can be seen: aperture radius (16.56 in.), aperture exit (7.00 in.), acceptance half-angle (25°) and the horizontal distance of each endpoint from the axis of the right branch of the CPC along the U-axis. The remaining dimensions represent specific changes made so that the concentrator met specifications, more clearly seen in a close-up of the interface between the rib and lower hexagon shown in Figure 5-19b. The thick black line represents the edge of the inflatable rib, which has been shifted outward by 0.20 in. to account the thickness of the reflective panels, the ReflecTech® mirror film, and the attachment medium (Velcro). The vertical segment, 1.50 in. long, connects the lower-most endpoint of the

CPC profile with the orange circle (4.00 in. in diameter), guaranteeing that the lower inflatable does not block any light that exits the concentrator.

It was easier for Otherlab to design and fabricate the bottom attachment points (Figure 5-19b) if the bottom tubes (orange circle) and ribs were the same diameter, and if their center lines intersect. They recommended a design that allows for simpler fabrication results and a more precisely constructed structure. Only the first suggestion was adopted because of necessity for the attachment method sketched in Figure 5-19b – designing the bottom tubes and ribs such that their center lines intersect would mean that a fraction of the light exiting the concentrator would go into the bottom inflatable rather than to a collector.

Another suggestion made by Otherlab was that the intersection between ribs and the hexagons be modified because it is challenging to construct the junctions where three tube segments meet. The proposed solution was to re-draw the joints where the parabolic units meet the top and bottom such that there is a straight segment on each side of the last tube in the parabolic unit for sewing it all together; this turned the hexagons into dodecagons (see Figure 5-20). Since the shape of aperture and exit were truly defined by the reflective facets, this suggestion was incorporated into the design in order to facilitate Otherlab's fabrication process.

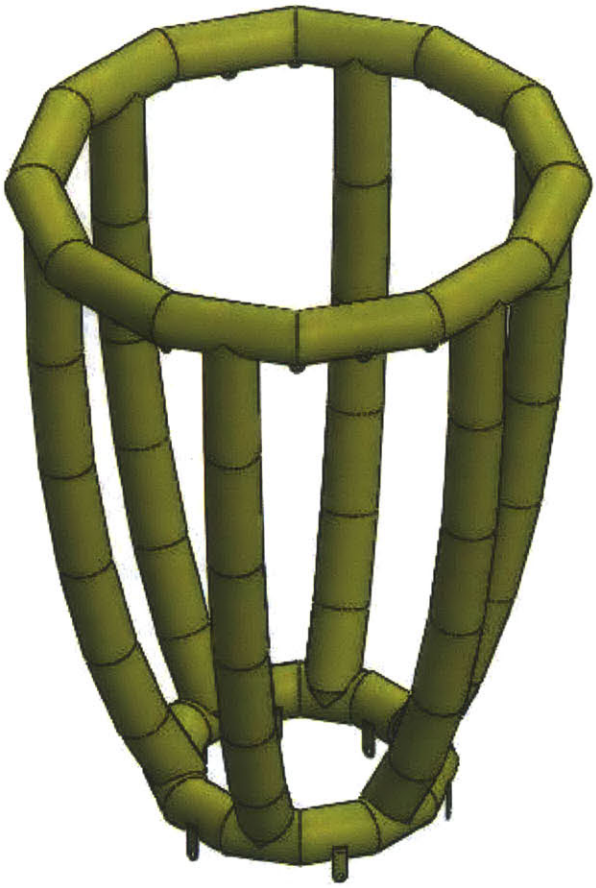

**Figure 5-20: Final CAD model of inflatable solar concentrator that was sent to Otherlab for fabric design and fabrication.**

As seen in the final CAD model of the inflatable concentrator in Figure 5-20, small tabs were added to the top and bottom inflatable structure, per Otherlab's recommendation. The bottom inflatable piece has two tabs in the inside and outside of alternating segments to be used as possible attachment points for fixing the concentrator at a particular location. The tabs on the upper dodecagon were sewn on to be used in case Mylar was used to make the facets. The tabs could be used to tie the upper ring of Mylar and tension into a more circular shape to help smooth out the surface and improve optical efficiency.

The final CAD file of the inflatable solar concentrator was sent to Otherlab for fabrication. Using the three-dimensional model, they were able to determine in which shape to cut out the fabrics and sew them together to produce the desired structure. A picture of the finalized concentrator is shown below in Figure 5-21.

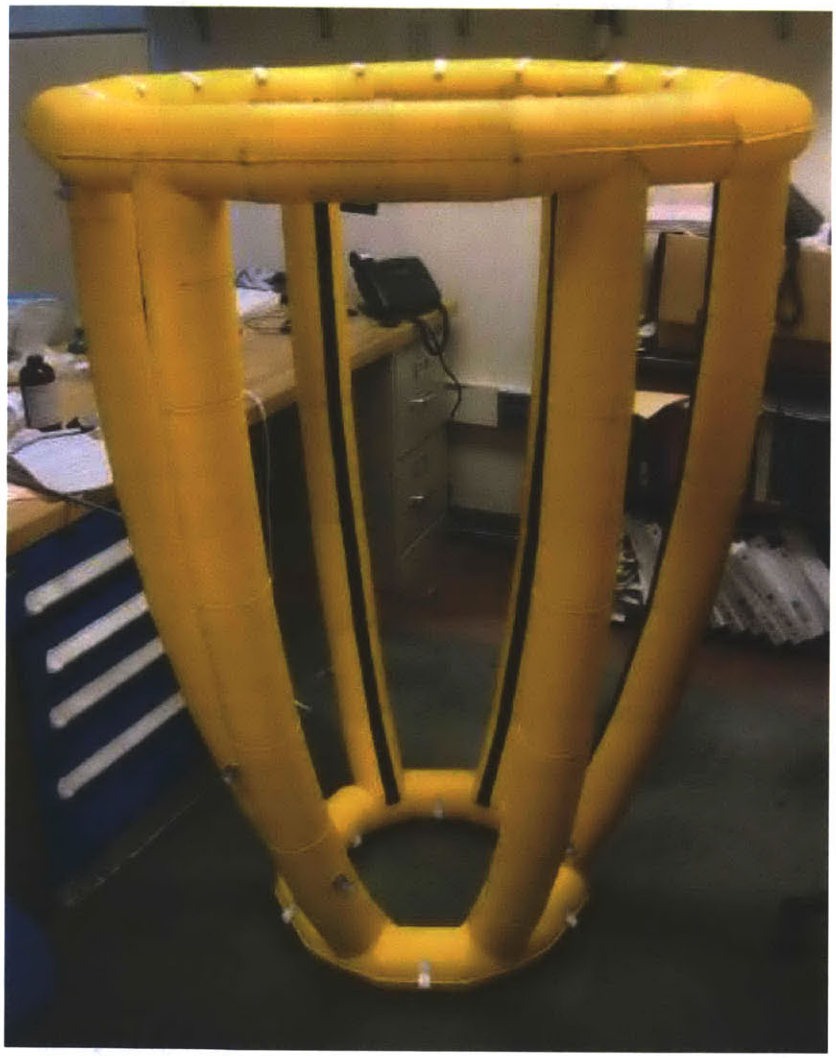

**Figure 5-21: Finalized inflatable frame for the solar concentrator.**

The outer shell of the inflatable is made out of PVC covered nylon and the inside bladders are made out of polyurethane. Each inflatable section of the structure is independent from all the others, which has benefits and drawbacks. The advantage of discrete sections is that if one bladder were to fail, the rest of the structure would remain intact. However, the independent sections complicate the inflating process.

### 5.3.3 Full-Scale Prototype: Reflective Facets

A small modification was made on the flat panel design. Since the precision of the inflatable structure was uncertain, the reflective panels were slightly undersized; this eliminated the possibility of not being able to fit all the facets if the inflatable was undersized. To modify the flat panels, 0.010 in. was removed from the length of the bases on the design tables.

The approach used to assemble the reflective facets for the inflatable prototype was similar to one used for the small-scale prototypes. However, alternate application techniques for the ReflecTech® mirror film were examined such that the facet assembly could be packaged in a compact manner. As in the small-scale facet assembly, it was observed that taping two panels together creates a hinge-like junction which allows for rotation in the direction of the tape. Inspired by this, it was determined to tape the panels of the facets on alternate sides such that the junction of each panel rotates in different directions in a zig-zag fashion; this panel-joining method allows for the panels in each facet to be stacked (see Figure 5-22).

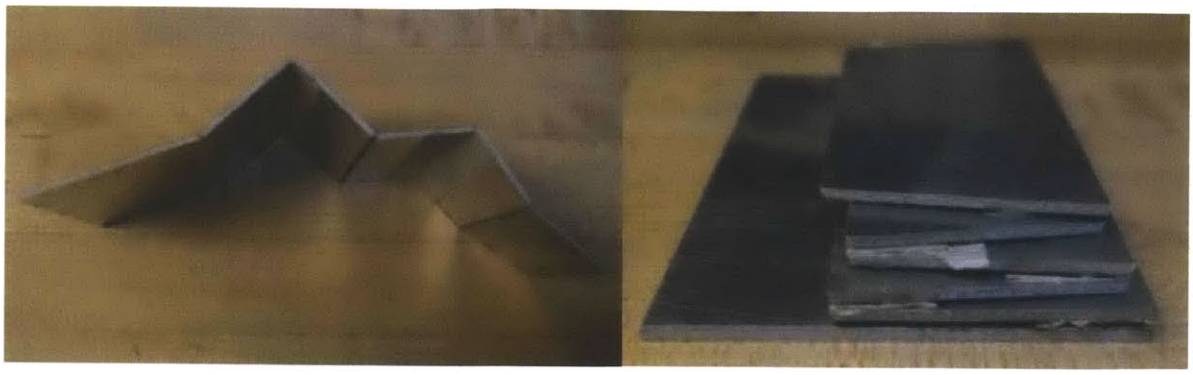

**Figure 5-22: Facet assembly concept for full-scale prototype; junction of adjacent panels are taped together on alternating faces of the panels.**

The panels for the full-scale prototype, much larger than the ones previously manufactured, were ordered from Big Blue Saw, a company that fabricates and delivers custom made waterjet parts. The initial step in the facet assembly process is shown in Figure 5-23.

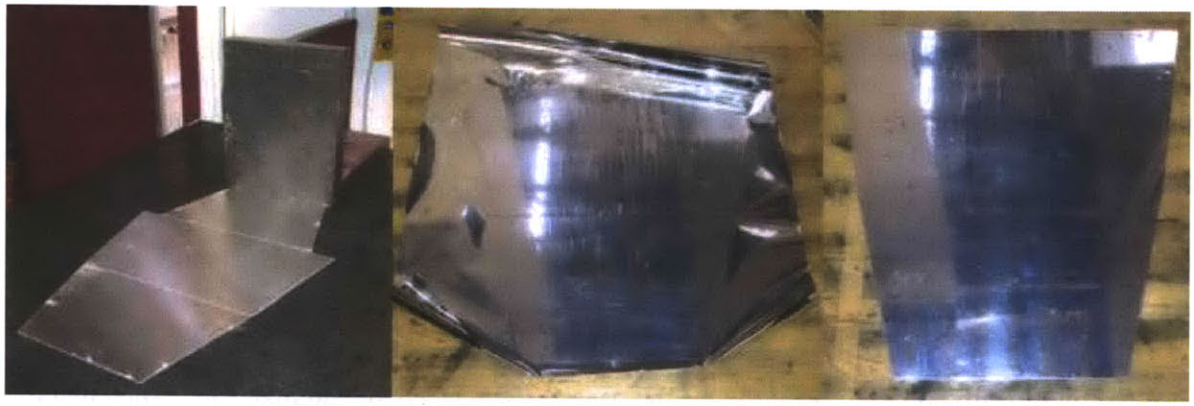

**Figure 5-23: Firsts step in facet assembly process for full-scale prototype.**

Starting from the smallest panel, pairs of adjacent panels were aligned and rested against a fixed surface for support. ReflecTech® was applied on the pair of panels and then the excess was removed using an X-Acto knife. With all three pairs of panels corresponding to a facet ready (see Figure 5-24), they were aligned on a flat surface with the un-taped surface facing upward. Strips of ReflecTech® were used to tape the adjacent pairs of panels together to fully attach all

components of the facet. Finally, Velcro strips were cut out and adhered to the back side of the panel. A picture of the fully assembled facet is shown in Figure 5-25.

**Figure 5-24: Three pairs of panels ready to be joined to complete facet assembly.**

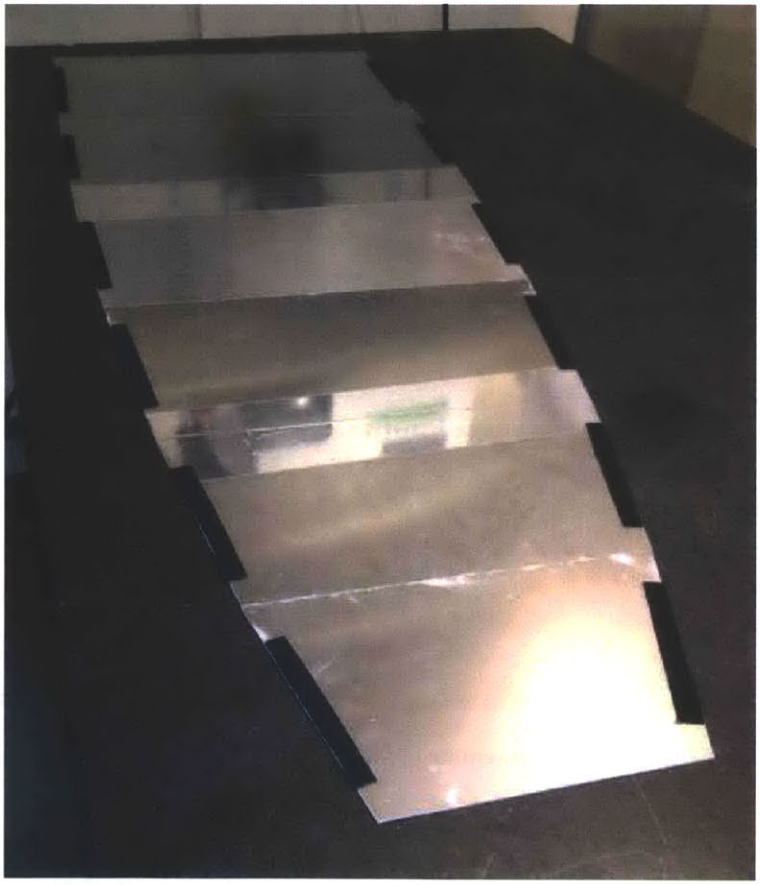

**Figure 5-25: Fully assembled facet for full-scale concentrator prototype.**

### 5.3.4 Full-Scale Prototype: Full Assembly

After all six reflective facets were assembled they were ready to be joined on the inflatable frame. For proper alignment, the flat sections on the ribs were used as guideline. At the top junction of the ribs with the upper dodecagon, there are corners that indicate the location of the upper corner of the facets. Starting with the largest panel on the top, the facet was aligned with the two corners in the inflatable and slowly unfolded while pressing down on the Velcro on the back of the facet onto the ribs for attachment. Below are pictures of the fully assembled concentrator.

**Figure 5-26: Completed assembly of inflated solar concentrator prototype.**

# Chapter 6: Testing

## 6.1 Overview

The prototypes were tested to verify the accuracy of the analytical models. As previously discussed, the main goal of the analytical models was to provide a tool that would aid in the design of a modified 3D CPC that uses flat sections to approximate both the parabolic curves and aperture geometry. The effects of making these approximations most directly affect the concentrator's aperture and exit geometries and its optical efficiency. However, it is most interesting to analyze the effects on efficiency because the only performance metric affected by the aperture and exit geometries is the concentration ratio, which remains the same after these approximations.

Two strategies were implemented in an attempt to test the optical efficiency of the concentrator. Tests were done inside, using a solar simulator, and outside using the direct sunlight. In all situations, it was crucial knowing the incidence angle on the collector plane. Since the sun moves in two axes, a simple sun tracker (see Figure 6-1) was made to align the collector's plane with one of the sun's axis and only have to consider the effect of a non-zero incidence angle in one direction. The sun tracker was made by drilling a hole through u-channel aluminum extrusion section. The drill bit was used to make a clearance hole on one leg of the extrusion but only a small dent opposite leg, enough to mark a spot concentric with clearance hole. For sun tracking, the part is placed on the surface of interest to allow light to enter the clearance hole directly and see in which spot it hits the inside opposing wall. A 0° incidence angle is obtained when the spot of light is perfectly concentric with the drilled mark (see Figure 6-1a); any deviation from this position indicates misalignment in some axis (see Figure 6-1b).

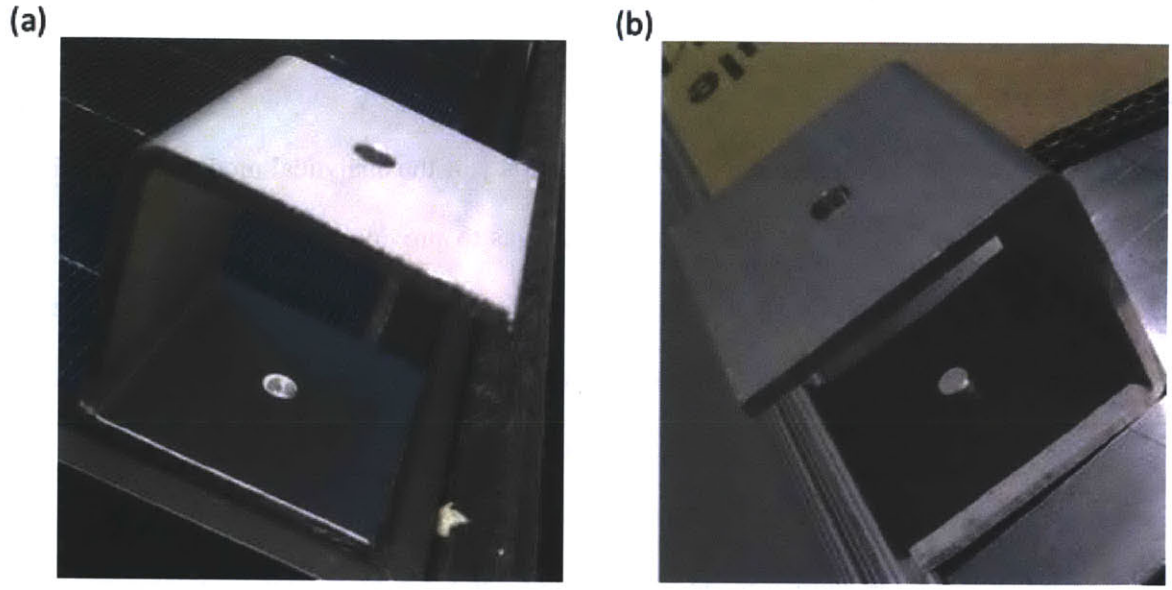


**Figure 6-1: Simple solar tracking device – (a) spot of light is almost concentric with mark, indicating it is close to aligned; (b) spot of light is shifted to the side, showing misalignment to sun's position.**

Since the motivation for this project derived from the solar cooker industry, the original idea for testing the efficiency of the system was to measure the temperatures obtained in a solar collector placed under the concentrator (e.g. tub of water). However, thermal testing requires consideration of other factors, like convective losses to the environment. Looking for a more straight-forward approach, the first thought was to use solar cells. The test would consist of measuring the current output of the solar cell with and without the solar concentrator resting over it; theoretically, the increase in output when using the concentrator would be directly correlated its optical efficiency. Yet, after a series of trials with both the small and full scale prototypes, it proved difficult to gauge the efficiency of the concentrators with this method so an alternate approach was pursued.

This alternate strategy of testing the efficiency of the concentrators was to measure illuminance, the amount of light energy incident on a surface, which is measured in lux

(lumens/$m^2$) [16].The illuminance was measured using the Vernier LS-BTA Light Sensor and data was collected using Logger Pro. A baseline lux reading was obtained by measuring the light intensity at a surface. Then, the concentrator was placed over the probe such that it measured the light intensity at the concentrator exit. Data was compared in order to determine the experimental optical efficiency of the concentrators.

## 6.2 Photovoltaics

Tabbed 2.8W solar cells (Figure 6-2a) and a 30W solar panel unit (Figure 6-2b) were ordered to be used in the testing of the optical efficiency of the small-scale and full-scale solar concentrator prototypes, respectively. The area of the units was intentioned to be as close as possible to the area of the concentrator exits to ensure that most of the light leaving the concentrators will be captured. The dimensions of the solar cell were 4.492 in. by 4.492 in. by 0.0125 in., and the dimensions of the solar panel were 17.36 in. by 21.30 in. by 0.98 in. The solar panel had wires connected to the positive and negative leads which were used to measure the output of the panel from a distance, meaning that there was no risk of blocking off light from the panel while trying to reach the leads. In order to do the same with the solar cell, wires were soldered directly to the leads.

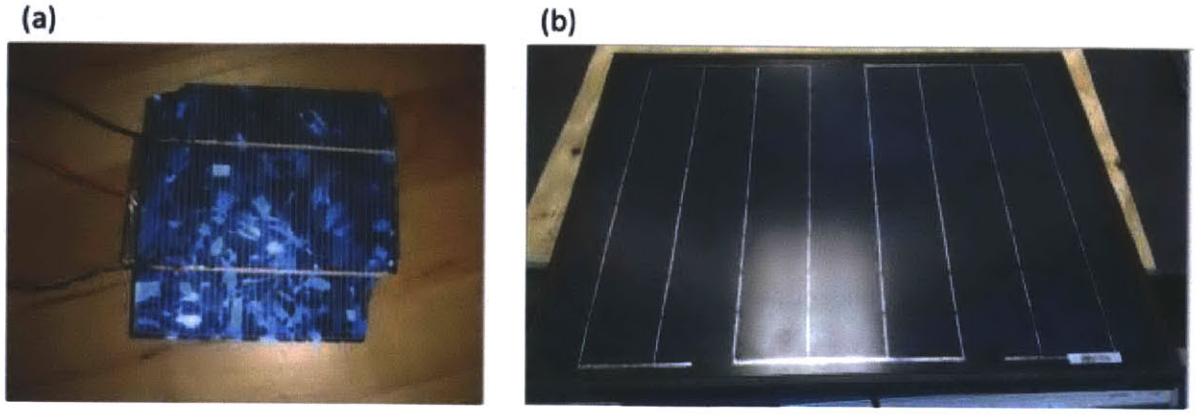


**Figure 6-2: Photovoltaic units used for testing solar concentrator prototypes – (a) 2.8W solar cell; (b) 30W solar panel**

Two different methods of measurement were used during testing with photovoltaics: a digital multimeter and an NI USB-6009 DAQ through the LabVIEW software. A digital multimeter was used during initial testing to measure the current output of the solar cell directly. However, when the photovoltaic was exposed to a high light intensity the current would not stabilize at a value, making it difficult to record accurate measurements. To address the unfavorable readings with the digital multimeter, a simple LabVIEW virtual instrument was built using the DAQ Assistant to measure current that allowed data to be captured for a specified period of time and, later, averaged. However, using LabVIEW required a different setup to measure the current output. LabVIEW requires for the circuit to be loaded with a known resistance; the DAQ measures the voltage across it and uses Ohm's Law to calculate and display the current in the circuit.

### 6.2.1 Small-Scale

In an attempt to create a controlled test experiment, part of solar simulator was reused from a previous experiment [17]. The light source consisted of a 1500 W Metal halide unit with a NEMA 3 reflector. A frame for the lamp was built using 80/20® and mounted on casters to

facilitate motion. For testing (see Figure 6-3), the solar cell was placed directly under the light (incidence angle of 0°), with and without the concentrator, and the output current was measured using a digital multimeter in both situations.

**Figure 6-3: Test setup up for testing small-scale prototype using solar cell.**

The procedure attempted was to measure the current output of the solar cell directly under the light, and also under the small-scale solar concentrator (see Figure 6-4). This sequence was repeated until five measurements were taken of each of the configurations. However, this strategy was flawed for two main reasons. First, it was not possible to precisely align the concentrator concentrically with the solar cell. Second, the current reading on the digital multimeter fluctuated greatly and it was difficult to capture an accurate measurement.

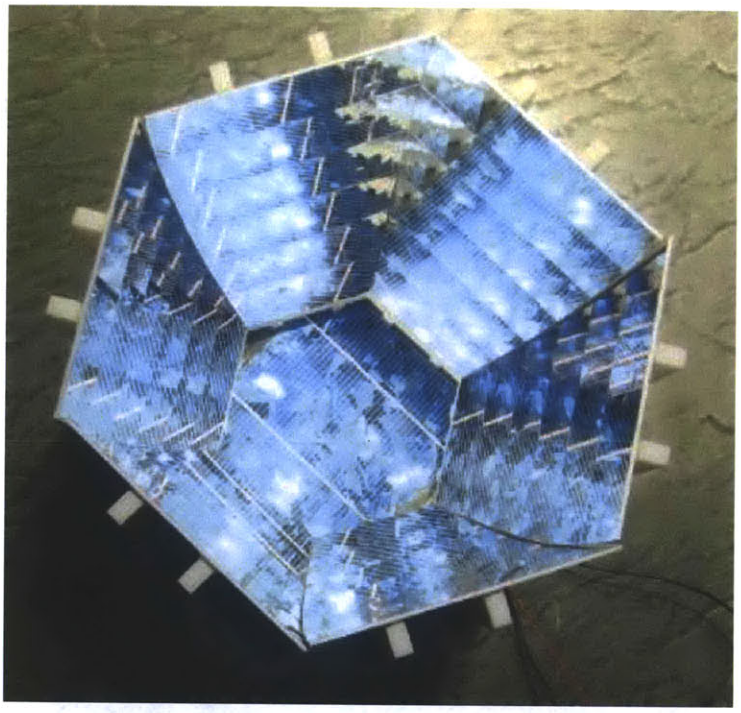

**Figure 6-4: Small-scale prototype sitting on top of solar cell for testing.**

As discussed at the beginning of Section 6.2, LabView was used to accurately record measurements. The proposed solution to align the concentrator concentrically with the solar cell, and to do so repeatedly, was to design and build a three-groove kinematic coupling [18]. A special fixture was designed for the solar cell, containing a pocket for precisely placing the solar cell in its center and three spherical holes to secure the spheres (see Figure 6-5). This part was CNC milled using the EZ-Track mill. The pocket was milled using a flat end mill and the holes were drilled using a spherical end mill. To avoid making another base for the small-scale concentrator, three V-grooves were milled into the existing base 120° from each other. Figure 6-6 shows a CAD model of the kinematic coupling for precisely and repeatedly position the solar concentrator concentrically with the solar cell.

**Figure 6-5: Solar cell fixture for kinematic coupling to small-scale concentrator**

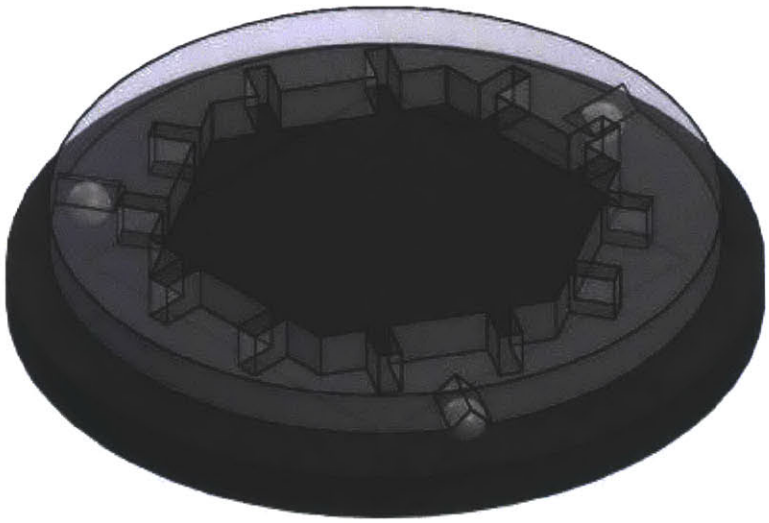

**Figure 6-6: CAD model of three-groove kinematic coupling between solar cell fixture and bottom of small-scale concentrator**

Figure 6-7 shows a picture of the fixture with the spheres and solar cell in place. The solar cell was fixed into position using double-sided tape. The corners of the solar cell were blocked off by the concentrator when mounted on the spheres, so the corners were masked such that the same solar cell area was exposed for both configurations of the test for consistent results.

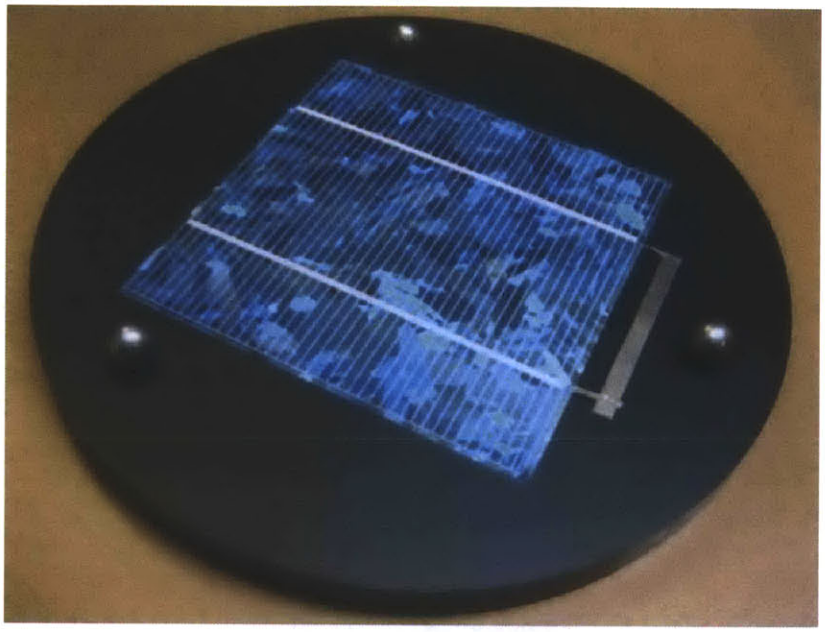

**Figure 6-7: Picture of the solar cell fixture holding the solar place in position.**

### 6.2.2 Full-Scale

The solar panel unit shown in Figure 6-2b was used for the first testing experiments of the full-scale inflatable prototype. Similar to the small-scale setup, the instinctive strategy was to create a mask for the solar panel such that the same area would be exposed with and without the solar concentrator.

For this experiment, the solar panel and concentrator were set outside to use the sun instead of the solar simulator because its reflector was not large enough to direct an even distribution of light throughout the entire aperture. Initially, the solar panel was set flat on the ground such that its normal was perpendicular to the floor. For measuring the output of the solar panel when under the solar concentrator, it was important to align the concentrator's exit with the exposed solar panel area. Due to time constraints, the position was approximated with a

SolidWorks sketch to determine the overhang distances of the solar concentrator long the dimensions of the solar panel. After preliminary current measurements, output of the solar panel unexpectedly decreased when using the concentrator. Exploring the test setup revealed that when looking into the concentrator, the solar panel's exposed area was under a shadow, meaning that incident light was not being redirected to the concentrator's exit properly. However, measuring the incidence angle of the sun (done so by measuring the shadow cast by a column of known length and calculating the formed angle) revealed that the sun was entering the aperture at an angle of 31°, larger than the acceptance half-angle of 25°. Hence, the observed behavior in the solar panel's output was to be expected.

To address this issue, an 80/20® stand was designed and assembled to tilt the solar panel at an inclination of 35° from the horizontal. Figure 6-8shows the CAD assembly model of the solar panel mounted on the fixture, while Figure 6-8b shows a picture of the stand once assembled; the images also show the mask that was used for testing.

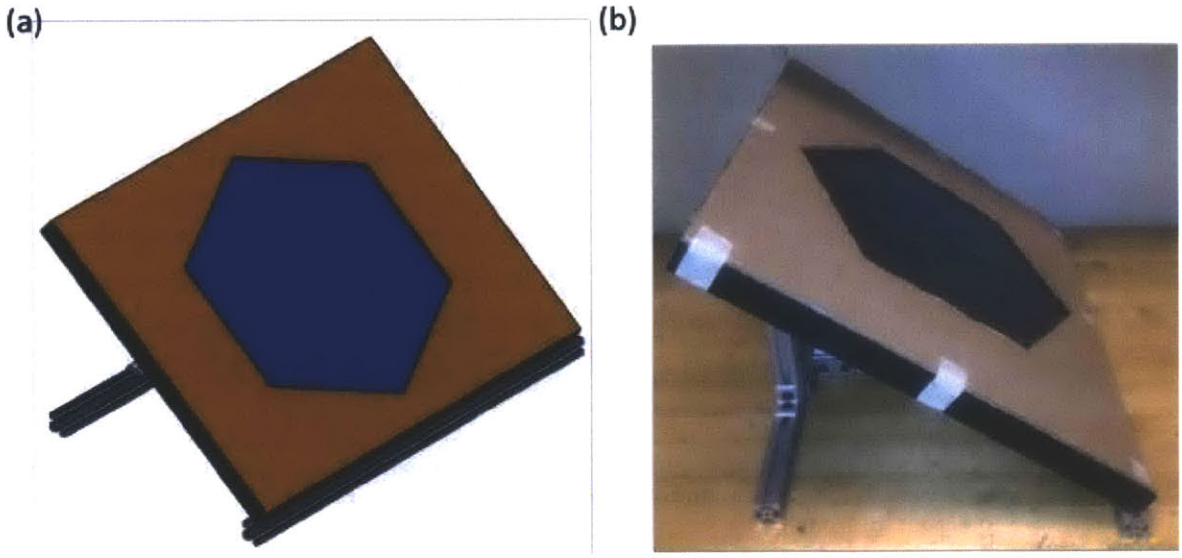


**Figure 6-8: Testing fixture for tilting solar panel and concentrator 35° from horizontal.**

For the second experimental, the inflatable concentrator also had to be tilted such that its bottom surface was coincident with the top surface of the solar panel mask, thus aligning both central axes. The solar panel fixture was mounted on a cart, which served two purposes: (1) facilitated process of moving experimental setup outside for testing, and (2) the handle provided a fixture point for attaching a rope to hold the concentrator at the desired location (see Figure 6-9a). The rope was wrapped around the handles multiple times to reduce the amount of force required to counter the weight of the concentrator. Once the concentrator was properly aligned concentrically to the solar panel and in the right orientation, the rope was tied down fixing the inclination of the concentrator. The entire setup was taken outside for a second round of testing (see Figure 6-9b).

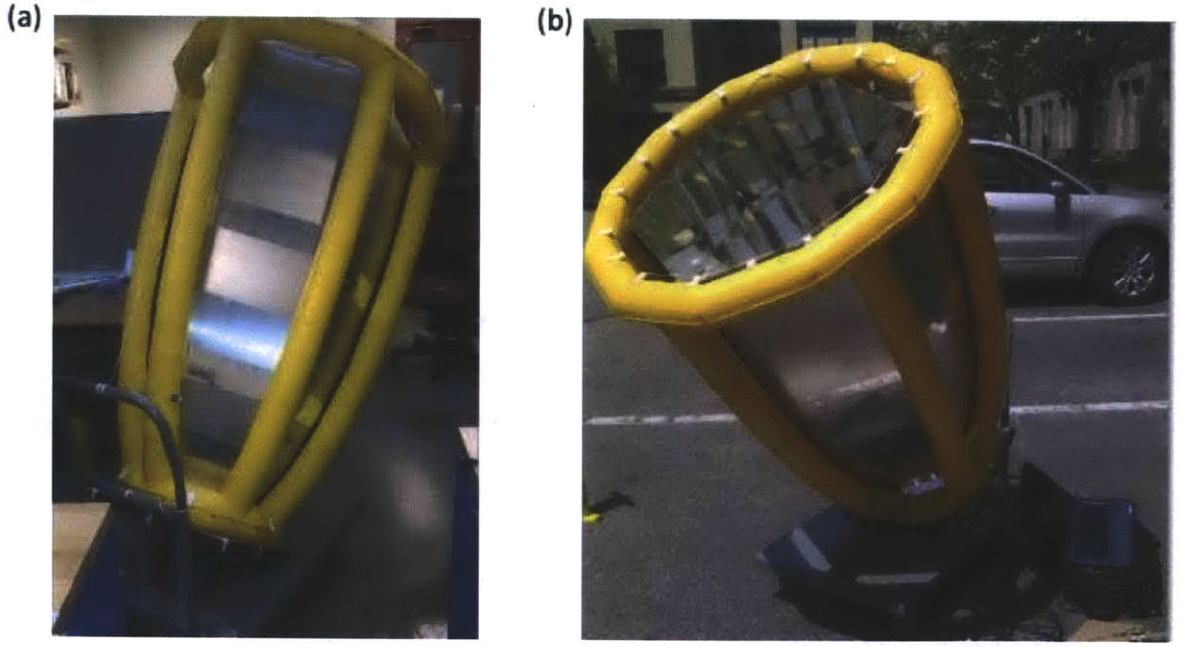


**Figure 6-9: Experimental setup for testing performance of inflatable concentrator using solar panel, 35° inclination – (a) rear view showing string used to hold concentrator in position; (b) frontal view.**

Despite repeated attempts, the concentrator did seem to perform successfully using the solar panel output readings. Based on simple observation, it was clear that there is a higher light intensity at the solar concentrator's exit. So even if the analytical model proved to be inaccurate, use of the concentrator should yield some improvement in performance. Thus, various steps were taken in order to discover the root of the problem. First, the analytical model was revised. There was concern that the first-order analytical model was not capturing the full performance of the system, which is why the ray tracing code was elaborated (Section 4.3). In addition, for both small-scale and full-scale testing, it was observed that the photovoltaic units, acting as the collector in the solar system, were displaced by some distance from the theoretical collector position depending on the particular setup. Second, due to the lack of expertise in photovoltaics, there was concern that solar panels behave different under different light conditions which may affect the measurements. Further research into solar panel technology revealed that during for solar panel assembly, individual solar cells (twelve in this particular panel) are connected in series. Thus, if any of the solar cells are shaded, that cell will cap the maximum amount of current that can flow through circuit. In all of the testing done using the solar panel up to this point, some portion of it had been covered, either by the mask or by the bottom inflatable in the full-scale prototype. Consequently, this experimental setup would never yield reliable output measurements with or without the solar concentrator.

The solar panel unit could not be used for testing the full-scale prototype because some portion of the panel would always be under a shadow since its area is larger than exit area of the concentrator. Staying with the approach of using photovoltaics to test the prototypes, the plan was to build another test setup that allow for the full-scale prototype to be tested with the solar cells used in the small-scale testing. A piece of sheet metal was divided into a nine cell grid

using electrical tape, such that the center cell in the grid system would be concentric with the concentrator. The plan was to measure the current output of the solar cell at different locations in the grid and map out position-sensitive efficiency of the concentrator throughout its exit area (see Figure 6-10). Due to the brittle nature of the solar cells, double-sided tape was used to attach the solar cell to a piece of sheet metal of the same dimensions to avoid the need to attach and remove the solar cell continuously, which would most likely break it. To accurately place the solar cell in each grid location, the electrical tape grid divider was used to guide the edges of the solar cell's sheet metal backing.

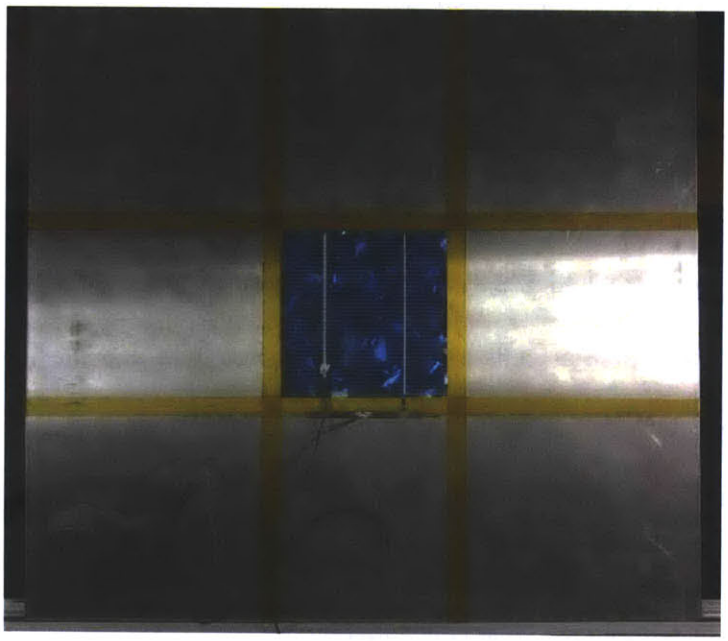

**Figure 6-10: Solar cell grid for testing of full-scale prototype.**

The second experimental setup for testing the full-scale prototype did not succeed in capturing the true optical efficiency of the concentrator. When using the concentrator, the current output of the solar cell would increase momentarily, but then dramatically decrease, even past the point of its current output without the concentrator. This behavior was bizarre because logic

dictates that the solar cell should not be producing less current when exposed to a higher light intensity. The sheet metal when under the concentrator, felt very hot to the touch. This led to the formulation of the theory that the temperature in the solar cells was getting high enough to the point where the efficiency deteriorates. In order to quantify the temperature of the solar cells during the test, a thermal camera was used.

## 6.3 Light Sensor

A light sensor was used to measure the light intensity in the regions of interest. The Vernier LS-BTA Light Sensor measures illuminance in the range of 0 – 150,000 lux (see Figure 6-11). For the experiments, a plate was arranged in orientations with known incidence angles of the sun. A slot was cut out along the centerline of the plate which allowed the light sensor probe to fit and slide in it. A washer was placed around the probe on each side of the plate to ensure it remained perpendicular to the plane, allowing the light sensor to point in the direction of the plate's normal and measure the light intensity resulting from the given incidence angle of the sun's rays. After obtaining a baseline lux value for the specific orientation, the concentrator was mounted directly on the plate's surface, aligning the normal vectors of the plate and the concentrator's aperture and exit. This alignment allowed for the probe to measure the light intensity in the same orientation as the concentrator's axis. The difference between both illuminance measurements was used to determine the experimental optical efficiency of the system.


**Figure 6-11: Light sensor used to measure illuminance; washers were fabricated for aligning light sensor probe on experimental setup.**

A problem with using the light sensor in this particular application was that the illuminance of direct sunlight was near the maximum of the sensor's range. The solar concentrators were expected to magnify the light intensity of the sun by a factor determined by their concentration ratio; thus, the illuminance was much higher than what could be measured by sensor. The solution was to use a neutral density filter (ND filter), which reduces the intensity of all the wavelengths of light equally by a specified factor. For this experiment, an ND20A filter was used; this filter is rated with an optical density of 2.0, indicating that only 1% of the incoming light is transmitted.

Besides testing the small-scale and full-scale prototypes with this experimental setup approach, a flat plate concentrator was also tested. The ray tracing analysis for flat plate concentrators is much simpler than for the modified CPC design due to its simple geometry. Comparing the theoretical and experimental optical efficiencies of the flat plate concentrator was expected to give a general idea of what to expect for the other prototypes.

### 6.3.1 Small-Scale

This test of the small-scale prototype was not done inside using the solar simulator. Since the same test procedure was done with the full-scale prototype and the flat panel concentrator, it was decided to also do this test with sunlight for consistency. Below is an image of the experimental setup used:

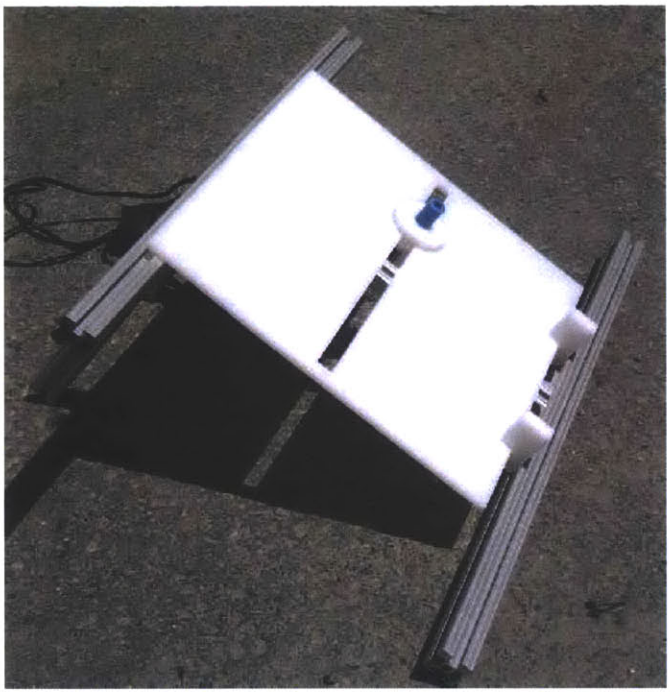

**Figure 6-12: Experimental setup for testing baseline lux.**

A slot was cut out along the center of a 1x1 ft. piece of HDPE using the waterjet; the slot was dimension such that the sensor probe could slide in with ease. The 80/20® stand shown was the same one as in Figure 6-8 but flipped upside down to allow for the HDPE plate to rest comfortably. A digital level was used to measure the inclination of the plate as 34.7° from the horizontal. After measuring the baseline illuminance, the small-scale prototype was placed on the HPDE plate, as shown in Figure 6-13. With the concentrator in place, lux was recorded for ten seconds while the probe was moved along a straight line at the concentrator's exit. Since the

concentrator's exit has the shape of a hexagon, this measurement was taken in two ways, moving the probe between opposing corners and moving it between opposing sides.

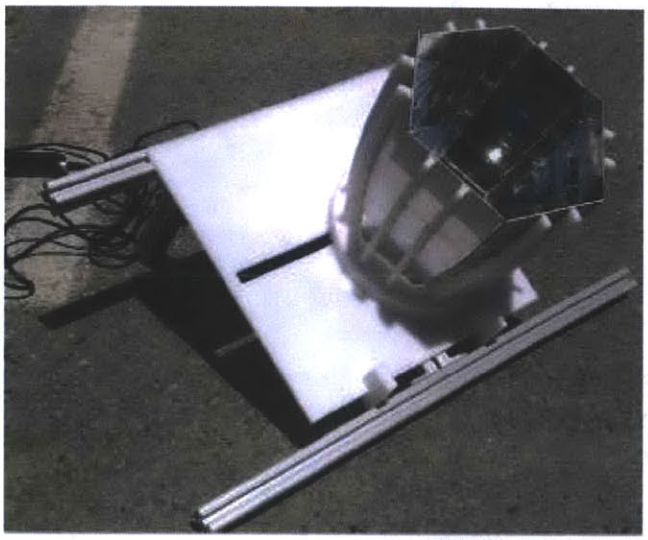

**Figure 6-13: Experimental setup for measuring illuminance at the exit of the small-scale prototype.**

### 6.3.2 Full-Scale

The slot for guiding the light sensor probe was added directly on the same plate that was originally used for the solar cell grid testing of the full-scale prototype (see Figure 6-14). While mounting the light sensor probe on the sheet metal plate (35° incline), the length of the probe above the surface was measured so that its tip would be right at the concentrator's exit. Illuminance was measured in this configuration and then the concentrator was mounted on the sheet metal plate (see Figure 6-15); illuminance was re-measured at the exit of the full-scale prototype.

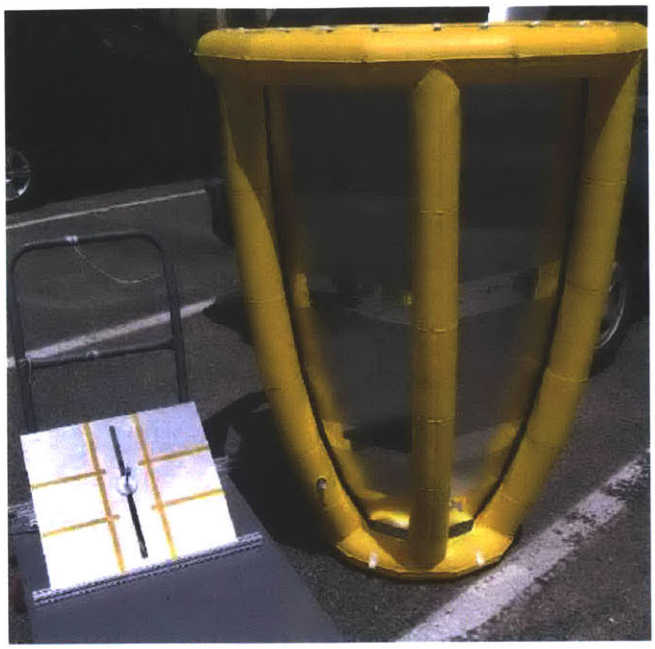

**Figure 6-14: experimental setup, full-scale**

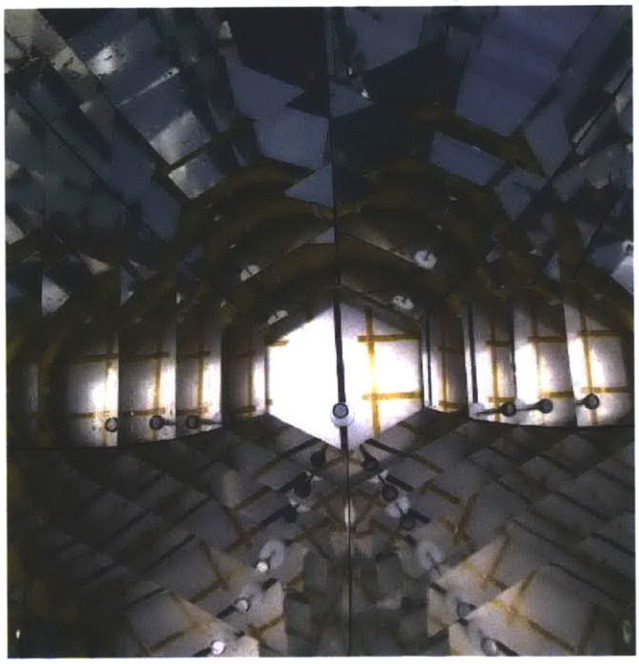

**Figure 6-15: Look inside full-scale concentrator, measuring illuminance**

### 6.3.3 Flat Panels

The flat plate concentrator consists of placing four reflective panels, inclined at a specific angle from the vertical, around a collector. Brackets were designed to hold the flat panels at 20° from the vertical and interface with the HDPE plate used during the testing of the small-scale prototype. The brackets were manufactured out of 0.5 in. thick HDPE using the waterjet (see Figure 6-16).

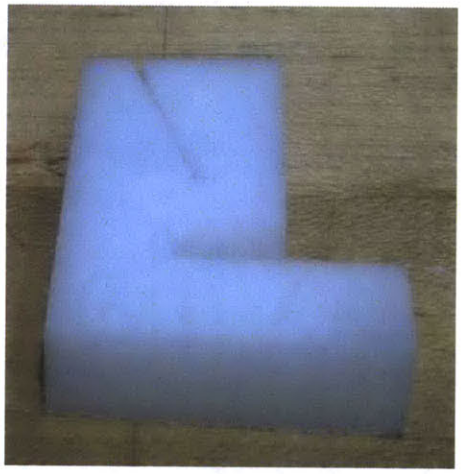

**Figure 6-16: Bracket for flat plate concentrator.**

Manufacturing of the reflective panels consisted of cutting four pieces of sheet metal, using the shear and coating them with ReflecTech® mirror film. Sheet metal for the reflective panels was reused from panels originally made for the facets of the inflatable concentrator, which had a height of 11.25 in. The pieces were cut to 12 in. in length in order to fully cover the sides of the collector. After assembling the flat plate concentrator, the same test procedure previously outlined was followed (see Figure 6-17).

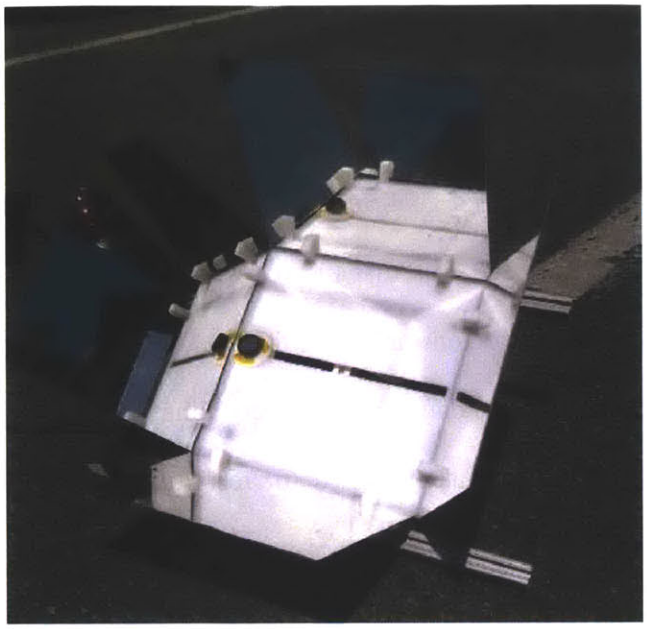

**Figure 6-17: Experimental setup to test illuminance for flat plate concentrator design.**

# Chapter 7: Results

## 7.1 Photovoltaics

Solar cells proved not to be a good testing media for measuring the performance of the solar concentrators. The hypothesis was that the solar cells were heating up too much, to the point that their performance was deteriorating. In the attempt to obtain accurate measurements, the solar cell was kept covered until data was being recording; measurements were usually taken for around two seconds. This approach worked for recording current output of the solar cell without the concentrator. However, when the concentrator was used, drop in output was noticeable in the short two second window. Data was captured for a longer period of time to get a better understanding of the current output through time (see Figure 7-1). Another reason this behavior was concerning was that as tests were repeated, the total exposure time of the solar cell under the lamp accumulated, possibly altering the results of subsequent measurements.

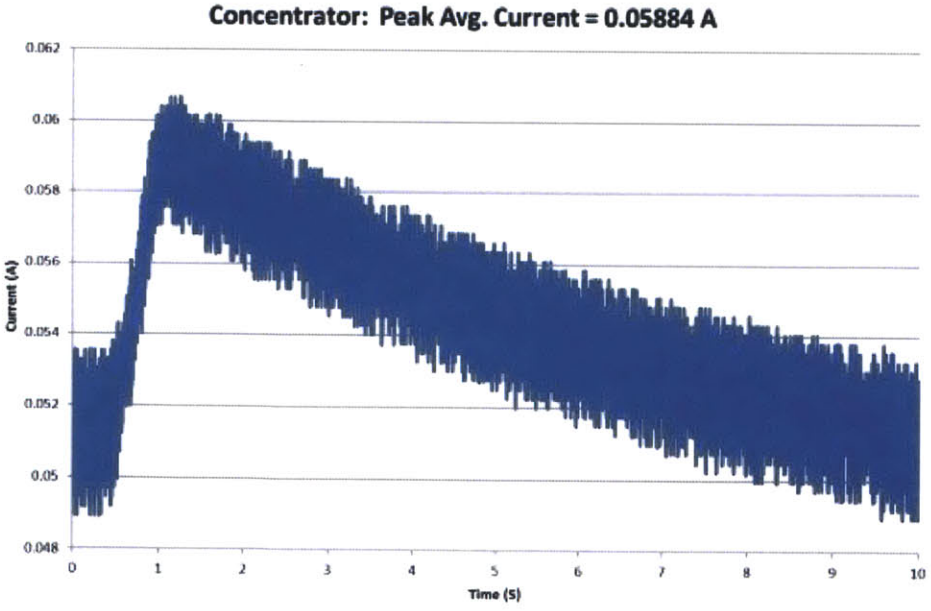


**Figure 7-1: Current output of solar cell under small-scale concentrator prototype.**

During the full-scale concentrator testing, an attempt was made to use solar cells in the experimental setup. The same behavior described above was observed in this experiment where the current output would momentarily increase, but it would instantly start decreasing, passing below point of the original output without the concentrator. A thermal camera was used to measure and compare the temperature of the solar cell under direct sunlight (see Figure 7-2a) and under the concentrator (see Figure 7-2b). As shown, there is a considerable increase in temperature in the solar cell. The time stamps in the images show a 19 minutes interval between the pictures. However, the solar cell was not under the concentrator for that period of time. The image in Figure 7-2b was taken about a minute of the concentrator being mounted on top of the solar cell on a different occasion.

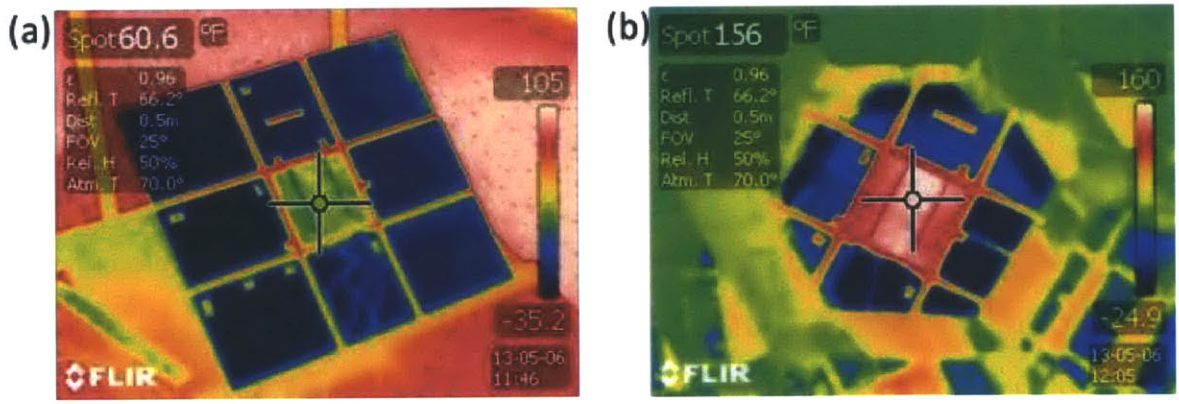


**Figure 7-2: Temperature readings of solar cell measured with thermal camera – (a) 60.6 °F under direct sunlight; (b) 156 °F under inflatable solar concentrator.**

## 7.2 Light Sensor

Measurements of illuminance were collected and used to describe the experimental performance of the solar concentrator prototypes. Theoretically, the illuminance at the receiver of a solar concentrator should be equal to the illuminance at the aperture times the effective concentration ratio. In the experimental setup, both measurements were taken at the same

location because without the concentrator, the illuminance was only determined by the angle of incidence of the sun (without the concentrator, the illuminance at the plate is the same as in the concentrator's aperture). The effective concentration ratio for each concentrator was calculated from the analytical model and its dimensions (see Table 4). The table shows the particular incidence angle of the sunlight, which was used to determine the optical efficiency of each design.

**Table 4: Summary of expected performance of solar concentrators.**

| | Small-Scale ($\theta_i = 6°$) | Full-Scale ($\theta_i = 8°$) | Flat Panel ($\theta_i = 8°$) |
|---|---|---|---|
| Aperture Area [in$^2$] | 45.18 | 712.48 | 328.70 |
| Exit Area [in$^2$] | 17.16 | 127.27 | 144 |
| $CR$ | 2.63 | 5.60 | 2.28 |
| $\eta_{eff}$ | 97.3% | 95.6% | 97.3% |
| $CR_{eff}$ | 2.56 | 5.35 | 2.22 |

The measured values of illuminance were 1% of the real magnitude because of the ND filter that was used. This did not affect the analysis because all measurements were scaled down by the same amount, not affecting the relative change between them. The procedure to determine the accuracy of the analytical models from the experiment results was outlined in Table 5. The baseline lux represents the illuminance present at the aperture of the solar concentrator at the given incidence angle. Theoretically, the illuminance at the exit of the concentrator should be the illuminance at the aperture times the effective concentration ratio of design. Given that the uncertainty of the lux measurements, an online uncertainty calculator [19] was used in order to properly propagate the uncertainty values trough out the calculations. Thus, the expected

illuminance at the exit of the concentrator was compared to the actual value measured; this difference was used to determine the accuracy of the analytical mode (row labeled "Error").

**Table 5: Illuminance data used to determine the accuracy of the analytical models by comparing the expected and measured optical efficiency of the systems.**

| | Small-Scale ($\theta_i = 6°$) | Full-Scale ($\theta_i = 8°$) | Flat Panel ($\theta_i = 8°$) |
|---|---|---|---|
| Effective CR | 2.56 | 5.35 | 2.22 |
| Baseline [lux] | 2,432 ± 25.59 | 2,097 ± 28.92 | 4,415 ± 77.35 |
| Concentrator Illuminance - Expected[lux] | 6,226 ± 66 | 11,220 ± 150 | 9,800 ± 170 |
| Concentrator Illuminance – Measured [lux] | 5,588 ± 27.14 | 11,010 ± 72.24 | 7,366 ± 62.28 |
| Error | 11.4 ± 1.3 % | 1.9 ± 1.6 % | 33.1 ± 2.6 % |

The error between the expected and measured values of illuminance was the largest for the flat panel reflectors. This seemed ironic because the purpose of testing the flat panel design was to create a benchmark for the other tests since its analytical model was much simpler. Yet, this error was expected because the flat panels did not extend past the width of the receiver. In the three-dimensional regime, the sunlight reflections do not stay in the same plane meaning that some of the reflected rays were lost because there were gaps in the 3D flat panel concentrator. Since the CPC concentrators are fully enclosed, these out-of-plane reflections are able to stay in the concentrator despite the analytical model not accounting for them.

There are certainly some sources of error due to the manufacturing and assembly processes of the concentrators. The more noticeable errors were: imperfections in the reflective surface and gaps between the facets. The reflective surfaces were far from ideal because of the bubbles that developed during the assembly process and dirt on the surface. Despite the

numerous bubbles in the reflective surface, rays can still be reflected off the bubbles and reach the receiver. Through a simple test, a laser-pointer was shined at a bubbled and it was observed that although the image of the reflection gets distorted, it is still reflected. The fact that the CPC is a non-imaging concentrator makes it so that bubbles don't affect efficiency as much as it would in other imaging-type designs. To minimize dirt on the reflective surfaces, the original attempt was to remove the protective film at the time of testing. Yet, given the numerous failed experiments, the concentrator did collect dust, which makes it more representative of what would happen in the field; the attempted solution was to clean the surfaces as best as possible before running experiments.

The other noticeable source of error was the gap between the facets, especially in the inflatable concentrator. As mentioned, the geometry of the reflective panels was scaled down by a small factor to account for manufacturing errors in the inflatable production. However, the inflatable structure ended up being reasonably compliant, meaning that if the reflective panels would have been slightly oversized, it could have been arranged for a snug fit. There is certainly a level of design iterations that must be done to determine the precision of the inflatable manufacturing process to determine the right facet design.

# Chapter 8: Conclusions

In order for people to continuously adopt renewable energy technology, it must be simple to use, available at low cost, and it must perform competitively. In the case of the solar cooker, potential users may be choosing not to take advantage of the technology because they are unwilling to deal with its inconvenient aspects. In particular, some solar concentrators required for the operation of cookers constrain the cost, size, and weight of the device. Despite solar concentrators having been studied and built for years, there is still room for growth and improvement. The goal of this project was to take existing technology and approach it from a slightly different perspective.

The proposed design was intended to simplify the manufacturing process of a well-known solar concentrator and to provide its users with a different set of advantages. The concept of the inflatable solar concentrators gives users the option of enjoying the same benefits offered by a typical concentrator but with the added advantages of portability, lighter weight, and potentially lower cost, which may be achieved due to the use of simple structures to approximate ideal geometries.

As it has been established through the study of solar concentrators, different designs are considered for different applications; this includes different performance metrics for the same type of concentrator. Consequently, an analytical model was desired that could help determine the dimensions necessary to meet certain design requirements. This does not mean that the concentrator must be fit for any application, but if it's not, the model would aid in the decision making process to discard it.

An analytical model was developed that characterized the effect of the design parameters in the optical efficiency of the system. In order to be useful, the analytical model was used to design two differently scaled prototypes that were built and tested. Tests of the concentrators were a success, showing a high accuracy of the model. Furthermore, during the course of this project, a semi-automated design process was developed by linking the analytical models to design tables governing the dimensions of part drawings necessary for building a concentrator.

As is, the inflatable concentrator is not ready for the market. The current design uses sheet metal panels that must be assembled separately and attached to the inflatable structure. Not only does this add unnecessary weight to the device, but it does not allow the structure to be packed when uninflated. The next step in the development of this product is forming the reflective facets out of Mylar and attaching them permanently to the inflatable structure. If this is successful, it would simplify the assembly process and allow for easy packaging once uninflated. Another aspect worth exploring is the effect of truncation of the inflatable solar concentrator design. Studies have shown that the CPC can be shortened without losing much in efficiency. It would be interesting to test if this would be the case with the suggested design. Furthermore, the efficiency of the system with either of these changes must be tested in order to verify that accuracy of the analytical models still holds.

# BIBLIOGRAPHY


[1] W. B. Stine and M. Geyer, "Power From the Sun," 2011. [Online]. Available: www.powerfromthesun.net/book.html. [Accessed 7 July 2012].

[2] W. K. Macura, "Angle of Incidence," 8 May 2013. [Online]. Available: http://mathworld.wolfram.com/AngleofIncidence.html. [Accessed 19 May 2013].

[3] F. d. Winter, Solar Collectors, Energy Storage, and Materials, Cambridge: MIT Press, 1990.

[4] E. W. Weisstein, "Reflection," 2007. [Online]. Available: http://scienceworld.wolfram.com/physics/Reflection.html. [Accessed 16 January 2013].

[5] E. W. Weisstein, "Snell's Law," 2007. [Online]. Available: http://scienceworld.wolfram.com/physics/SnellsLaw.html. [Accessed 16 January 2013].

[6] A. Rabl, "Comparison of Solar Concentrators," *Solar Energy,* vol. 18, pp. 93-111, 1976.

[7] Cool Earth Solar, "Cool Earth Solar," TMB Creative, 2012. [Online]. Available: http://www.coolearthsolar.com/technology. [Accessed 17 September 2012].

[8] E. B. Cummings, "Infltable solar concentrator balloon method and apparatus". US Patent 8,074,638, 13 December 2011.

[9] J. Rodgers, "Infltable curved mirror". US Patent 3,054,328, 23 December 1962.

[10] G. Barthel, "Inflatable mirror construction capable of being formed into a permanently rigid structure". US Patent 3,326,624, 20 June 1967.

[11] J. Lucas and L. Sylla, "Inflatable solar collector". US Patent 4,432,342, 21 February 1984.

[12] "Connox: Living Design Shop," 2012. [Online]. Available: http://www.connox.com/categories/cooking/cooking-knives/folding-colander.html. [Accessed 30 May 2012].

[13] "Natures Organic Market," 2012. [Online]. Available: http://www.naturesorganicmarket.com/images/silicone_collapsible_colander.jpg. [Accessed 30 May 2012].

[14] "Tmart," 2012. [Online]. Available: http://cdn1.image-tmart.com/prodimgs/J/J7403/Stainless-Steel-Travel-Folding-Collapsible-Cup_320x320.jpg.

[Accessed 30 May 2012].

[15] R. Amarasekara, "Energy for Cooking," 1994. [Online]. Available: http://www.ideasrilanka.org/PDFDownloads/energy%20for%20cooking.pdf. [Accessed 11 December 2012].

[16] "Dnp Denmark," 2013. [Online]. Available: From http://www.dnp-screens.com/DNP08/Technology/Basic-Visual/What-is-light/Illuminance.aspx. [Accessed 6 May 2013].

[17] D. S. Codd, A. Carlson, J. Rees and A. H. Slocum, "A low cost high flux solar simulator," *Solar Energy,* vol. 84, pp. 2202-2212, 2010.

[18] A. H. Slocum, "Design of three-groove kinematic couplings," *Precision Engineering,* vol. 14, no. 2, pp. 67-76, 1972.

[19] T. W. Shattuck, "Uncertainty Calculator," Colby College Chemistry, [Online]. Available: http://www.colby.edu/chemistry/PChem/scripts/error.html. [Accessed 16 May 2013].

# APPENDIX A

1. Matlab code for first-order ray tracing analysis – optical efficiency as a function of incidence angle and number of panels.

```
% First-order ray tracing analysis

clc
clear all
close all

a = 4; % aperture radius, in.
acceptance = 40; %deg
th = degtorad(acceptance);
b = a*sin(th); % collector radius, in.

% Concentrator Height
L = (a+b)*cot(th); %in.
% Focus of parabola (curve for each leg)
f = L*sin(th)^2/cos(th);

% Points in parabola, x-y plane
F = [-b,0]; %focus
F2 = [b,0];
H = [a,L]; %end of parabola
H2 = [-a,L];

% Points of parabola in u-v plane (rotated by th)
[uF,vF] = rotateToTilted(F(1),F(2),th);
[uF2,vF2] = rotateToTilted(F2(1),F2(2),th);
[uH,vH] = rotateToTilted(H(1),H(2),th);
[uH2,vH2] = rotateToTilted(H2(1),H2(2),th);

%Vertex
h_vert = uF;
k_vert = vF-f;

%Equation in roated Axis (x' = u, y' = v)
u = linspace(uF2,uH);
v = (u-h_vert).^2/(4*f)+k_vert;

%Add second leg
[uF1L,vF1L] = rotateToTilted(F(1),F(2),-th);
[uF2L,vF2L] = rotateToTilted(F2(1),F2(2),-th);
[uH1L,vH1L] = rotateToTilted(H2(1),H2(2),-th);
[uH2L,vH2L] = rotateToTilted(H(1),H(2),-th);

h_vert_L = uF2L;
k_vert_L = vF2L-f;

uLeft = linspace(uH1L,uF1L);
vLeft = (uLeft-h_vert_L).^2/(4*f)+k_vert_L;
```

```
%Transorm equation of left leg to right leg coordinate system
[xLeft,yLeft] = rotateToOriginal(uLeft,vLeft,-th);

%Equation of Left leg in same u-v system as right leg, for plotting
[uLeftPlot,vLeftPlot]=rotateToTilted(xLeft,yLeft,th);

%% Define collector, or concentrator exit

xCollector = linspace(-b,b);
yCollector = zeros(size(xCollector));
[uCollector,vCollector]=rotateToTilted(xCollector,yCollector,th);

%% Input Parameters

numPts = 5; % number of pts where ray hits
panels = 15;
incidence_max = 30; %deg

%% Generate equations for CPC panels

%Initialize values
x_line = {0,0};
y_line = {0,0};
x_endpoints = zeros(panels,panels+1);
y_endpoints = zeros(panels,panels+1);
x_endpoints(:,1) = uF2;
y_endpoints(:,1) = vF2;
m = zeros(panels,panels);
normal_dir = {0,0}; %normal vector to each panel
refl_dir = {0,0}; %direction of reflected ray from a panel
angle_normal = zeros(panels,panels); %angle of normal vector for each panel

%% Generate Incident Rays

inc_dir = zeros(1,2); %direction of incident ray
t_par = linspace(-20,20,5); % parametric parameter, incident ray
t_par_refl = linspace(0,20,5);

%Vectors [m,n]to store coordinates of rays
%m: incidence angle; n: point of entry
xIncidence = {0,0};
yIncidence = {0,0};
xReflection = {0,0};
yReflection = {0,0};

incidenceAngle = zeros(1,incidence_max+1);

%Points of entry on concentrator aperture
xAperture = linspace(-a+.001,a-.001,numPts);
yAperture(1:length(xAperture)) = L;
[uAperture,vAperture]=rotateToTilted(xAperture,yAperture,th);
```

```
%% Ray Tracing Analysis

totalGood = zeros(panels,incidence_max+1);
totalBad = zeros(panels,incidence_max+1);
totalRays = zeros(panels,incidence_max+1);

bad = zeros(panels,incidence_max+1);
good = zeros(panels,incidence_max+1);

goodRays = {0,0};
reflections = {0,0};
reflectivity = {0,0};
optEfficiency = zeros(panels,incidence_max+1);

for n = 1:panels
    intSizePanels = (uH-uF2)/n;
    x0 = 0;
    y0 = 0;
    x1 = 0;
    y1 = 0;

%     figure()
%     plot(u,v);
%     hold on;
%     plot(uLeftPlot,vLeftPlot)
%     h1 = plot(uCollector,vCollector,'--');
%     xlim([-5 12]);
%     ylim([-3 10]);
% %     axis equal
%     title('Ray Tracing: Incidence Angle = 30 deg','FontSize',12)
%     xlabel('U-axis','FontSize',12)
%     ylabel('V-axis','FontSize',12)


    for i = 0:incidence_max
        incidenceAngle(i+1) = acceptance-i;
        th_incidence = degtorad(i);
        inc_dir = [sin(th_incidence),cos(th_incidence)];
        for ray = 1:numPts
%             ray
            xIncidence{i+1,ray} = uAperture(ray) + t_par*inc_dir(1);
            yIncidence{i+1,ray} = vAperture(ray) + t_par*inc_dir(2);

%             h2 = plot(xIncidence{i+1,ray},yIncidence{i+1,ray},'r');


[x0,y0]=intersections(xIncidence{i+1,ray},yIncidence{i+1,ray},uCollector,vCol
lector);
            if ~isempty(x0)

%                 plot(x0,y0,'.k','MarkerSize',20)

                good(n,i+1) = good(n,i+1) + 1;
                goodRays{n,i+1}(ray) = 1;
                reflections{n,i+1}(ray) = 0;
```

```
%                 'good - no reflections!'
            else
                for section = 1:n % look at each panel independently
                    x_endpoints(n,section+1) = x_endpoints(n,section) +
intSizePanels;
                    y_endpoints(n,section+1) = (x_endpoints(n,section+1)-
h_vert)^2/(4*f)+k_vert;
                    m(n,section) =
slope(x_endpoints(n,section)+intSizePanels/2,h_vert,f);
                    x_line{n,section} =
linspace(x_endpoints(n,section),x_endpoints(n,section+1),numPts);
                    y_line{n,section} = m(n,section)*(x_line{n,section}-
x_endpoints(n,section))+y_endpoints(n,section);
                    angle_normal(n,section) = pi/2 - atan(m(n,section));
                    normal_dir{n,section} = [-
cos(angle_normal(n,section)),sin(angle_normal(n,section))];
                    refl_dir{n,section} = -inc_dir +
2*(dot(inc_dir,normal_dir{n,section}))*normal_dir{n,section};

%                     h4 =
plot(x_line{n,section},y_line{n,section},'LineWidth',3);

                    %Does ray hit this panel?

[x0,y0]=intersections(xIncidence{i+1,ray},yIncidence{i+1,ray},x_line{n,sectio
n},y_line{n,section});
                    if ~isempty(x0)
%                         'Reflection!'
%                         [x0,y0]
%                         n
%                         section
%                         plot(x0,y0,'sk','MarkerSize',10)
                        reflections{n,i+1}(ray) = 1;
                        xReflection{i+1,ray} = x0(1) +
t_par_refl*refl_dir{n,section}(1);
                        yReflection{i+1,ray} = y0(1) +
t_par_refl*refl_dir{n,section}(2);

%                         h3 =
plot(xReflection{i+1,ray},yReflection{i+1,ray},'g','LineWidth',2);


[x1,y1]=intersections(xReflection{i+1,ray},yReflection{i+1,ray},uCollector,vC
ollector);
                        if ~isempty(x1)
                            good(n,i+1) = good(n,i+1) + 1;
                            goodRays{n,i+1}(ray) = 1;
%                             plot(x1,y1,'.k','MarkerSize',20)
%                             good(n,1) = good(n,1) + 1;
%                             'good - 1 reflection'
                        else
                            bad(n,i+1) = bad(n,i+1) + 1;
                            goodRays{n,i+1}(ray) = 0;
%                             bad(n,1) = bad(n,1) + 1;
%                             'bad - reflection went away'
                        end
```

```
                    end
                end
            end
        end
        reflectivity{n,i+1} = goodRays{n,i+1}.*(0.93.^reflections{n,i+1});
        optEfficiency(n,i+1) = sum(reflectivity{n,i+1}*1/numPts);
    end
end

% legend([h1 h4 h2 h3 ],{'Collector','Panels','Incident Rays','Reflected
Rays'},'Location','Southeast')


figure()
surf(incidenceAngle,1:panels,optEfficiency)
xlabel('Incidence angle (deg)')
ylabel('# of panels')
zlabel('Optical Efficiency')
```

2. Matlab code for first-order ray tracing analysis – optical efficiency as a function of incidence angle and number of ribs, constant number of panels. Code for fixed incidence angle is just a modification of this one.

```
%%

clc
clear all
close all

a = 4; % aperture radius, in.
acceptance = 40; %deg
th = degtorad(acceptance);
b = a*sin(th); %collector radius, in.

% Concentrator Height
L = (a+b)*cot(th);
% Focus of parabola (curve for each leg)
f = L*sin(th)^2/cos(th);

% Points in parabola, x-y plane
F = [-b,0]; %focus
F2 = [b,0];
H = [a,L]; %end of parabola
H2 = [-a,L];

% in u-v plane (rotated by th)
[uF,vF] = rotateToTilted(F(1),F(2),th);
[uF2,vF2] = rotateToTilted(F2(1),F2(2),th);
[uH,vH] = rotateToTilted(H(1),H(2),th);
[uH2,vH2] = rotateToTilted(H2(1),H2(2),th);

%Vertex
h_vert = uF;
k_vert = vF-f;

%Equation in roated Axis (x' = u, y' = v)
u = linspace(uF2,uH);
v = (u-h_vert).^2/(4*f)+k_vert;

%Add second leg
[uF1L,vF1L] = rotateToTilted(F(1),F(2),-th);
[uF2L,vF2L] = rotateToTilted(F2(1),F2(2),-th);
[uH1L,vH1L] = rotateToTilted(H2(1),H2(2),-th);
[uH2L,vH2L] = rotateToTilted(H(1),H(2),-th);

h_vert_L = uF2L;
k_vert_L = vF2L-f;

uLeft = linspace(uH1L,uF1L);
vLeft = (uLeft-h_vert_L).^2/(4*f)+k_vert_L;
```

```
%Transorm equation of left leg to right leg coordinate system
[xLeft,yLeft] = rotateToOriginal(uLeft,vLeft,-th);

%Equation of Left leg in same u-v system as right leg, for plotting
[uLeftPlot,vLeftPlot]=rotateToTilted(xLeft,yLeft,th);

%% Input Parameters

numPts = 5; % number of pts where ray hits
panels = 3;
incidence_max = 30; %deg
ribsMin = 5;
ribsMax = 5;

%% Generate equations for CPC panels

intSize = (uH-uF2)/panels;
x_endpoints = zeros(1,panels+1);
y_endpoints = zeros(1,panels+1);
x_endpoints(1) = uF2;
y_endpoints(1) = vF2;
m = zeros(1,panels);
normal_dir = zeros(panels,2); %normal vector to each panel
refl_dir = zeros(panels,2); %direction of reflected ray from a panel
angle_normal = zeros(1,panels); %angle of normal vector for each panel
x_line = zeros(panels,numPts);
y_line = zeros(panels,numPts);


%% Generate Incident Rays

t_par = linspace(-20,20,5); % parametric parameter, incident ray
t_par_refl = linspace(0,20,5);
inc_dir = zeros(1,2); %direction of incident ray

%Vectors [m,n] to store coordinates of rays
%m: incidence angle; n: point of entry
xIncidence = {0,0};
yIncidence = {0,0};
xReflection = {0,0};
yReflection = {0,0};

incidenceAngle = zeros(1,incidence_max+1);

%Points of entry on concentrator aperture
xAperture = linspace(-a+.001,a-.001,numPts);
yAperture(1:length(xAperture)) = L;
[uAperture,vAperture]=rotateToTilted(xAperture,yAperture,th);

%% Ray Tracing Analysis

bad = zeros(incidence_max+1, ribsMax-ribsMin+1);
good = zeros(incidence_max+1, ribsMax-ribsMin+1);
totalGood = zeros(incidence_max+1,ribsMax-ribsMin+1);
```

```
totalBad = zeros(incidence_max+1,ribsMax-ribsMin+1);
totalRays = zeros(incidence_max+1,ribsMax-ribsMin+1);

goodRays = {0,0};
reflections = {0,0};
reflectivity = {0,0};
optEfficiency = zeros(panels,ribsMax-ribsMin+1);

figure()
plot(u,v);
hold on;
plot(uLeftPlot,vLeftPlot)
xlim([-5 12]);
ylim([-3 10]);
% axis equal
title(['Incidence Angle = 30 deg; # of Panels = ',num2str(panels),'; # of
Ribs: ',num2str(ribsMax)],'FontSize',12)
xlabel('U-axis','FontSize',12)
ylabel('V-axis','FontSize',12)



% Efficiency = f(ribs,incidence angle) for N panels
for ribs = ribsMin:ribsMax
    collector_length = b*cos(pi/ribs);
    xCollector = linspace(-collector_length,collector_length);
    yCollector = zeros(size(xCollector));
    [uCollector,vCollector]=rotateToTilted(xCollector,yCollector,th);

    h1 = plot(uCollector,vCollector,'--','LineWidth',2);

    for n = incidence_max:incidence_max
        th_incidence = degtorad(n);
        inc_dir = [sin(th_incidence),cos(th_incidence)];
        incidenceAngle(n+1) = acceptance-n;
        x0 = 0;
        y0 = 0;
        x1 = 0;
        y1 = 0;

        for ray = 1:numPts
            xIncidence{n+1,ray} = uAperture(ray) + t_par*inc_dir(1);
            yIncidence{n+1,ray} = vAperture(ray) + t_par*inc_dir(2);

            h2 = plot(xIncidence{n+1,ray},yIncidence{n+1,ray},'r');


[x0,y0]=intersections(xIncidence{n+1,ray},yIncidence{n+1,ray},uCollector,vCol
lector);
            if ~isempty(x0)
                good(n+1,ribs-ribsMin+1) = good(n+1,ribs-ribsMin+1) + 1;
                goodRays{n+1,ribs-ribsMin+1}(ray) = 1;
                reflections{n+1,ribs-ribsMin+1}(ray) = 0;
            else
                for section = 1:panels %looking at each panel
```

```
                    x_endpoints(section+1) = x_endpoints(section) + intSize;
                    y_endpoints(section+1) = (x_endpoints(section+1)-
h_vert)^2/(4*f)+k_vert;
                    m(section) =
slope(x_endpoints(section)+intSize/2,h_vert,f);
                    x_line(section,:) =
linspace(x_endpoints(section),x_endpoints(section+1),numPts);
                    y_line(section,:) = m(section)*(x_line(section,:)-
x_endpoints(section))+y_endpoints(section);
                    angle_normal(section) = pi/2 - atan(m(section));
                    normal_dir(section,:) = [-
cos(angle_normal(section)),sin(angle_normal(section))];
                    refl_dir(section,:) = -inc_dir +
2*dot(inc_dir,normal_dir(section,:))*normal_dir(section,:);

                    h3 =
plot(x_line(section,:),y_line(section,:),'LineWidth',3);


[x0,y0]=intersections(xIncidence{n+1,ray},yIncidence{n+1,ray},x_line(section,
:),y_line(section,:));
                    if ~isempty(x0)
                        reflections{n+1,ribs-ribsMin+1}(ray) = 1;
                        xReflection{n+1,ray} = x0(1) +
t_par_refl*refl_dir(section,1);
                        yReflection{n+1,ray} = y0(1) +
t_par_refl*refl_dir(section,2);

                        h4 =
plot(xReflection{n+1,ray},yReflection{n+1,ray},'g','LineWidth',2);


[x1,y1]=intersections(xReflection{n+1,ray},yReflection{n+1,ray},uCollector,vC
ollector);
                        if ~isempty(x1)
                            good(n+1,ribs-ribsMin+1) = good(n+1,ribs-
ribsMin+1) + 1;
                            goodRays{n+1,ribs-ribsMin+1}(ray) = 1;
                        else
                            bad(n+1,ribs-ribsMin+1) = bad(n+1,ribs-ribsMin+1)
+ 1;
                            goodRays{n+1,ribs-ribsMin+1}(ray) = 0;
                        end
                    end
                end
            end
        end
        reflectivity{n+1,ribs-ribsMin+1} = goodRays{n+1,ribs-
ribsMin+1}.*(0.93.^reflections{n+1,ribs-ribsMin+1});
        optEfficiency(n+1,ribs-ribsMin+1) = sum(reflectivity{n+1,ribs-
ribsMin+1}*1/numPts);
    end
end
legend([h1 h2 h3 h4 ],{'Collector','Incident Rays','Panels','Reflected
Rays'},'Location','Southeast')
```

```
% optEfficiency
% figure()
% surf(ribsMin:1:ribsMax,incidenceAngle,optEfficiency)
% title(['Number of Panels: ',num2str(panels)]);
% xlabel('Number of ribs');
% ylabel('Incidence Angle');
% zlabel('Optical Efficiency');
```

3. Ray tracing analysis considering both sides of concentrator and multiple reflections:

```
%% CPC Parameters

clc
clear all
close all

% a = 16.56; % aperture radius, in.
% acceptance = 25; %deg
a = 4;
acceptance = 40;
th = degtorad(acceptance);
b = a*sin(th); % collector radius, in.

% Concentrator Height
L = (a+b)*cot(th); %in.
% Focus of parabola (curve for each leg)
f = L*sin(th)^2/cos(th);

% Points in parabola, x-y plane
F = [-b,0]; %focus
F2 = [b,0];
H = [a,L]; %end of parabola
H2 = [-a,L];

% Points of parabola in u-v plane (rotated by th)
[uF,vF] = rotateToTilted(F(1),F(2),th);
[uF2,vF2] = rotateToTilted(F2(1),F2(2),th);
[uH,vH] = rotateToTilted(H(1),H(2),th);
[uH2,vH2] = rotateToTilted(H2(1),H2(2),th);

%Vertex
h_vert = uF;
k_vert = vF-f;

%Equation in roated Axis (x' = u, y' = v)
u = linspace(uF2,uH);
v = (u-h_vert).^2/(4*f)+k_vert;

%Add second leg
[uF1L,vF1L] = rotateToTilted(F(1),F(2),-th);
[uF2L,vF2L] = rotateToTilted(F2(1),F2(2),-th);
[uH1L,vH1L] = rotateToTilted(H2(1),H2(2),-th);
[uH2L,vH2L] = rotateToTilted(H(1),H(2),-th);

h_vert_L = uF2L;
k_vert_L = vF2L-f;

uLeft = linspace(uH1L,uF1L);
vLeft = (uLeft-h_vert_L).^2/(4*f)+k_vert_L;

%Transorm equation of left leg to right leg coordinate system
[xLeft,yLeft] = rotateToOriginal(uLeft,vLeft,-th);
```

```
%Equation of Left leg in same u-v system as right leg, for plotting
[uLeftPlot,vLeftPlot]=rotateToTilted(xLeft,yLeft,th);

%% Define collector, or concentrator exit

xCollector = linspace(-b,b);
yCollector(1:length(xCollector)) = 0;
% yCollector(1:length(xCollector)) = -0.8; %gap between exit and solar cell
% yCollector(1:length(xCollector)) = -3.625; %gap between exit and solar
cell, full-scale inflatable and solar panel w/ mask

% Using solar cell for full-scale testing
% solarCellLength = 4.492; %in
% xCollector = linspace(-solarCellLength/2,solarCellLength/2);% %center
position
% % xCollector =
linspace(solarCellLength/2+0.5,solarCellLength/2+0.5+solarCellLength); %side
% yCollector(1:length(xCollector)) = -3.625;


[uCollector,vCollector]=rotateToTilted(xCollector,yCollector,th);

%% Input Parameters

numPts = 500; % number of pts where ray hits
panels = 6;
incidence_max = 34; %deg

%% Generate equations for CPC panels

%Initialize values
x_line = {0,0};
y_line = {0,0};
x_endpoints = zeros(panels,panels+1);
y_endpoints = zeros(panels,panels+1);
x_endpoints(:,1) = uF2;
y_endpoints(:,1) = vF2;
m = zeros(panels,panels);
normal_dir = {0,0}; %normal vector to each panel
refl_dir = {0,0}; %direction of reflected ray from a panel
angle_normal = zeros(panels,panels); %angle of normal vector for each panel

%Right side
for n = 1:panels
    intSizePanels = (uH-uF2)/n;
    for section = 1:n % look at each panel independently
       x_endpoints(n,section+1) = x_endpoints(n,section) + intSizePanels;
       y_endpoints(n,section+1) = (x_endpoints(n,section+1)-
h_vert)^2/(4*f)+k_vert;
       m(n,section) = slope(x_endpoints(n,section)+intSizePanels/2,h_vert,f);
       x_line{n,section} =
linspace(x_endpoints(n,section),x_endpoints(n,section+1),numPts);
       y_line{n,section} = m(n,section)*(x_line{n,section}-
x_endpoints(n,section))+y_endpoints(n,section);
```

```
        angle_normal(n,section) = pi/2 - atan(m(n,section));
        normal_dir{n,section} = [-
cos(angle_normal(n,section)),sin(angle_normal(n,section))];
    end
end

%Left side
x_endpointsLeft = -x_endpoints;
y_endpointsLeft = y_endpoints;
[x_endPtLeft,y_endPtLeft] =
rotateToTilted(x_endpointsLeft,y_endpointsLeft,2*th);
mLeft = zeros(panels,panels);
x_lineL = {0,0};
y_lineL = {0,0};
angle_normal = zeros(panels,panels);
normal_dirL = {0,0};

for n = 1:panels
    for section = 1:n
        m(n,section+n) = (y_endPtLeft(n,section+1)-
y_endPtLeft(n,section))/(x_endPtLeft(n,section+1)-x_endPtLeft(n,section));
%         x_lineL{n,section} =
linspace(x_endPtLeft(n,section),x_endPtLeft(n,section+1),numPts);
%         y_lineL{n,section} = mLeft(n,section)*(x_lineL{n,section}-
x_endPtLeft(n,section))+y_endPtLeft(n,section);
        x_line{n,section+n} =
linspace(x_endPtLeft(n,section),x_endPtLeft(n,section+1),numPts);
        y_line{n,section+n} = m(n,section+n)*(x_line{n,section+n}-
x_endPtLeft(n,section))+y_endPtLeft(n,section);
        angle_normal(n,section+n) = pi/2 - atan(m(n,section+n));
        normal_dir{n,section+n} = [-
cos(angle_normal(n,section+n)),sin(angle_normal(n,section+n))];

%
plot(x_line{n,section+panels},y_line{n,section+panels},'LineWidth',3)
%         hold on
    end
end


% Combine all equations of lines in one matrix, sec 1: lower left, sec n:
% upper right

%% Generate Incident Rays

inc_dir = zeros(1,2); %direction of incident ray
t_par = linspace(-60,20,5); % parametric parameter, incident ray
t_par_refl = linspace(0,60,5);

%Vectors [m,n]to store coordinates of rays
%m: incidence angle; n: point of entry
xIncidence = {0,0};
yIncidence = {0,0};
xReflection = {0,0};
yReflection = {0,0};
```

```
reflections = {0,0};

incidenceAngle = zeros(1,incidence_max+1);

%Points of entry on concentrator aperture
xAperture = linspace(-a+.001,a-.001,numPts);
yAperture(1:length(xAperture)) = L;
[uAperture,vAperture]=rotateToTilted(xAperture,yAperture,th);


%% Ray Tracing Analysis

totalGood = zeros(panels,incidence_max+1);
totalBad = zeros(panels,incidence_max+1);
totalRays = zeros(panels,incidence_max+1);

bad = zeros(panels,incidence_max+1);
good = zeros(panels,incidence_max+1);
goodRays = {0,0};

reflectivity = {0,0};
optEfficiency = zeros(panels,incidence_max+1);


% plot(u,v);
% hold on;
% plot(uLeftPlot,vLeftPlot)
% h1 = plot(uCollector,vCollector,'--');

for n = panels:panels
    intSizePanels = (uH-uF2)/n;
    x0 = 0;
    y0 = 0;
    x1 = 0;
    y1 = 0;
    otherPanel = 0;

    for i = incidence_max:incidence_max
        incidenceAngle(i+1) = acceptance-i;
        th_incidence = degtorad(i);
        inc_dir = [sin(th_incidence),cos(th_incidence)];
        for ray = 1:numPts
%           ray
            xIncidence{i+1,ray} = uAperture(ray) + t_par*inc_dir(1);
            yIncidence{i+1,ray} = vAperture(ray) + t_par*inc_dir(2);

%             h2 = plot(xIncidence{i+1,ray},yIncidence{i+1,ray},'r');

            for section = 1:2*n
%                 section
%                 h3 =
plot(x_line{n,section},y_line{n,section},'LineWidth',3);

                xRay = xIncidence{i+1,ray};
```

```
                yRay = yIncidence{i+1,ray};

[x0,y0]=intersections(xRay,yRay,x_line{n,section},y_line{n,section});
%                 x0
                if ~isempty(x0)
                    otherPanel = 2*n;
                    reflections{n,i+1}(ray) = 1;
                    refl_dir{n,section} = -inc_dir +
2*(dot(inc_dir,normal_dir{n,section}))*normal_dir{n,section};
                    xReflection{i+1,ray} = x0(1) +
t_par_refl*refl_dir{n,section}(1);
                    yReflection{i+1,ray} = y0(1) +
t_par_refl*refl_dir{n,section}(2);
                    xRay = xReflection{i+1,ray};
                    yRay = yReflection{i+1,ray};

%                     h4 = plot(xRay,yRay,'g','LineWidth',2);

                    while otherPanel > 0

[x1,y1]=intersections(xRay,yRay,x_line{n,otherPanel},y_line{n,otherPanel});
                        if (~isempty(x1) && abs(x1-x0) > 0.0001)
                            reflections{n,i+1}(ray) = reflections{n,i+1}(ray)
+ 1;
                            angle_normal2 = angle_normal(n,otherPanel);
                            normal_dir2 = normal_dir{n,otherPanel};
                            inc_dir2 = refl_dir{n,section};
                            refl_dir2 = inc_dir2 -
2*dot(inc_dir2,normal_dir2)*normal_dir2;
                            xRay = x1 + t_par_refl*refl_dir2(1);
                            yRay = y1 + t_par_refl*refl_dir2(2);

%                             plot(xRay,yRay,'g','LineWidth',2);

                        end
                        otherPanel = otherPanel - 1;
                    end
                    [x2,y2]=intersections(xRay,yRay,uCollector,vCollector);
%                   x2
                    if ~isempty(x2)
                        good(n,i+1) = good(n,i+1) + 1;
                        goodRays{n,i+1}(ray) = 1;
%                         'good'
                        break
                    else
                        bad(n,i+1) = bad(n,i+1) + 1;
                        goodRays{n,i+1}(ray) = 0;
%                         'bad'
%                         x2
                        reflections{n,i+1}(ray) = 0;
                        break
                    end
                elseif (isempty(x0) && section == 2*n)
                    [x3,y3]=intersections(xRay,yRay,uCollector,vCollector);
                    if ~isempty(x3)
                        good(n,i+1) = good(n,i+1) + 1;
```

```
                        goodRays{n,i+1}(ray) = 1;
%                         'good'
                    else
                        bad(n,i+1) = bad(n,i+1) + 1;
                        goodRays{n,i+1}(ray) = 0;
%                         'bad'
                        reflections{n,i+1}(ray) = 0;
%                         x3
                    end
                end
            end
        end
        reflectivity{n,i+1} = goodRays{n,i+1}.*(0.93.^reflections{n,i+1});
        optEfficiency(n,i+1) = sum(reflectivity{n,i+1}*1/numPts);
    end
end

%
% figure()
% surf(incidenceAngle,1:panels,optEfficiency)
% xlabel('Incidence angle (deg)')
% ylabel('# of panels')
% zlabel('Efficiency')
```